Magnetic resonance imaging of theranostic drug carriers - from relaxation studies to image contrast assessment

mgr inż. Natalia Łopuszyńska

Supervisors:

dr hab. Władysław Węglarz, Institute of Nuclear Physics PAS

Prof. dr hab. Piotr Warszyński, Institute of Catalysis and Surface Chemistry PAS

A thesis submitted in fulfilment
of the requirements for the degree of

Doctor of Philosophy

in the
Henryk Niewodniczański Institute of Nuclear Physics
Polish Academy of Sciences

Kraków, 2021

Acknowledgements

First and foremost, I would like to thank Dr. Władysław Węglarz and Prof. Piotr Warszyński, without whose supervision this thesis would not exist. I would like to express my sincerest gratitude for the opportunity to work in many exciting interdisciplinary projects as a PhD student at The Henryk Niewodniczanski Institute of Nuclear Physics Polish Academy of Sciences.

I would also like to extend my appreciation to Dr. Krzysztof Szepanowicz and Marta Szczęch for the synthesis of the majority of the materials that have been investigated in this thesis, to Dr. Alexey Maximenko, for including me in his research project, numerous discussions, and for help with interpretation of the results, and to Dr. Krzysztof Jasiński for invaluable help with experiments and technical difficulties. Many thanks to all colleagues from the Department of Magnetic Resonance Imaging for their support and creation of a friendly atmosphere throughout my studies.

Last but not least I would like to thank my best friend and partner Alexandre for being my greatest support and inspiration.

The doctoral dissertation was prepared during
Cross-institutional PhD Studies
under the framework of the project nr POWR.03.02.00-00-I013/16,
“Interdisciplinarity for Innovative Medicine”; InterDokMed,
implemented as part of the Operational Program Knowledge, Education and Development for 2014-2020, co-financed by the European Social Fund

Table of Contents

List of figures

List of tables

Chapter 1

Introduction

Cancer is a leading cause of death worldwide, accounting for nearly 10 million deaths in 2020. The most common cases of cancer in 2020 were: breast, lung, colon and rectum, prostate, skin, and stomach, while lung, colon and rectum, liver, stomach, and breast are the most common causes of cancer death. Moreover, as reported by WHO, in high-income countries the group of the lung, bronchus, and trachea cancers is in the first four top causes of overall deaths in 2020, followed by colon and rectum cancers as the 7th [1]. Despite dynamic development in the fields of cancer diagnosis and therapy, there are still significant challenges to overcome. Currently available anticancer treatment options, including radiotherapy, chemotherapy, and surgery, are invasive, painful, and sometimes imprecise, and therefore ineffective. As a result, significant acute and chronic adverse effects negatively impacting the patient's overall outcome are observed, especially in the case of chemotherapy and radiotherapy which target non-specifically fast-dividing cells whether they are cancerous or not [2]. The development of effective drug therapy based on targeted platforms that can distinguish between cancer and healthy cells, and deliver a therapeutic dose to cancer cells is a major goal of drug discovery [3].

To enable effective action, therapeutic agents have to be delivered to their specific destinations, which are usually the cytoplasm or nucleus of cancer cells. However, as many chemotherapeutics suffer from low aqueous solubility and poor pharmacokinetics, their therapeutic effect is limited and the therapeutic doses are in general high. Moreover, due to the small size and molecular weight of particles, the clearance of these agents from the circulation is very rapid, resulting in a short half-life that limits clinical use [3]. The integration of nanotechnology and drug design can address those problems by offering nanosystems with high surface-to-volume ratios and with unique physiochemical properties. Specifically, the use of nanocarriers for drug delivery offers the following advantages; it prevents the drug from rapid degradation, resulting in an increased half-life of the drug in the systemic circulation; appropriate design of nanocarrier improves the solubility and stability of anticancer drugs; it advances drug distribution and

targeting of the cancer sites, ensures a sustained release of the drug; and it can reduce drug resistance by the delivery of multiple therapeutic agents [2]. In general, the delivery of anticancer drugs in nanoparticle systems to tumor sites can be accomplished by either passive or active targeting. In active targeting, the NPs are conjugated with a ligand moiety, such as peptides, aptamers, antibodies, and small molecules that can be selectively recognized by specific receptors, whereas passive targeting is based on the enhanced permeation and retention effect. In addition, the enhancement of NPs accumulation in the desired location can be achieved by the use of external forces. For example, it is possible to direct nanocarriers containing magnetic NPs with the magnetic field.

Moreover, nanotechnology offers the opportunity to combine chemotherapeutics with biomedical imaging agents and other treatment modalities to overcome the challenges of cancer diagnosis and therapy. The combination of diagnosis and therapy in a single nanocarrier is referred to as theranostics. Such an approach presents synergistic advantages in comparison to separately conducted imaging and treatment procedures [4]. In particular, the use of well-designed theranostic agents allows the simultaneous delivery of therapeutic and imaging agents in a single dose, with the potential to overcome the undesirable differences in biodistribution and selectivity, that occur when using the standard two-step procedure. The main expected effect of the use of theranostics is to enable the imaging and monitoring of diseased tissue anatomy, as well as studying the kinetics of drug delivery and its efficacy, with the long-term hope of achieving treatment dose adjustments with much greater control and precision. The most commonly used imaging modalities for nanoparticle tracking in vivo, as well as for structural, functional, and molecular imaging of the tumor region, include fluorescence imaging, positron emission tomography (PET), magnetic resonance imaging (MRI), and computed tomography (CT), which are characterized by different sensitivity, resolution, and penetration depths [5]. In the case of MRI, the observation of NCs distribution is accomplished by the attachment of contrast agents that either modify the relaxation rates of the surrounding (positive or negative contrast agents) or can be directly detected (hot-spot agents). The most extensively studied therapeutic applications combined with MRI diagnosis include chemotherapy, gene therapy, thermal therapy (magnetic hyperthermia, photothermal therapy, and ultrasound and radiofrequency-induced thermal therapy),

reactive oxygen species based cancer therapy (photodynamic therapy, sonodynamic therapy, and ferroptosis), and combination therapies, mostly combining thermal therapy with chemo or radiotherapy.

The aim of the thesis was to evaluate the theranostic potential of various nanocarriers in terms of their contrasting efficiency for magnetic resonance imaging. Regarding the similarity of the composition and the application of nanocarriers, two main groups of investigated formulations can be distinguished, namely polyelectrolyte nanocapsules with multilayer shells for anticancer (paclitaxel, or 5-FU) drug delivery, and core-shell nanoparticles for photothermal therapy. In the group of polyelectrolyte nanocapsules following nanosystem with contrast agents of standard, relaxation type (positive and negative), as well as direct detection agents based on ^{19}F compounds were investigated, specifically:

- Gadolinium-labelled polyelectrolyte nanocarriers with encapsulated Paclitaxel, where formulations with nanoemulsion and polymeric cores were compared;
- Magnetically responsive polycaprolactone nanocarriers with Fe_3O_4 nanoparticles as MRI contrast agents with encapsulated Paclitaxel, where two types of multilayer shell were investigated;
- Nafion™-Based Theranostic Nanocapsules with Paclitaxel for x-nuclei MRI detection;
- and polyelectrolyte nanocapsules with 5-fluorouracil, where 5-FU is used as both therapeutic and imaging agent for ^{19}F MRI.

In the case of core-shell nanoparticles, different variations of core shape and shell thickness were tested, namely:

- NPs with a spherical-shaped Fe_3O_4 core, coated by a 10 nm thick SiO_2 shell;
- NPs with a cubic-shaped Fe_3O_4 core, coated by a 10 nm thick SiO_2 shell;
- and NPs with a cubic-shaped Fe_3O_4 core, coated by a 2 nm thick SiO_2 shell.

The synthesis of nanocarriers for MR investigations as well as their physicochemical characterization and therapeutic efficiency tests were performed in cooperation with two groups, one from the Institute of Nuclear Physics PAS and one from the Jerzy Haber Institute of Catalysis and Surface Chemistry PAS.

The main hypothesis is that it is possible to use MR imaging to detect theranostic nanocarriers at a therapeutic dose. To test that, the contrasting efficiency of synthesized nanocarriers was investigated in order to find the most optimal composition of each NP type. For nanoparticles with relaxation contrast agents based on Gadolinium and F_3O_4 particles, the contrasting properties were evaluated by means of MR relaxometry, specifically relaxivity measurements. Following that, an imaging study of gel- or water-based phantoms with nanoparticles was conducted with the goal of visualizing their MRI contrasting properties and establishing optimal sequence parameters. The Mössbauer spectroscopy and SQUID magnetometry data were taken into account to better understand and explain the obtained results. In the case of nanocapsules based on direct-detection agents, a contrasting effect was achieved by imaging on ^{19}F nuclei and imposing the MR image of their spatial distribution over the standard anatomical image on protons. For that reason, the contrasting efficiency of those so-called hot-spot agents was evaluated based on values of the signal-to-noise ratio in ^{19}F MR images. Therefore, the main objective in ^{19}F imaging experiments was to optimize the imaging conditions in order to reliably determine the location of ^{19}F-containing agents.

The thesis consists of 6 chapters. In the first introductory chapter, the research problem is outlined. Chapter two, fundamentals and state of the art, presents the theoretical background of conducted experiments. It starts with a description of the current knowledge about the studied matter, providing a comprehensive overview of what has been done in the field. Next, the physical principles of magnetic resonance imaging are described, followed by an overview of available contrast agents classified by the mechanism of their action. In the third chapter, materials, and methods, the description of the investigated theranostic nanosystem is provided, including a short description of the chemical composition and the synthesis process. Subsequently, the experimental equipment and applied measurement and analysis methods are described. Chapter four shows the experimental results obtained for all the investigated materials. This chapter is divided into three parts. The first section is devoted to the nanosystem containing relaxation contrast agents of the superparamagnetic (negative) type. The second part displays results obtained for nanocapsules containing gadolinium ions, which are positive relaxation contrast agents. Finally, in the third part, results of imaging of nanocarriers containing direct detection contrast agents based on ^{19}F atoms are

presented. Chapter six, discussion, provides the interpretation of the obtained experimental results. It consists of two subsections, one concerning nanocarriers based on relaxation contrast agents, and the other about ^{19}F MR imaging of direct detection contrast agents. Considerations are supplemented with results of Mössbauer spectroscopy and SQUID magnetometry, as well as information on the therapeutic potential of investigated materials based on cell viability tests. The last chapter, conclusions, points out the most important outcomes of the thesis and is followed by a list of relevant references.

Chapter 2

Fundamentals and state of the art

2.1. Theranostics for MR-guided therapy

The 'theranostics' is a relatively new term, that was originally introduced by Funkhouser in 2002 [6]. It's a concept of combining two modalities, therapy, and diagnostic imaging. Initially, the term was closely related to personalized medicine, a strategy of closely linking disease diagnosis with the application of appropriate therapy. Later, 'theranostic' gained a new meaning and nowadays is used to describe a single agent in which the diagnostic and therapeutic properties are combined. Theranostics aims to offer a more patient-specific approach, through the adjustment of the therapeutic dose individually for each patient, based on the observation of the distribution of contrast agents that are linked to therapeutics. By combining both the diagnostic and therapeutic aspects, it is possible to reduce the number of agents administered to patients, their dose, and the number of invasive treatments they must undergo [7]. For theranostic purposes, the most commonly used imaging modalities are positron emission tomography (PET), single-photon emission computed tomography (SPECT), ultrasound imaging, magnetic resonance imaging (MRI), and computed tomography (CT). For each of those methods, different imaging agents that can be incorporated into the theranostic device are available. Moreover, each of these modalities has some unique advantages and limitations that have to be taken into account when selecting appropriate imaging techniques for desired information.

For PET imaging, probes based on ^{18}F, ^{64}Cu, ^{11}C, and ^{15}O-labelled compounds are used, while SPECT utilizes ^{99m}Tc, and ^{111}In chelates [8]. Both methods are based on the detection of γ radiation emitted by the radionuclide administered in the form of a radiopharmaceutical and are referred to as nuclear imaging modalities. Nuclear imaging is characterized by very high sensitivity and provides quantitative results. However, those methods are associated with risks related to high radiation doses, and they suffer from low spatial resolution [9]. Also, they don't provide anatomical information therefore,

additional imaging modalities are required to localize the radiotracer in the anatomical context. In the standard approach, SPECT or PET imaging is combined with CT (Computed Tomography), or less frequently, with MRI. The CT scan is based on the measurement of the ionizing radiation (x-ray) attenuations in body tissues. To increase the contrast between tissues, CT uses mainly probes that are based on iodine. However, lanthanide–chelate contrast agents that were initially developed for MRI, gold nanoparticles, and other metallic contrast agents, including Bi-based probes and Fe/Pt alloys, are also used [10] [11]. CT provides tomographic imaging, but again, its main disadvantage is the use of ionizing radiation. Ultrasound imaging is one of the most commonly used diagnostic techniques in the clinic because of its ease of operation and real-time results. It offers high resolution and relatively low costs. However, the depth of imaging is limited. Microbubbles and nanobubbles are contrast agents available in ultrasound imaging for theranostic purposes [12] [13]. Finally, MRI is a technique that, similarly to CT, has tomographic capabilities, but does not utilize ionizing radiation to create the image. It allows for imaging at any depth within the object and has submillimetre resolution in-vivo. Its main disadvantage is low sensitivity, which can be solved by the use of contrast agents. There is a very wide range of contrast agents used in MR imaging, which are usually based on gadolinium, iron oxide, manganese oxide, or ^{19}F-labelled compounds [14] [4]. A more detailed description of the types and mechanisms of action of contrast agents for MR imaging is provided in chapter 2.3.

For theranostic purposes, MRI contrast agents are combined with therapeutic components for the implementation of targeted anti-cancer therapy such as MR-guided drug delivery, thermal therapies including photothermal therapy, magnetic hyperthermia treatment, ultrasound, and radiofrequency-induced thermal therapy, reactive oxygen species–based therapy, gene therapy, and combination therapies. Targeting of nanoparticles to tumor sites can be achieved either passively, actively, or through externally applied forces. Passive targeting is accomplished by enhanced permeability and retention (EPR) effect where nanoparticles accumulation is increased due to leaky vasculature with pores of 100 nm to 2 μm in diameter and impaired lymphatic drainage in the tumor. In active targeting, specific interactions between a ligand attached to the theranostic nanoparticle surface and a receptor on the target cells are used. Those ligands include peptides, aptamers, antibodies, and small molecules. The targeting based on

external forces is accomplished by the use of magnetically-responsive carriers and an external magnetic field. Moreover, those approaches are often applied simultaneously in one theranostic nanodevice that allows for more efficient drug delivery to the tumor site. In this thesis, nanocarriers for drug delivery and thermal therapy were investigated. Therefore, a short overview of similar nanocarriers is provided.

Regarding drug delivery, the application of nanocarriers provides prolonged circulation time of drugs, improves their efficacy, overcomes complex delivery barriers, and reduces side effects compared to free drug formulations. For instance, in [15], Ganipineni et al. reported the application of paclitaxel (PTX) and superparamagnetic iron oxide (SPIO)-loaded PEGylated PLGA-based nanoparticles to treat glioblastoma via magnetic targeting. Based on MRI images, the blood-brain barrier at the glioblastoma site was seen to be disrupted, and PLGA nanoparticles could be accumulated in the mouse brain via magnetic treatment. NPs did not induce any systemic toxicity compared with free PTX, while the treatment significantly prolonged the median survival time compared with the passive targeting and control treatments. In [16] a complex of SPIO-Doxorubicin-conjugated microbubbles for drug delivery to the brain was developed by Fan et al. Magnetic labelling enabled visualization via MRI and magnetic targeting for enhanced deposition of the drug in the tumor. It was shown, that focused ultrasound sonication can be used with synthesized NCs to enable blood-brain barrier opening, and allowed dual ultrasound/magnetic targeting of Doxorubicin (DOX) delivery in a rat glioma model. The accumulation of the complex within brain tumors was evaluated by the change in relaxation rate R_2 which was confirmed also by liquid chromatography and inductively coupled plasma-atomic emission spectroscopy. Shakeri-Zadeh et al. [17] synthesized 5-FU/magnetite/PLGA nanocapsules for the targeted delivery of 5-fluorouracil to colorectal cancer. Magnetic drug targeting was used to selectively focus chemotherapeutics in tumor tissue. In vivo release investigations showed that fabricated nanocapsules have a prolonged lifetime in the rabbit plasma compared with free 5-FU. Magnetic resonance imaging confirmed that the magnetic nanocapsules were successfully targeted to the tumor. Additionally, the magnetic nanocapsules demonstrated excellent anti-tumor activity against colon cancer (CT26 cells allograft model). In [18], Feng et al. encapsulated PTX and hydrophilic SPIONs inside the core of the copolymer (PEG-P(Asp-DIP)-P(Lys-Ca)) micelles to be used for potential cancer therapy. It was demonstrated that PTX

release from micelles can be controlled by pH change and that as-prepared NCs were effectively internalized by human colon carcinoma cells (LoVo cells). The NCs delivery effect was also positively verified in vivo in a model of colorectal carcinoma xenografts by MRI and histology analysis.

All nanocarriers mentioned so far utilize T2-contrast MRI based on SPIONs. However, in some situations, darkening in NCs accumulation sites can be difficult to distinguish from artifacts induced by various pathological conditions or air cavities. Therefore, theranostic nanocarriers are also designed as positive MRI CAs. For example, in [19], pH-responsive Gd-based nanoparticle–organic frameworks loaded with chemotherapeutic agents DOX and 5-fluorouracil (5-FU) were designed by Ling et al. The proposed nanosystem showed effective dual-drug release by the cleavage of chemical bonds and the disruption of the framework structure induced by acidic pH. Moreover, much higher cytotoxicity was observed for dual-drug NCs in comparison to frameworks loaded with only a single drug (DOX or 5-FU), indicating the synergic effect of Dox and 5-FU released from the NCs. Liu et al. [20] fabricated polymeric, pH-sensitive nanocarriers by the self-assembly of the multi-block polymer (PLA-PEG-PLL-DTPA) and the pH-sensitive material (PLH-PEG-biotin). The anti-hepatocellular carcinoma (HCC) drug sorafenib was encapsulated inside the nanoparticles and Gd ions were attached to the surface of the nanoparticle. In cell cytotoxicity studies, NCs showed a similar antitumor effect against HepG2 cells compared to free drug solution, while in in-vivo anti-tumor studies, a significantly higher antitumor effect in H22 tumor-bearing mice was observed. Regarding MRI tests, the T_1 relaxivity value was 17.3 mM^{-1} s^{-1}, which was much higher than clinically approved Magnevist® (r_1 = 4.8 mM^{-1} s^{-1}).

MRI-detectable theranostic nanocarriers have also been designed to include ^{19}F atoms, which provides the hot-spot contrast that is preferred for quantitative studies. For instance, in [21], Boissenot et al. presented optimization of the encapsulation of paclitaxel (PTX) into core-shell nanocapsules made of a PLGA-PEG shell and PFOB (perfluorooctyl bromide) core to serve as theranostic agents. In in-vitro tests, fabricated nanocapsules induced similar mortality of CT-26 colon cancer cells as free PTX. Additionally, in-vivo ^{19}F-MRI showed that the encapsulation of PTX does not limit its ability to accumulate passively in CT-26 tumors in mice by the EPR effect. Moreover, a twofold reduction in tumor growth as compared with the negative control and with the free PTX group was

observed. Shaowei et al. [22] proposed a fluorinated amphiphile-based ^{19}F MRI-traceable liposomal drug delivery system for in vivo tracking of DOX at therapeutic dose. The fluorinated amphiphile was designed as a dendrimer with highly fluorinated moieties that served as hydrophobic tails and as a ^{19}F MRI detectable agent, and monodisperse PEG as hydrophilic heads that enhance solubility, biocompatibility, and stability. Subsequently, this amphiphile was used for the formulation of ^{19}F MRI traceable liposomes with encapsulated DOX. In the in-vivo ^{19}F MRI-monitored DOX delivery studies on tumor-carrying nude mice, the distribution of the synthesized liposomes in the tumor was observed. Moreover, the amounts of DOX and amphiphile in tumors and kidneys were quantitatively measured. The co-localization of DOX and amphiphile in vivo was observed, proving the efficiency of liposomes to monitor DOX in vivo at the therapeutic dose level. Another formulation for ^{19}F traceable nanocarriers was proposed in [23], where peptidic monodisperse-PEG was modified with fluorinated L-lysine side chains and a fluorescent N-terminal for a ^{19}F MRI and fluorescence dual-imaging traceable and thermo-responsive DOX-loaded liposome fabrication. The efficiency of NCs was investigated in a rodent xenograft model of human liver cancer HepG2 cells. Mice injected with theranostics had higher plasma DOX concentrations than mice injected with free DOX. Additionally, the half-life time of DOX and theranostics in plasma were < 5 and around 15 min, respectively. The therapeutic efficacy in-vivo test showed considerable tumor growth inhibition in the groups treated with free DOX and theranostics. Moreover, tumors sizes in the theranostics treated group were much smaller than that of the free DOX treated group, which showed the improved therapeutic efficacy of theranostics.

MR-guided thermal therapy can be carried out with the use of several different heating sources/mechanisms. These include photothermal therapy (PTT), magnetic hyperthermia treatment (MHT), and ultrasound (US) and radiofrequency (RF)-induced thermal therapy. In this thesis nanoparticles for PTT and MHT were investigated, the overview focuses on those mechanisms. In magnetic hyperthermia treatment, magnetic nanoparticles (MNPs) are subjected to an alternating magnetic field, which results in heat generation and selective tumor cells death. With large, multidomain MNPs, heat is generated via hysteresis losses, while for smaller, single domain NPs, Neel and Brownian relaxation are involved. As a result, the temperature is raised locally in the tumor within the range of 43 - 46 °C, leading to physiological changes in the cancer cells followed by

their apoptosis or necrosis [24]. Theranostics is accomplished mainly by the use of SPIONs like Fe_3O_4 or Fe_2O_3, as they demonstrate preferable magnetic properties for magnetic heating, low toxicity, magnetic targeting, and MRI contrasting. To further enhance this potential, SPIONs are conjugated with different compounds to form efficient nanodevices for MHT. For instance, Hayashi [25] prepared clustered SPIONs for the effective enhancement of MRI contrast in tumors and inhibition of tumor growth by magnetic hyperthermia (MHT). Obtained clusters were modified with folic acid and PEG to promote their accumulation and prolong the retention in tumors. After 24 hours post i.v. injection of FA-PEG-SPION nanoclusters, their local accumulation in cancer tissues within the tumor, and enhanced MRI contrast were observed. Subsequently, mice were placed in an AC magnetic field with H = 8 kA/m and f = 230 kHz for 20 min. Due to the accumulation of nanoclusters, tumors underwent local heating, with the temperature raise higher than the surrounding tissues by ≈6°C, 20 min after treatment (the average SAR was 104 $W/g_{Fe)}$. The tumor volume of treated mice was one-tenth that of the control group 35 days after treatment. Furthermore, mice treated with MHT were alive after 12 weeks, while the control group died up to 8 weeks post-treatment. Similar folic acid-modified nanoparticles were proposed by Soleymani et al. [26], where dextran-coated biocompatible magnetite nanoparticles with high heating efficacy were synthesized. The folic acid was conjugated to the surface of the prepared nanoparticles to enhance their accumulation in tumors with overly expressed folate receptors, such as breast, colon, lung, and brain tumors. The heat generation efficiency of the synthesized nanoparticles was evaluated by SAR value measurement that was 37.6 and 52.3 $W\,g^{-1}$ (for the magnetic field of H = 12.5 or 15.0 mT and f = 150 kHz). The NPs were relatively nontoxic even at high concentrations of up to 1000 $\mu g\,mL^{-1}$ in vitro, and 100 $mg\,kg^{-1}$ in vivo. In-vivo MRI experiments proved enhanced accumulation and retention of the FA@Fe_3O_4 NPs within the tumor tissue. Moreover, hyperthermia treatment performed on an animal model of breast tumor showed a significant difference in tumor growth between the treated mice in the MHT with NPs group and the untreated mice in the control group.

Magnetic hyperthermia can also be utilized to improve drug delivery efficiency in difficult environments by offering controlled on-demand drug release in the desired location. In [27], the effect of MHT in combination with local chemotherapy to inhibit patient-derived colorectal cancer stem cells (qCR-CSCs) was investigated by Fernandes et

al. Iron oxide nanocubes were coated with a thermoresponsive polymer (TR-Cubes) and loaded with DOXO (TR-DOXO) as a chemotherapeutic agent that was released from the polymer only at a temperature above 44 °C. In cell viability tests, qCR-CSCs exposed to TR-nanocubes and treated with MHT struggled to survive the heat damage and exhibited delayed restart division of dormant cells. However, the complete stop of the colony formation was achieved only after incubation with TR-DOXO NPs and MHT treatment. The in vivo study confirmed this synergic effect of MHT and heat-induced drug release. Only the group of animals that received the CR-CSCs pre-treated with TR-DOXONPs and MHT did not form the tumour, even after several months. A similar approach was employed by Hayashi et al. [28], where magnetic field responsive NPs were created by combining the DOX and clustered Fe_3O_4 NPs within a polymer (carboxylic polypyrrole) with a glass-transition temperature (T_g) of 44 °C. To improve the NP retention in the tumour, NPs were modified with PEG and folic acid. During exposure to the alternating current magnetic field, the NPs core consisting of the Fe_3O_4 cluster produces heat, leading to the softening of the polymer phase and, as a result, the release of DOX. The combination of MHT and chemotherapy using the Fe_3O_4/DOX/PPy-PEG-FA NPs destroyed cancer cells in the entire tumor and achieved a complete cure in one treatment. Furthermore, Fe_3O_4/DOX/PPy-PEG-FA NPs exhibited no significant toxicity, demonstrating that the combination of MHT and chemotherapy could destroy the tumor without damaging normal tissues. In [29], Liu et al. proposed Mn–Zn ferrite MNCs - paclitaxel (PTX) nanocores that were coated with a biocompatible PEG-phospholipid layer, with a surface modified by tripeptide of arginine-glycine-aspartic acid (RGD) for improved targeting. The MR contrasting properties were assessed by MR relaxometry and revealed a very high r_2 relaxivity value of 490 $mM^{-1}s^{-1}$, while heat generation efficiency was confirmed by a SAR value of 512 of W g^{-1} Fe. In-vivo MRI experiments showed that in a mouse model bearing a subcutaneous 4T1 breast tumour, MNCs-PTX@RGD could be effectively located in the tumor. Furthermore, when exposed to an AC magnetic field, MNCs-PTX@RGD could easily penetrate the tumour tissue from the tumour-fenestrated vascular networks and induce significant heating (around 43 °C). The achieved temperature elevation accelerated the PTX release from the inner lipid layer, promoting the synergetic thermo-chemotherapy in vivo. Overall anti-tumour efficacy of MNCs-PTX@RGD was improved, resulting in an increased survival time of the mice to more than 46 days. Very recently, Fe_3O_4 nanoparticles for hyperthermia, magnetic resonance imaging, and 5-fluorouracil delivery in colorectal cancer treatment

were fabricated by Yusefi et al. [30] using Punica granatum fruit peel extract (green extract) as a green stabilizer. Thermoresponsive performance of the Fe_3O_4 nanofluids with the green extract was assessed by SAR measurements, with obtained values in a range of 243.12 - 310.97 W g^{-1} depending on the applied field (23.6 - 39.37 kA m^{-1}). Contrasting properties of synthesized NPs were evaluated by MR imaging and relaxometry, with r_2 values in the range of 1.00 - 0.39 ml $\mu g^{-1}s^{-1}$ depending on stabilizer concentration (1 – 4 wt%). Furthermore, 5-FU was successfully loaded onto the Fe_3O_4 NPs with 62 ± 0.3% efficiency, which was followed by 79% drug release within 24 h at pH 7.4. According to in-vitro cytotoxicity tests on CCD112 normal and HCT116 colorectal cancer cell lines, the 5-FU loaded in the Fe_3O_4 NPs showed 29% cancer cell mortality, and only 11% elimination on healthy cells, indicating potential theranostic application in colorectal cancer therapy.

Another type of thermal therapy, photothermal therapy (PTT), utilizes near-infrared (NIR) laser photoabsorbers to generate heat for the thermal ablation of cancer cells. PT therapy is characterized by high specificity, minimal invasiveness, and precise spatial-temporal selectivity compared with conventional therapeutic modalities. For effective PTT, two main factors have to be considered: the incident excitation energy and the dosage; and the photothermal conversion efficiency of the PTT agents. A number of PTT agents, including noble metal nanostructures, nanocarbons, transition metal sulfide/oxide nanomaterials, and organic nanomagnets, have been extensively explored. The optimal PTT agent should exhibit high PTCE (photothermal conversion efficiency), strong absorption of NIR light, efficient targeting capability, and high biocompatibility. Moreover, some of the PTT agents have been designed in combination with imaging moieties, including MRI contract agents, to enable image-guided therapy. For instance, Abed et al. [31] presented the theranostic nanoplatform of Fe_2O_3@Au core-shell nanoparticles, where the Au shell exhibits surface plasmon resonance used in PTT and the magnetic core Fe_2O_3 can be employed as an MRI contrast agent. Furthermore, the magnetic properties of Fe_2O_3 allowed fabricated nanoparticles to be directed to the tumor site by the external magnetic field. The theranostic potential of Fe_2O_3@Au NPs was demonstrated on Balb/c mice bearing the CT26 colorectal tumor model. MR imaging revealed the accumulation of NPs within the tumor, while in-vivo thermometry results demonstrated a significantly higher temperature elevation rate in the tumor after NIR

irradiation than in the non-targeted group (~ 12 °C vs. 8.5 °C). Histological investigations of tumor tissue confirmed the antitumor activity of Fe_2O_3@Au. Tumors treated with only NIR or with an I.V injection of Fe_2O_3@Au show normal cell morphology and similar cell density to the control group. In contrast, a significant reduction in cell density and necrosis areas were observed in the tumor sections after treatment with an I.V injection of Fe_2O_3@Au followed by magnetic targeting and NIR treatment. Similarly, in [32] core-shell gold-coated IONPs (iron-oxide nanoparticles) were synthesized by Eyvazzadeh et al. MR relaxometry investigations of Au@IONPs spherical NPs demonstrated their MR contrasting properties with r_2 relaxivity equal to 95 $mM^{-1}s^{-1}$. MTT results showed no significant cytotoxicity in human nasopharyngeal carcinoma KB cells after incubation with Au@IONPs or by laser irradiation without NPs. In contrast, the photothermal treatment using Au@IONPs, resulted in approximately 70% cell death, depending on an incubation period and the Au@IONP concentration. Tsai et al. [33] demonstrated a rattle-shaped IONP@shell-in-shell nanostructure, created by the deposition of a double layer of Au/Ag alloy on the surface of truncated octahedral iron IONPs with a controlled distance between the layers for broad and strong NIR absorption. Through the exposure of fabricated nanoparticles in an aqueous solution to a 1064 nm diode laser, ~28.3 % heat conversion efficiency was accomplished. The in vitro cell viability at a gold concentration of 100 ppm decreased to ~16 % (from ~85 %) after the NIR irradiation and magnetic attraction. Moreover, a clear accumulation of nanoparticles was visualized by T_2-weighted MR imaging, followed by luminescence imaging that showed that the magnetically targeted nanoparticles treated with NIR laser reduced the U87MG-luc2 cancer cell proliferation in mice. In [34], Hou et al. developed a method to synthesize monodispersed and uniform theranostic Fe_3O_4@SiO_2@GNSs–PEG nanoparticles. The synthesized NPs were composed of a superparamagnetic Fe_3O_4 inner core, silica as the mid-layer, and gold nanoshells on the outside, with a uniform size distribution of less than 100 nm. It was demonstrated that synthesized NPs can serve as both MR and CT imaging contrast agents at different concentrations. Furthermore, a high photothermal effect with a temperature increase of 40 °C was observed (808 nm laser irradiation at 2 W cm^{-2} for 10 min at the concentration of 160 μg ml^{-1}). NPs exhibited low toxicity with viability of more than 90% at the concentration of 200 μg ml^{-1}, which was reduced to 40% under 808 nm laser irradiation at 2 W cm^{-2} for 3 min. Feng et al. [35] proposed a programmed NIR-responsive drug delivery system for combined magnetic tumor targeting, MR imaging, and chemo-

phototherapy. Hollow mesoporous CuS nanoparticles (HMCuS NPs) were used to encapsulate the DOX and then were capped with IONPs to facilitate enhanced PTT effect, controlled drug release, magnetic targeting, and MR imaging. Further surface modification with PEG resulted in increased biocompatibility and prolonged circulation of NPs. The photothermal effect under NIR irradiation was evaluated, and the photothermal conversion efficiency of HMCuS/DOX@IONP-PEG NPs was calculated to be 42.12%. The magnetic resonance contrasting capability of HMCuS/DOX@IONP-PEG was assessed by T_2-weighted MR images, revealing transverse relaxivity r_2 equal to 29.5 mM^{-1} s^{-1}. The anti-tumor efficacy of NPs was evaluated in tumor-bearing mice. The changes of relative tumor volumes after various treatments were recorded as a function of time. The treatment with empty NPs exhibited no tumor regression with tumor volumes increasing rapidly. Moderate growth inhibition was observed in the group treated with free DOX. Finally, the HMCuS/DOX@IONP-PEG NPs under NIR irradiation reduced the tumor growth, and tumors were almost completely suppressed after the magnetic targeting of injected NPs.

2.2. Magnetic Resonance Imaging principles

2.2.1. Nuclear Magnetic Resonance

The nuclear magnetic resonance (NMR) phenomenon arises from the quantum mechanical property of the intrinsic form of angular momentum carried by elementary particles, called spin. Individual unpaired electrons, protons, and neutrons each possess a spin of I = ½, while the spin value of the whole nucleus lies in the range of I = 0 to I = 8 in ½-unit increments.

Due to the Heisenberg Uncertainty Principle, the exact orientation of a particle's angular momentum at any point in time is unknown. However, some limited properties, such as the component of its angular momentum along an arbitrary direction, can be measured with certainty:

$$I_z = \hbar m, \qquad (1)$$

where m is the quantum number, in the case of hydrogen m = -½ or ½, which means that two spin eigen states are observed for ^{1}H nucleus. Nuclei that have a non-zero spin possess a magnetic moment, that is proportional to their angular momentum :

$$\mu_z = \gamma\, I_z \qquad (2)$$

In the absence of an external magnetic field, the two separate spin states are degenerated. Only when a magnetic field is applied does the energy of the individual spins depend on the magnetic moment and two spin eigenstates are revealed (nuclear Zeeman effect). These states are commonly denoted as | +½ ⟩ and | -½ ⟩ and are referred to as spin-up and spin-down, respectively (Figure 1).

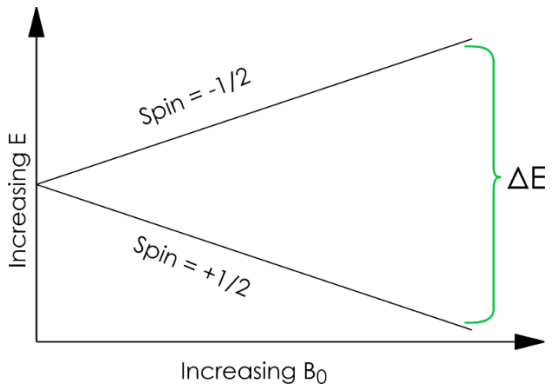

Figure 1 Zeeman splitting for ^{1}H nucleus

Although the lower-energy state is preferred, due to thermal motions at room temperature resultant equilibrium distribution is a compromise predicted by the Boltzmann distribution resulting in only small excess in spin-up sate [36]:

$$\frac{\mathrm{N}\uparrow}{\mathrm{N}\downarrow} = e^{\frac{-\Delta \mathrm{E}}{k_b T}}, \qquad (3)$$

where N↑ and N↓ are the number of spins in the spin-up and spin-down configurations, ΔE is the difference in energy between the two states, k_b is the Boltzmann constant, and T is the absolute temperature.

The energy of an individual proton is given by the dot product of the magnetic moment vector and the static field, i.e.

$$E = -\mu_z \cdot B_0 \qquad (4)$$

Therefore, the energy difference between two eigenstates is described by the equation:

$$\Delta E = \gamma \hbar B_0 \qquad (5)$$

The particle can undergo a transition between the two energy states by the absorption of a photon. The energy of this photon must exactly match the energy difference between the two states. The relationship between the change in energy (Δ E) of an atomic system by emission or absorption of a photon of frequency (ν_0) is described by the equation:

$$\Delta E = \nu_0 h. \qquad (6)$$

The combination of equations 5 and 6 gives the frequency ν_0 that can also be expressed as an angular velocity $\omega_0 = 2\pi\nu_0$:

$$\omega_0 = \gamma B_0 , \qquad (7)$$

which is referred to as Larmor frequency [37].

It should be highlighted that the fact that a hydrogen nucleus has two eigen spin states does not mean that all individual spins reside exclusively in one of those states. All possible states are weighted sums of the two eigenstates, and only if the spin of an individual proton is measured along the direction of the magnetic field, it will be found to be one of the eigenstates. In actual MR experiments, in order to get a measurable MR signal, the total magnetization of many nuclei is taken into account. In the absence of a magnetic field, the angular distribution of spins is spherical as shown in Figure 2. For the individual spins, the energies associated with the orientation are much smaller than the thermal energies, so there is only a slight tendency for them to point exactly in the direction of the field. Therefore, when the magnetic field B_0 is applied, the distribution of spins orientation is skewed slightly toward the field direction, forming non-zero net magnetization *M* (Figure 2, right) [38].

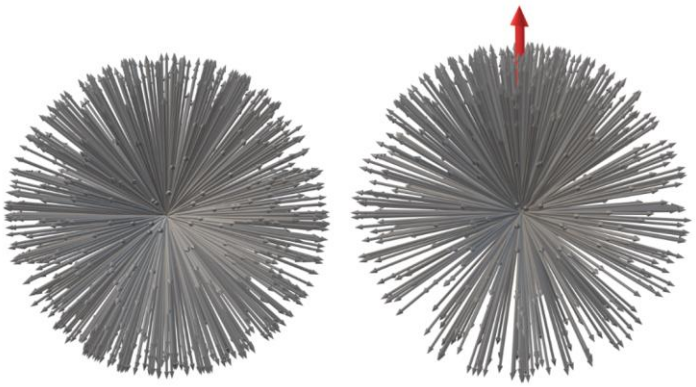

Figure 2 Distribution of spins orientation in the absence (left) and presence (right) of magnetic field B_0

When the sample is placed in the magnetic field, the precession of the individual nuclei starts. Therefore, individual nuclei emit and absorb waves at the Larmor frequency as soon as they are placed in the external magnetic field. Since the distribution of spin directions is even in the transversal plane, the net transversal magnetization at equilibrium is zero.

Nuclear magnetic resonance occurs when the pulse of an alternating magnetic field B_1 at the Larmor frequency is applied to a nuclear spin system. As this frequency lays in the radio wave range, the pulse of the B_1 field is also referred to as the RF pulse. The absorption of energy by the spin system results in tilting the magnetization *M* out of its equilibrium condition and the beginning of its precession around the B_0 field direction, also at the Larmor frequency (Figure 3) [38].

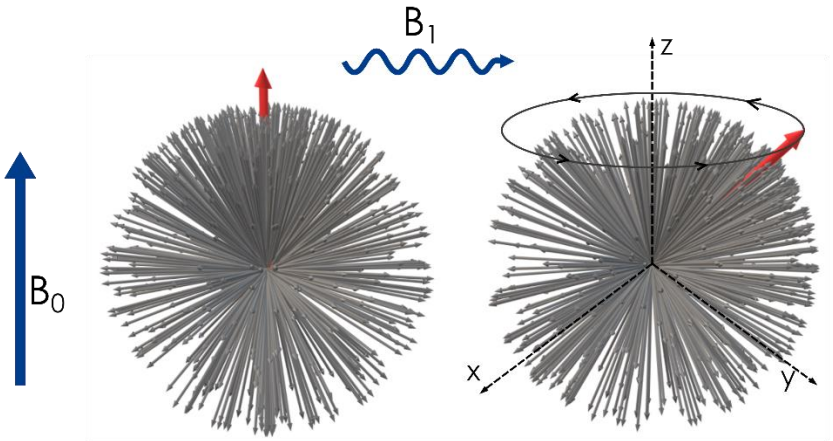

Figure 3 Nuclear Magnetic Resonance

The net magnetization does not precess indefinitely around B after the RF pulse. When the B_1 field is turned off, *M* gradually returns to equilibrium M_0 through magnetic relaxation, as shown in Figure 4.

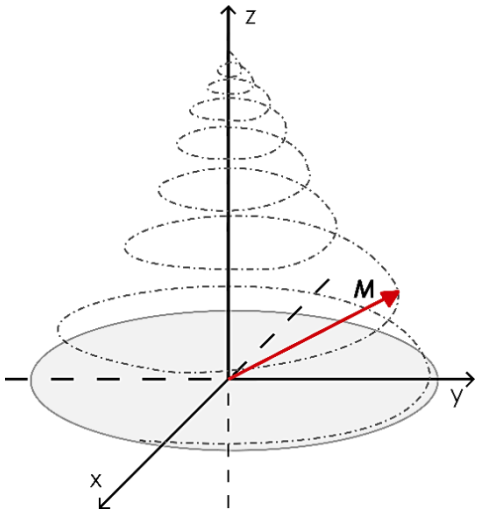

Figure 4 Evolution of net magnetization *M* in the magnetic field

This evolution of net magnetization in the magnetic field, taking into account spin relaxation, is described by the Bloch equation [39]:

$$\frac{d\boldsymbol{M}}{dt} = \boldsymbol{M} \times \gamma \boldsymbol{B} + \frac{\boldsymbol{M_0} - \boldsymbol{M_z}}{\boldsymbol{T_1}} - \frac{\boldsymbol{M_{xy}}}{\boldsymbol{T_2}}, \qquad (8)$$

where M_0 is the equilibrium magnetization, M_z and M_{xy} are longitudinal and transverse magnetization components, and T_1 and T_2 are two relaxation time constants, that reflect the return of *M* to thermal equilibrium after the generation of the NMR signal. T_1 describes the regrowth of longitudinal magnetization, whereas T_2 characterizes the decay of the transverse components.

Bloch equation can be rewritten in the form of explicit expressions for all components:

$$\begin{aligned} \frac{dM_x}{dt} &= \gamma(\boldsymbol{M} \times \boldsymbol{B})_x - \frac{M_x}{T_2} \\ \frac{dM_y}{dt} &= \gamma(\boldsymbol{M} \times \boldsymbol{B})_y - \frac{M_y}{T_2} \\ \frac{dM_z}{dt} &= \gamma(\boldsymbol{M} \times \boldsymbol{B})_z - \frac{M_z - M_0}{T_1} \end{aligned} \qquad (9)$$

The solution of the above equations in the case of static field $B = B_0$ can be simplified to:

$$\begin{aligned} M_x(t) &= e^{-t/T_2}\left[M_x(0)cos\omega_0 t + M_y(0)sin\omega_0 t\right] \\ M_y(t) &= e^{-t/T_2}\left[M_y(0)cos\omega_0 t + M_x(0)sin\omega_0 t\right] \\ M_z(t) &= M_z(0)e^{-t/T_1} + M_0\left(1 - e^{-t/T_1}\right). \end{aligned} \qquad (10)$$

T_1 relaxation, which is also called spin-lattice relaxation or longitudinal relaxation, is the process by which the net magnetization M returns to its equilibrium value M_0. It is characterized by a T_1 time constant reflecting the time it takes for the longitudinal magnetization component M_z to recover approximately to 63% of its initial value after being flipped into the transverse plane by a 90° RF pulse, as shown in Figure 5 (left). For T_1 relaxation to occur, the energy must be dissipated from the spin system. As the spontaneous emission of energy is extremely unlikely in the NMR range of frequencies, the energy transfer is stimulated by locally fluctuating field B_{local}. The source of this field is usually another proton or electron of the same or nearby molecule (so-called 'lattice') that produces the magnetic field fluctuating near the Larmor frequency, allowing transitions between energy levels and the return of the system to the equilibrium state [40]. The z-component of the locally fluctuating field B_{local} adds to the B_0 field, which results in the local variations of Larmor frequency. As individual spins experience a slightly different magnetic field, the dephasing and, as a result, loss of transverse magnetization is observed. This process is called transverse or spin-spin relaxation and is characterized by a T_2 relaxation time constant, which describes the time it takes for the transverse component of magnetization M_{xy} to decay to 37% of its initial value after its generation by flipping the magnetization towards the transverse plane by a 90° RF pulse (Figure 5 right).

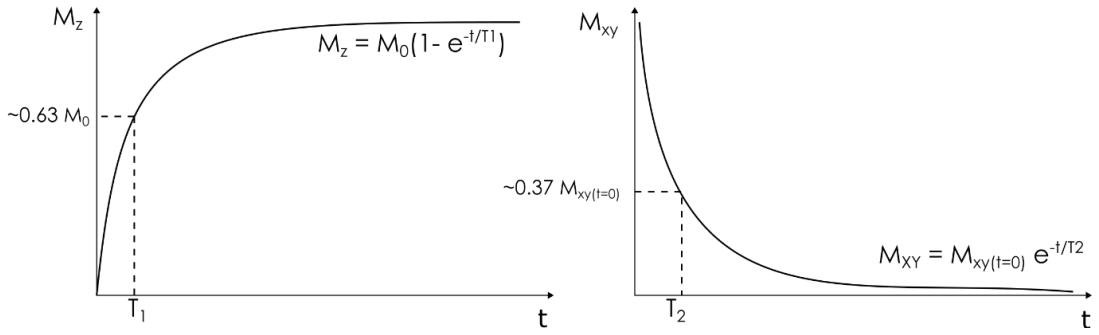

Figure 5 T_1 (left) and T_2 (right) relaxation

The net magnetization after RF pulse excitation is flipped to the transverse plane and precesses at the Larmor frequency. This precession induces changing magnetic flux which according to Faraday's induction law generates changing voltage in the receiver coil. As all protons in the sample precess at the same frequency, the received MR signal is a complex harmonic with only a single frequency peak centered at this frequency.

2.2.2. Magnetic Resonance Imaging

To spatially locate nuclear spins, which allows creating MR images from NMR signals, magnetic field gradients are used. The gradient system consists of three orthogonal coils which produce time-varying gradients G of the main B_0 field in the three directions, which can be described as [41]:

$$B = B_0 + \boldsymbol{G}\,\boldsymbol{r} \qquad (11)$$

As a result, the resonance frequency of the magnetization will vary depending on the location according to:

$$\omega_0(x, y, z) = \gamma(B_0 + G_x x + G_y y + G_z z), \qquad (12)$$

The time-domain signal generated in the receiver coil by the transverse magnetization with applied field gradients can be described as [42]:

$$S(t) = \int M_{xy}(\boldsymbol{r}) B(\boldsymbol{r}) e^{-i\varphi(\boldsymbol{r},t)} d^3r, \qquad (13)$$

where $M_{xy}(\boldsymbol{r})$ is transverse magnetization, $B(\boldsymbol{r})$ is the component of the receive coil B_1-field that lies in the transverse plane ($M_{xy}(\boldsymbol{r})$ and, $B(\boldsymbol{r})$ are complex quantities), $\boldsymbol{r}$ is a spatial variable, and the accumulated phase $\varphi(\boldsymbol{r}, t)$ is defined by:

$$\varphi(\boldsymbol{r}, t) = \gamma \int_0^t \boldsymbol{r} \cdot \boldsymbol{G}(t')dt'. \qquad (14)$$

Defining:

$$\boldsymbol{k}(t) = \frac{\gamma}{2\pi}\int_0^t \boldsymbol{G}(t')\,dt', \qquad (15)$$

with the space in which $\boldsymbol{k}(t)$ resides known as k-space, equation 13 becomes:

$$S(t) = \int M_{xy}(\boldsymbol{r})B(\boldsymbol{r})e^{-i2\pi\boldsymbol{k}(t)\boldsymbol{r}}d^3r, \qquad (16)$$

The signal $S(t)$ is the Fourier transform of the weighted transverse magnetization $M_{xy}(\boldsymbol{r})B(\boldsymbol{r})$, with $\boldsymbol{k}(t)$ the Fourier conjugate variable to the spatial variable. The elements of the k-space are discrete values of the signal S (t) obtained from the sample in the presence of field gradients. The motion of the vector $\boldsymbol{k}(t)$ determines the k-space trajectory, i.e. the manner of writing the elements in the matrix. From the data collected in the k-space, an MR image is obtained by the inverse Fourier transform.

2.3. Contrast Agents for Magnetic Resonance Imaging

To fully appreciate the potential of theranostics, the application of a non-invasive imaging method is essential. The most frequently used imaging methods in medicine include computed tomography CT, ultrasound, PET, SPECT, and magnetic resonance imaging. Each of these methods has its own unique advantages and limitations. In the case of magnetic resonance imaging, the biggest advantage is that it does not use ionizing radiation. In addition, it provides tomographic images with very high spatial resolution and allows for imaging at any depth within the object. However, the greatest constraint of magnetic resonance imaging is its limited sensitivity, which results in insufficient contrast. This problem can be addressed by the use of contrast agents (MRI CAs) [43].

Currently available MR CAs can be classified in different ways according to their various features, such as the presence or absence of metal atoms, magnetic properties, effects on the magnetic resonance image, chemical structure and ligands, or biodistribution and applications [44]. In this section, an overview of MRI CAs with classification based on their biophysical mechanism of action and their effect on MR images is provided.

2.3.1. Relaxation agents I - Paramagnetic CAs

The relaxation in water molecules surrounding the paramagnetic complex is induced by a fluctuating magnetic field generated by the Brownian motion of this complex and is described by the Solomon-Bloembergen-Morgan (SBM) Theory [45], [46]. According to this theory, the observed relaxation rate of the solvent: $\frac{1}{T_{iObs}}$, is the sum of a diamagnetic term: $\frac{1}{T_{iS}}$, that corresponds to the relaxation rate of the solvent nuclei without the contrast agent, and a paramagnetic term: $\frac{1}{T_{iP}}$, which express the relaxation rate enhancement caused by the paramagnetic substance:

$$\frac{1}{T_{iObs}} = \frac{1}{T_{iS}} + \frac{1}{T_{iP}} \qquad i = (1,2). \qquad (17)$$

The paramagnetic contribution is proportional to the concentration C of the contrast agent and is described by the specific proton relaxivity, r_i, that directly refers to how efficiently the paramagnetic centre enhances the relaxation rate of surrounding water protons, and thus to contrasting efficiency:

$$\frac{1}{T_{iObs}} = \frac{1}{T_{iS}} + r_i \cdot C \qquad i = (1,2). \qquad (18)$$

The concentration of contrast agent is given in mmol/l (denoted as mM) rather than mmol/g, thus the commonly used unit for proton relaxivity is $mM^{-1}s^{-1}$.

The relaxation of water protons originates from the dipole-dipole interactions between the proton nuclear spins and the fluctuating local magnetic field caused by paramagnetic centre unpaired electron spins. Three contributions to the relaxation can be distinguished [47] [48] [49]:

1. Inner-sphere relaxation, $\left(\frac{1}{T_{iP}}\right)^{IS}$, where a water ligand directly bound to the metal (water protons in the inner coordination sphere) is relaxed and transmits the relaxation effect through exchange with bulk water.

2. Second-sphere relaxation, $\left(\frac{1}{T_{iP}}\right)^{2nd_S}$, where hydrogen-bonded water molecules in the second coordination sphere, or exchangeable hydrogen atoms (such as O–H, N–H) undergo relaxation and exchange.

3. Outer-sphere relaxation, $\left(\frac{1}{T_{iP}}\right)^{OS}$, where water molecules diffusing near the complex compound can also undergo relaxation:

$$\left(\frac{1}{T_{iP}}\right) = \left(\frac{1}{T_{iP}}\right)^{IS} + \left(\frac{1}{T_{iP}}\right)^{2nd_S} + \left(\frac{1}{T_{iP}}\right)^{OS}. \qquad (19)$$

As it is difficult to experimentally differentiate between second-sphere and outer-sphere water, those groups are usually considered together as the outer-sphere water molecules. Additionally, in aqueous solutions, in most cases, the exchange of protons between the bulk water and the coordination sphere is so rapid that the observed proton relaxation rate is the weighted average of the relaxation rates in the inner and outer spheres.

Inner sphere contribution

The inner sphere contribution to proton relaxivity arises from the chemical exchange of the coordinated water protons with the bulk. According to the Solomon-Bloembergen-Morgan (SBM) theory, the main factors influencing proton inner sphere relaxivity are:

1. The number of water molecules in the inner sphere, q;

2. The kinetics of water exchange between the inner sphere and the bulk, expressed by exchange rate $k_{ex} = 1/\tau_m$, where τ_m is the mean residency time of the water ligand;

3. The rotational dynamics of the molecule, described by a rotational correlation time τ_R;

4. The electron spin S of the complex;

5. The electronic relaxation times T_{1e} and T_{2e}

The longitudinal and transverse inner sphere relaxivities, r_1^{IS}, and r_2^{IS}, of the bulk solvent nuclei are given by equations 20 and 21 [50]:

$$r_1^{IS} = \frac{P_m}{T_{1m}+\tau_m}, \qquad (20)$$

$$r_2^{IS} = \frac{P_m}{\tau_m}\left(\frac{T_{2m}^{-1}\left(\tau_m^{-1}+T_{2m}^{-1}\right)+\Delta\omega_m^2}{\left(T_{2m}^{-1}+\tau_m^{-1}\right)^2+\Delta\omega_m^2}\right), \qquad (21)$$

where: $P_m = \frac{q}{[H_2O]}$, is the mole fraction of bounded water molecules where [H_2O] is the water mM concentration, and $\Delta\omega_m$ is the chemical shift difference between bound and bulk water.

The relaxation of bound water protons, $\left(\frac{1}{T_{im}}\right), (i = (1,2))$, is governed by the magnetic field-dependent dipole-dipole and scalar or contact interactions. The scalar interaction is influenced by electron spin relaxation and water exchange, and generally, its contribution is negligible for longitudinal relaxation. Thus, the T_1- effect arises mostly from dipolar contribution, while the T_2-effect from both dipolar and scalar interactions.

Relaxation rates, $\frac{1}{T_{im}}, \left(i = (1,2)\right)$ are described by the SBM equations of paramagnetic relaxation theory (equations 22 and 23). Here, r_{MH} is the distance between metal ion and hydrogen, γ_I is a nuclear gyromagnetic ratio, g_e is the electron g factor, μ_B is the Bohr magneton, μ_0 is the vacuum permeability, and ω_s and ω_H are the Larmor frequencies of the electron and proton. $\left(\frac{A}{\hbar}\right)$ is the hyperfine or scalar coupling constant between the electron of the paramagnetic center and the proton of the coordinated water.

$$\frac{1}{T_{1m}} = \underbrace{\frac{2}{15}\left(\frac{\mu_0}{4\pi}\right)^2 \frac{\gamma_I^2 g_e^2 \mu_B^2 S(S+1)}{r_{MH}^6}\left[\frac{7\tau_{c2}}{1+\omega_s^2\tau_{c2}^2}+\frac{3\tau_{c1}}{1+\omega_H^2\tau_{c1}^2}\right]}_{\text{Dipolar coupling}} + \underbrace{\frac{2S(S+1)}{3}\left(\frac{A}{\hbar}\right)^2\left(\frac{\tau_{e2}}{1+{\omega_s}^2{\tau_{e2}}^2}\right)}_{\text{Scalar coupling}}, \qquad (22)$$

$$\frac{1}{T_{2m}} = \underbrace{\frac{1}{15}\left(\frac{\mu_0}{4\pi}\right)^2 \frac{\gamma_I^2 g_e^2 \mu_B^2 S(S+1)}{r_{MH}^6}\left[4\tau_{c1}+\frac{13\tau_{c2}}{1+\omega_s^2\tau_{c2}^2}+\frac{3\tau_{c1}}{1+\omega_H^2\tau_{c1}^2}\right]}_{\text{Dipolar coupling}} + \underbrace{\frac{S(S+1)}{3}\left(\frac{A}{\hbar}\right)^2\left(\frac{\tau_{e2}}{1+{\omega_s}^2{\tau_{e2}}^2}+\tau_{e1}\right)}_{\text{Scalar coupling}}, \qquad (23)$$

Moreover, the correlation times that are characteristic of the relaxation processes are expressed as:

$$\frac{1}{\tau_{ci}} = \frac{1}{\tau_R} + \frac{1}{\tau_m} + \frac{1}{T_{ie}}; \qquad i = (1,2), \quad (24)$$

$$\frac{1}{\tau_{ei}} = \frac{1}{\tau_m} + \frac{1}{T_{ie}}; \qquad i = (1,2), \qquad (25)$$

where τ_R is the rotational correlation time, τ_m is the water residency time, and T_{ie} $(i = (1,2))$ is the electronic relaxation time.

The electronic relaxation rates depend on the applied magnetic field. For the most commonly used Gd(III) and Mn(II) complexes, electronic relaxation times are interpreted in terms of zero-field splitting interactions (ZFS) and can be described (with the low field limiting value of the electronic relaxation rate) by the equations 26 and 27 [51]:

$$\left(\frac{1}{T_{1e}}\right) = \frac{12}{5}\Delta^2\tau_v\left(\frac{1}{1+\omega_S^2{\tau_v}^2} + \frac{1}{1+4\omega_S^2{\tau_v}^2}\right) \qquad (26)$$

$$\left(\frac{1}{T_{2e}}\right) = \frac{12}{10}\Delta^2\tau_v\left(3 + \frac{5}{1+\omega_S^2{\tau_v}^2} + \frac{2}{1+4\omega_S^2{\tau_v}^2}\right), \quad (27)$$

where τ_v is the correlation time for the modulation of the zero-field splitting interaction and Δ^2 is the mean square zero-field splitting energy. Therefore, electronic relaxation rates decrease with the square of the applied field and eventually $\frac{1}{T_{1e}}$ becomes much smaller than $\frac{1}{\tau_R}$, and rotation contribution dominates the overall correlation time.

The combination of equations 22 and 23 with the equations for electron spin relaxation (equations 26 and 27) constitutes a complete microscopic scale theory of the observed paramagnetic relaxation rate enhancement.

Second and Outer sphere contribution

Second-sphere relaxivity refers to complexes that have water molecules or exchangeable protons that have a residency time longer than the diffusion lifetime in the

second coordination sphere. Therefore, its contribution to relaxation enhancement can be described by the dipolar term of equations for inner sphere relaxivity [52].

Outer sphere relaxivity is mainly described by translational diffusion due to the Brownian motion of free water molecules that interact with the electronic spins of the metal ions through dipolar intermolecular interactions. This process is described by equation 28 [53] [54]:

$$\frac{1}{T_1} = \frac{32\pi}{405}\left(\frac{\mu_0}{4\pi}\right)^2 \frac{N_A[M]}{dD}\gamma_I^2\gamma_S^2\hbar^2 S(S+1)[j_2(\omega_I - \omega_S) + 3j_1(\omega_I) + 6j_2(\omega_I + \omega_S)], \quad (28)$$

where d is the distance of the closest approach of spins I and S (solvent protons and paramagnetic complex), N_A is Avogadro's number, $[M]$ is the molar concentration of the paramagnetic contrast agent, and D is the diffusion constant for relative diffusion. The spectral densities $j(\omega)$ are obtained from the Fourier transform of the correlation function g(t) [50].

T_1 relaxation enhancement produced by paramagnetic complex depends directly on the quantum spin number as $S(S+1)$ function, and inversely on the distance between the metal ion and the proton of the water. Gadolinium (III) with $S = 7/2$ and manganese (II) or iron (III) with S = 5/2 have been the most widely investigated as contrast agents [52]. Due to their high toxicity and undesirable biodistribution with accumulation in the spleen, liver, and bones, Mn and Gd cannot be used in their ionic forms. For that reason complexes with high thermodynamic and kinetic stability, chelates, are clinically available. Nonspecific contrast agents based on Gd(II) or Mn(II) chelates usually present similar transverse and longitudinal relaxivities, however, they are mostly used as T_1 contrast agents [43]. The $\frac{r_2}{r_1}$ ratio for those CAs is low, below 5, which indicates that they can be successfully applied for signal amplification in T_1 weighted images.

Relaxivity values for the most frequently clinically used paramagnetic contrast agents are presented in Table 1. It's worth noting that all clinically available paramagnetic CAs are based on gadolinium. To date, only one manganese-based agent, Teslascan™, has been clinically approved. However, due to toxicity concerns and lack of sales, it has been withdrawn from sale [55].

Table 1 Clinically available paramagnetic contrast agents

Chemical name	Trade name	Mean r_1 [$mM^{-1}s^{-1}$] at 7T* [56] [57]	Mean r_1 [$mM^{-1}s^{-1}$] at 3T * [56] [57] [58]
Gd-DTPA	Magnevist™	3.30	3.3 - 3.7
Gd-DOTA	Dotarem™	3.20	3.3 - 3.5
Gd-DO3A-butrol	Gadovist™	4.70	4.9 - 5.0
Gd-EOB-DTPA	Primovist™	4.8	5.4 - 6.2
Gd-DTPA-BMA	Omniscan™	3.50	3.6 - 4.0
Gd-HP-DO3A	ProHance™	3.30	3.5 - 3.7
Gd-BOPTA	MultiHence™	4.30	5.1 – 6.3

* relaxivities measured in human plasma

2.3.2. Relaxation agents II – Superparamagnetic CAs

The shortening of T_2 relaxation time induced by superparamagnetic nanoparticles is determined by the translational diffusion of water molecules near the unpaired electrons. Therefore, the relaxation enhancement caused by the presence of superparamagnetic nanoparticles is subjected to the outer-sphere SBM theory combined with the Curie relaxation theory and can be described by equation 29:

$$\frac{1}{T_2} = \frac{256\pi^2\gamma^3}{405}\frac{V^* M_S^2 a^2}{D\left(1+\frac{L}{a}\right)}, \quad (29)$$

where γ is the proton gyromagnetic ratio, V^*, M_S and a are the volume fraction, saturation magnetization, and the radius of iron oxide core, respectively; L is the thickness of a surface coating and D is the diffusion contrast of water molecules [59] [60] [61].

Superparamagnetic Iron Oxides (SPIOs) are often categorized according to size as ultrasmall superparamagnetic iron oxide particles (USPIOs), with a diameter smaller than 20 nm, and superparamagnetic iron oxide (SPIOs), with a diameter usually below 100 nm. SPIOs consist of a single magnetic domain, which is characteristic for nanoparticles of volume below the superparamagnetic limit, in which it is more energetically favorable to support the external magnetostatic energy of the single domain state than to create a domain structure [62]. The implications of the superparamagnetic state are as follows: in the absence of the external magnetic field, the net magnetic moment is zero; in applied

external field superparamagnetic nanoparticles behave like paramagnets, but with much larger susceptibility and therefore larger saturation magnetization, which makes them efficient T_2 CAs [63] [64]. Clinically approved superparamagnetic contrast agents are based on iron oxides. Table 2 summarizes the most frequently used superparamagnetic CAs in clinical practice.

Table 2 Clinically available superparamagnetic contrast agents

Generic name	**Trade name**	**Core size [nm]**	**Mean r_2 [$mM^{-1}s^{-1}$] at 1.5 T** [65] [66] [67]
Ferumoxide	Feridex™	4.96 – 5.0	33 - 129
Ferucarbotran	Resovist™	4.0 - 4.2	95- 189
Ferumoxtran	Sinerem™	5.85 - 5.90	65
Ferumoxytol	Faraheme™	n.a.	89

Taking into consideration the effect the contrast agent has on the MR image, relaxation CAs can be classified either as positive or negative contrast agents. Positive contrast agents shorten the T_1, resulting in the appearance of brighter, signal-enhanced areas on T_1-weighted images. Opposingly, negative contrast agents shorten T_2 relaxation time. As an effect, darker spots on T_2-weighted images are observed [44]. Positive contrast agents include mostly the paramagnetic CAs mentioned above, as they effectively shorten T_1. Superparamagnetic nanoparticles (mostly iron oxide NPs) are considered to be negative contrast agents. However, the r_2/r_1 ratio increases with the size of superparamagnetic nanoparticles, thus ultra-small SPIONs with sizes below 10 nm can also effectively modify T_1 relaxation and produce positive contrast with appropriate imaging sequence parameters [43].

2.3.3. Chemical exchange saturation transfer CAs

The principle of CEST imaging is very well described by its name: chemical exchange saturation transfer. Exchangeable solute protons from different molecules that resonate at a frequency different than the bulk water protons are selectively saturated using an RF pulse. This magnetic saturation is subsequently spontaneously transferred to bulk water via chemical exchange of the excited protons with water protons. This leads to a slight attenuation of the water MR signal arising from bulk water. Because of the very

low concentration of solute protons, which is in the range of single μM to mM, a single transfer of saturation would be insufficient to produce any noticeable change in the signal intensity of bulk water [68] [69]. Therefore, the observable change in MR signal from water is created by the continuous transfer of excited ^{1}H protons, which causes the build-up of saturation in water. This means that each saturated proton undergoes the exchange with water and is replaced with another unsaturated ^{1}H proton, that can be subsequently saturated and further exchanged. This implicates that the substantial enhancement of the saturation effect, that is detectable on the water signal, is induced if the solute protons have a sufficient exchange rate, and the saturation time is long enough, in the range of seconds [69] [70].

The CEST mechanism enhances the sensitivity of MRI, allowing the detection of low concentration molecules indirectly, through the water signal, which makes this technique applicable for molecular and cellular imaging. The simplest classification of CEST agents includes two groups: DiaCEST and ParaCEST, and is mostly related to the chemical shift difference between the solute and bulk water. For DiaCEST, this difference usually lies in the range of 0 - 5 ppm [68]. DiaCEST proton exchange groups are mostly limited to amide, amine, or hydroxyl groups [71] [72] [73] that can be endogenous, present in the body, or exogenous, administered as a contrast agent. The biggest advantage of DiaCEST agents of the endogenous type is that the CEST imaging can be performed using modifications of the existing pulse sequences, without introducing any exogenous substance that could cause adverse effects [70]. The small chemical shift difference of DiaCEST agents is, however, their biggest limitation, as it leads to partial saturation of the signal arising from a bulk water pool and also implies that very slow exchange rates are required. This can be addressed by increasing chemical shift separation between the two exchanging pools by using exogenous ParaCEST agents. The most explored ParaCEST agents include complexes of paramagnetic lanthanide ions, such as Eu^{3+} Tm^{3+} and $Yb^{3+,}$ and paramagnetic transition metal ions: Fe, Co, Ni. Depending on the complex, ParaCEST agents' chemical shift values are in the range of +500 to −720 ppm with respect to the MR frequency of water [74] [75].

In the case of ParaCEST agents, the translation to human studies may be difficult because of the technical obstacles resulting in high specific absorption rates and also due to concerns related to the toxicity of these agents. On the other hand, the application of

endogenous DiaCEST [76] [77] and some exogenous DiaCEST agents like nutrients, including glucose and its derivatives [78] [79], to human subjects is already possible. Furthermore, some of the clinically approved CT contrast agents including iopamidol, iopromide, iodixanol, ioversol, iobitridol, and iohexol, have been investigated as CEST agents on animal models. Those agents are routinely used in CT imaging at relatively high doses, so the translation to clinical CEST imaging may be possible, especially since it brings additional information about extracellular pH changes in the accumulation site, which is an important indicator in many diseases (for example Warburg effect in tumours) [80]. Another very interesting potential application of exogenous diaCEST, that is possible in human subjects, is the imaging of drugs distribution. In particular, many anticancer drugs, including Gemcitabine, Cytarabine, Decitabine, Azacitidine, Fludarabine, Methotrexate [81], Pemetrexed [82], and Olsalazine [83], but also some anti-inflammatory, neuroprotective, and cardiovascular drugs, were investigated in the context of off-label image-guided drug delivery. With the technological advances, most importantly shifting to higher field strengths, CEST efficiency is expected to be improved, and therefore its clinical applicability will expand.

The CEST contrast agents are used to visualize the distribution of molecules other than water, such as chemical compounds and metabolites related to physiological function and pathological conditions, in body tissues, rather than to increase the contrast between anatomical structures [69]. Because CEST contrast agents can be turned on on-demand with the saturation pulse, the effect on MR image could be visualized by the subtraction of an image acquired after and before CEST activation. However, in order to eliminate the effects of the magnetization transfer contrast and direct water saturation, the CEST effect is visualized by comparison of the signal reduction caused by the saturation pulse applied at the desired spectral location (+τ ppm with respect to water signal) with the water signal reduction obtained with the saturation pulse applied to the opposite spectral location (-τ ppm). This way, a spatial distribution map of the investigated compound is created and overlaid on an anatomical image.

2.3.4. Direct detection CAs

Relaxation and CEST contrast agents described above induce the change in local MR signal at the site of their accumulation either by shortening the relaxation rates of bulk water or by saturation transfer. Another group of contrast agents for MRI are CAs that can be detected directly by the detection of a signal arising from nuclei other than hydrogen. In theory, any nuclei with a nonzero spin produce an MR signal, however, due to factors such as the natural abundance of the isotope, relative sensitivity, and quadrupolar relaxation, only a few of them are available for magnetic resonance spectroscopy and imaging. Those nuclei are ^{13}C, ^{23}Na, ^{31}P, ^{19}F, and hyperpolarized ^{3}He, ^{129}Xe, ^{13}C, ^{15}N, and ^{6}Li [52]. As the two fluorinated compounds were investigated in this thesis, only fluorine MRI will be described with more details.

Among the mentioned nuclei, fluorine-19 is perfect for in-vivo imaging applications. Interestingly, the first ^{19}F imaging-related study, using NaF and perfluorotributylamine, was published in 1977 [84], so already at the beginning stage of human MRI method development. However, only the later advancements in both MR hardware and the chemistry of fluorinated probes made the in-vivo application of ^{19}F-MRI possible [85]. As mentioned above, there are several properties of ^{19}F that make it a perfect tracer for in-vivo imaging. Fluorine-19 has an I = ½ spin, which implies that it does not undergo quadrupolar relaxation. Also, its gyromagnetic ratio γ has a value very similar to that of ^{1}H (40.06 MHz/T for ^{19}F vs. 42.58 MHz/T for ^{1}H), which means that it resonates at a frequency very close to that of ^{1}H ($\omega = \gamma \cdot B_0$), and that the standard ^{1}H instruments can be used, with only minor modifications. As the MR signal is proportional to $\gamma^3(I)(I+1)$, and ^{19}F isotope has 100% natural abundance, its relative sensitivity is very high, equal to 0.83 (the relative sensitivity of ^{1}H is 1), which is significantly higher than the relative sensitivities of other MR active nuclei, such as ^{31}P (0.066), ^{13}C (0.016) and ^{23}Na (0.083). Last but not least,^{19}F almost does not appear physiologically in the human body. It is present at higher concentrations mostly in the bone matrix and in teeth, where it is strongly immobilized, and therefore is characterized by very short spin-spin relaxation time and is not detectable by conventional MRI. This lack of background signal provides an excellent contrast-to-noise ratio and specificity for the exogenous ^{19}F probes that can be introduced as contrast agents. However, even for ^{19}F nuclei, the factor that strongly

limits its application is the low signal-to-noise ratio due to the much smaller number of nuclei available for imaging than for standard ^{1}H anatomical imaging, where nearly 2/3 of the nuclei present in the body contribute to the MR signal. Therefore, to increase SNR and allow detection in-vivo, agents with very high ^{19}F content per molecule are required to ensure sufficient tissue concentration [86] [87].

The group of chemical compounds that are the most successfully used in ^{19}F MRI are perfluorocarbons (PFCs). Perfluorocarbons have a chemical structure similar to biologically present compounds, such as alkanes, with all hydrogen atoms substituted by fluorine [85]. Most frequently used PFCs are PFCE (perfluoro-15-crown-5-ether), that contains 20 fluorine atoms per one molecule, PERFECTA (1,3bis[[1,1,1,3,3,3hexafluoro2(trifluoromethyl)propan2yl]oxy]2,2bis[[1,1,1,3,3,3hexafl uoro2(trifluoromethyl)propan2yl]oxymethyl]propane), with 36 chemically equivalent fluorine atoms [88], and PFOB (perfluorooctyl bromide), bearing 17 ^{19}F atoms. All PFCs are hydrophobic and lipophobic, therefore, for biological applications, PFCs emulsions must be stabilized with surfactants or encapsulated in polymer nanoparticles to achieve the required biocompatibility and stability. In general, PFC probes are proven to be non-toxic and biologically and chemically inert. Furthermore, they can be internalized into different cells such as macrophages, stem cells, and immune cells [89] [90]. Preclinical applications of ^{19}F contrast agents include mostly cell tracking [91] [92] [93] [94], inflammation imaging in cardiac [95] [96] [97] and neural [98] [99] [100] disease models, inflammation associated with tumors [101] [102] and drug delivery observations [103] [104] [22].

The major issue with the translation of PFCs applications to clinical practice is their prolonged retention. The majority of available perfluorocarbons have very long biological half-lives, even over 100 days [105]. Therefore, the slow biological clearance of PFCs leads to complications with regulatory approvals that are now being observed regarding gadolinium deposition [106].

Regarding the effect that direct detection or X-nuclei contrast agents exert on MR images, those CAs are referred to as hot-spot agents. In this case, standard ^{1}H MR images as well as images of another nucleus with a different resonance frequency, for example, ^{19}F, are acquired in one imaging session. Subsequently, the X-nucleus image is overlaid on

the ^{1}H image, where the standard MR image serves as the reference for the spatial localization of the signal arising from the x-nucleus.

Chapter 3

Materials and methods

In this chapter, the materials and experimental apparatus relevant to the studies presented in this thesis are described. First, a description of the investigated nanocarriers and standard substances is provided. Next, the experimental apparatus, i.e. high-field MRI scanner and used coils, is briefly presented, which is followed by the description of imaging sequences used in the study. Finally, the methods for specific relaxivity and signal-to-nose ratio calculations are outlined.

3.1. Materials

3.1.1. Nanocapsules for drug delivery

a) Gadolinium labelled polyelectrolyte nanocarriers

In this group, two types of nanocarriers were investigated: with nanoemulsion and polymeric cores formed with the ionic surfactant AOT (Docusate sodium salt), or with AOT and PCL (polycaprolactone), respectively. The nanocarrier shells were formed via a layer-by-layer technique with biodegradable polyelectrolytes: PLL (Poly lysine), PLL-Gd (Gadolinium-labelled Poly-L-lysine), and PGA (Poly-L-glutamic acid). Moreover, an anticancer drug (Paclitaxel) was encapsulated in the formed nanocarriers of both types. The schematic representation of the nanocarriers' composition is illustrated in Figure 6. The average sizes of nanocarriers were: 161 nm for polymeric, and 142 nm for nanoemulsion type, respectively [107]. The presence of Gd ions in the structure of the shell allows the observation of the distribution of nanocarriers by the contrast changes in the site of accumulation by MRI, while the therapeutic effect is achieved by the release of the drug.

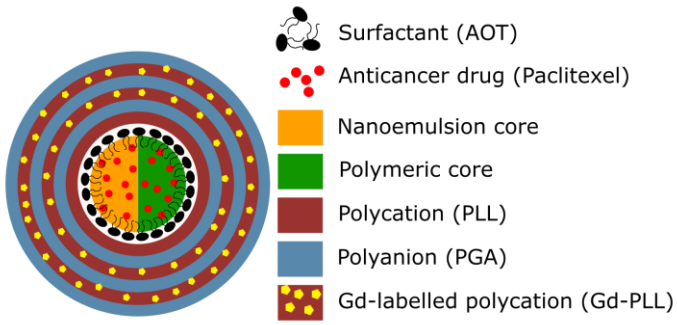

Figure 6 Gadolinium labelled polyelectrolyte nanocarriers composition

For magnetic resonance experiments, two sets of samples containing nanocarriers of each type were prepared for T_1 and T_2 relaxation analysis. Samples containing nanocapsules with a nanoemulsion core were denoted as AOT/PLL-Gd, while those with nanocarriers with a polymeric core as PCL/AOT/PLL-Gd. Also, for each type of nanocarrier, samples without Gd were prepared for reference. The samples' description is presented in Table 3.

Table 3 Samples with nanocarriers containing Gd as MRI contrast agent

Sample	Type of core	Gd concentration [mM]
AOT/PLL	nanoemulsion	0
AOT/PLL-GD 1	nanoemulsion	0.0036
AOT/PLL-GD 2	nanoemulsion	0.0073
AOT/PLL-GD 3	nanoemulsion	0.018
PCL/AOT/ PLL	polymeric	0
PCL/AOT/ PLL-GD 1	polymeric	0.0036
PCL/AOT/ PLL-GD 2	polymeric	0.0073
PCL/AOT/ PLL-GD 3	polymeric	0.018

b) Magnetically responsive polycaprolactone nanocarriers

The magnetically responsive nanocarriers were composed of drug-loaded polymer nanoparticles (Paclitaxel-PCL) coated with a multilayer of poly-L-glutamic acid (PGA) and superparamagnetic iron oxide nanoparticles (SPIONs). The PCL nanocarriers with a model anticancer drug were formed by the spontaneous emulsification solvent evaporation (SESE) method. Further functionalization was achieved by magnetically responsive multilayer shell formation via the layer-by-layer (LbL) method [108] [109]

[110]. In this group, two types of NCs were formed with (samples MR NC) or without AOT (samples MR NCx) surfactant in one of the shell layers. This addition of AOT results in the creation of the AOT/PLL interfacial complex instead of the PLL layer. The resulting compositions of nanocarriers are illustrated in Figure 7, with an average size of about 120 nm. Due to the presence of SPIONs, these hybrid nanodevices can be used as MRI-guided drug-delivery systems based on enhanced permeability and retention (EPR) [111] effect but can also be directed to the site of action by the external magnetic field. The therapeutic effect can also be achieved in two ways: by the release of the drug to the site of action and by magnetic hyperthermia [112].

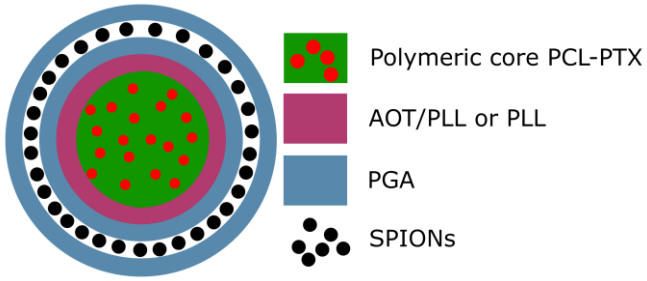

Figure 7 SPIONs labelled polyelectrolyte nanocarriers composition

For analysis of MRI contrasting properties and T_1 and T_2 relaxation measurements, two sets of agarose gel phantoms with varying concentrations of nanocarriers were prepared. Also, a reference sample containing SPIONs–free nanoparticles was measured for comparison. In total, eight samples with different Fe_3O_4 concentrations (Table 4) were investigated for each set.

Table 4 Samples with nanocapsules containing Fe_3O_4 as MRI contrast agent

Sample	Fe_3O_4 concentration [mM]	Sample	Fe_3O_4 concentration [mM]
reference	0	**reference**	0
MR NC 128	0.015	**MR NCx 128**	0.016
MR NC 64	0.029	**MR NCx 64**	0.031
MR NC 32	0.058	**MR NCx 32**	0.062
MR NC 16	0.116	**MR NCx 16**	0.124
MR NC 8 A/B	0.232	**MR NCx 8 A/B**	0.248
MR NC 4	0.464	**MR NCx 4**	0.497
MR NC 2	0.929	**MR NCx 2**	0.993
MR NC 0	1.857	**MR NCx 0**	1.986

c) Nafion™-Based Theranostic Nanocapsules

Nafion™ (N-(3-acetylphenyl)-4-(2-phenylethyl)thieno[3,2-b]pyrrole-5-carboxamide) - based nanoemulsion core – polyelectrolyte shell nanocarriers were prepared by the encapsulation of nanoemulsion droplets in a polyelectrolyte multilayer shell. The liquid core of capsules (nanoemulsion droplets) was formed with AOT (docusate sodium salt) as a surfactant. The multilayer shell was formed by the layer-by-layer method from polyelectrolytes: PLL as cationic and Nafion™ as anionic. The surface of positively charged nanocarriers (with PLL as an outer layer) was coated with the pegylated polyelectrolyte, PGA-g-PEG. Figure 8 illustrates the nanocapsule's composition with an average size of ~170 nm. The utilization of Nafion™ polymer as the component of the shell enables the observation of nanocapsule's distribution via Fluorine Magnetic Resonance Imaging (^{19}F-MRI) due to its high fluorine content [113].

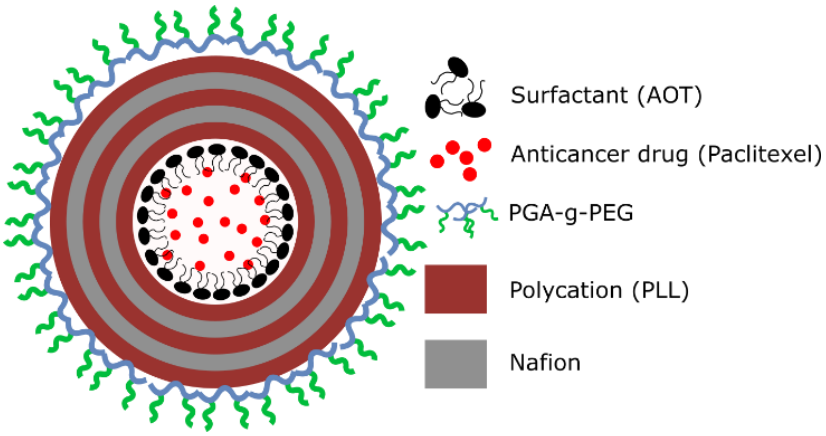

Figure 8 Nafion™ - Based Theranostic Nanocapsules composition

For experiments concerning visualization of the theranostic nanocapsules, the first four samples containing different concentrations of NafionTM were prepared in order to estimate the minimum concentration of NafionTM that would be possible to be visualized in reasonable acquisition time in our setup. Next gel phantom with theranostic nanocapsules was prepared. The summary of samples with different NafionTM content can be found in Table 5.

Table 5 Samples with different Nafion™ concentration

Sample	Relative Concentration of 20% Nafion® Solution in H2O (mL)
N0	1.000
N1	0.100
N2	0.010
N3	0.005

d) Polyelectrolyte nanocapsules with 5-FU

5-Fluorouracil loaded nanocarriers were synthesized by the adoption of the method applied in the synthesis of nanocapsules with relaxation contrast agents and Nafion™, i.e. encapsulation of liquid cores in a polyelectrolyte multilayer shell. Liquid cores of nanocarriers were prepared by the addition of a solution of 5-fluorouracil (45 mg/ml) and AOT (330mg/ml) in DMSO to the poly-L-lysine solution during stirring by a magnetic stirrer. Subsequently, such nanocores were encapsulated with polyaminoacids multilayer shells via the layer-by-layer method with saturation technique. A fixed volume of 5-FU loaded nanocores was added to the oppositely charged polyaminoacids solution and the formation of each consecutive layer was confirmed by the zeta potential measurements. For the shell assembly, the following polyaminoacids were used: PLL as a polycation and PGA as a polyanion. Additionally, PGA-g-PEG pegylated polyanion was used to form a pegylated external layer. The resulting composition of nanocores and the whole nanocapsules is presented in Figure 9, with the average nanocore size of 80 nm and a pegylated nanocapsule of 205 nm. To confirm the efficiency of encapsulation and to assess the possibility of obtaining a sufficient signal-to-noise ratio for imaging of the spatial distribution of 5-fluorouracil loaded nanocapsules, ^{19}F MR spectroscopy and imaging were performed on liquid 5-fluorouracil cargo enclosed in an AOT/PLL interfacial layer forming the nanocore [114].

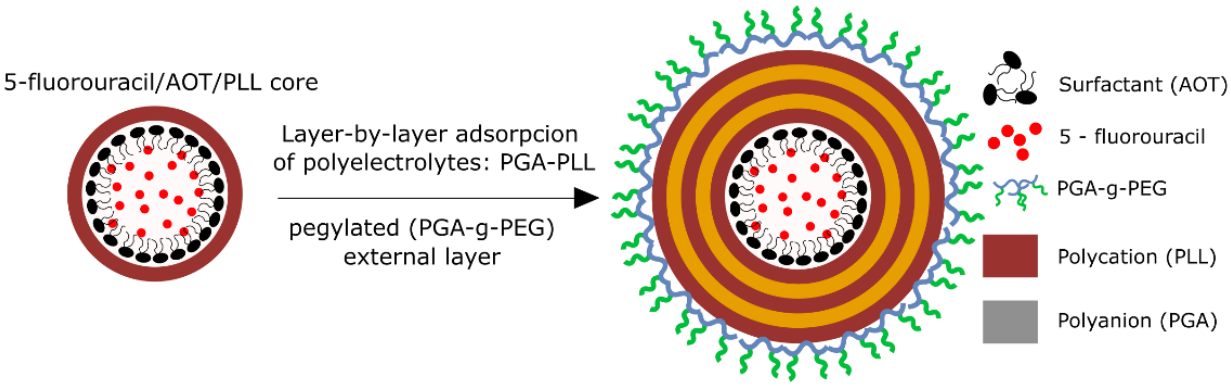

Figure 9 The composition of 5-fluorouracil loaded theranostic nanocapsules

3.1.2. Core-shell nanoparticles for MRI-guided chemo/NIR photothermal therapy

Core-shell nanoparticles for MRI-guided chemo/NIR photothermal therapy consisted of monodisperse Fe_3O_4 nanoparticles encapsulated in a SiO_2 shell. This shell was decorated with small Au nanoparticles (average size of 4 nm) and functionalized by cisplatin (cPt) using a 16-mercaptohexadecanoic acid (16-MHDA) linker [115].

In order to evaluate the theranostic potential of studied nanoparticles, we investigated only the magnetically active element of the nanoparticle: Fe_3O_4@SiO_2 as it was the only component exhibiting strong magnetic properties and therefore causing local perturbations of the magnetic field. In addition, Au nanoparticles didn't form a continuous shell around the Fe_3O_4@SiO_2 NPs, which could limit the access of water molecules to the surface of the active element.

In this group of materials several variations on NPs were investigated:

- NPs with spherical-shaped Fe_3O_4 core of an 11 nm average size, coated by a 10 nm SiO_2 shell
- NPs with cubic-shaped Fe_3O_4 core of an 18.5 nm average size, coated by a 10 nm SiO_2 shell
- NPs with cubic-shaped Fe_3O_4 core of an 18.5 nm average size, coated by a 2 nm SiO_2 shell

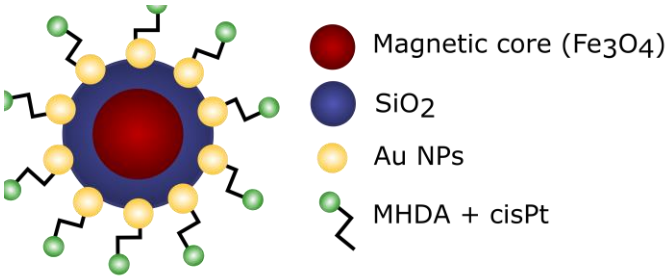

Figure 10 Core-shell nanoparticles for MRI-guided chemo-photothermal therapy

The MRI contrasting efficiency of those three variations was tested using sets of samples with varying concentrations of nanocarriers. The summary of measured core-shell nanoparticles is presented in Table 6.

Table 6 Samples with core-shell NPs with Fe_3O_4 as MRI contrast agent

Spherical Fe_3O_4 11 nm core + 10 nm SiO_2 shell		**Cubic Fe_3O_4 18.5 nm core + 10 nm SiO_2 shell**		**Cubic Fe_3O_4 18.5 nm core + 2 nm SiO_2 shell**	
Sample	Fe_3O_4 concentration [mM]	Sample	Fe_3O_4 concentration [mM]	Sample	Fe_3O_4 concentration [mM]
2B1	0.7311	4B1	1.3352	TD4Y1	4.8897
2B2	0.3655	4B2	0.6676	TD4Y2	2.4449
2B3	0.1828	4B3	0.3338	TD4Y3	1.2224
2B4	0.0914	4B4	0.1669	TD4Y4	0.6112
2B5	0.0457	4B5	0.0835	TD4Y5	0.3056
2B6	0.0228	4B6	0.0413	TD4Y6	0.1528
2B7	0.0114	4B7	0.0209	TD4Y7	0.0764
2B8	0.0057	4B8	0.0104	TD4Y8	0.0382
				TD4Y9	0.0192
				TD4Y10	0.0097

3.1.3. Other materials

Fluorine Magnetic Resonance requires the use of standards with known fluorine content for the estimation of nanocarriers' absolute concentration. For that purpose, pure sodium fluoride (pure NaF, Chempur PL) and hexafluorobezene (99% C_6F_6 Sigma Aldrich PL) were purchased. Sodium fluoride powder was used for the preparation of solutions of different NaF concentrations in distilled water, and C_6F_6 was used without any further

processing. Additionally for experiments concerning Nafion™ based theranostic Nanocapsules detection, the Nafion™ perfluorinated resin solution (20 wt. % in mixture of lower aliphatic alcohols and water, 34% water) was purchased from Sigma Aldrich.

3.2. Experimental equipment and software

For all magnetic resonance spectroscopic/relaxation measurements as well as for imaging, the 9.4 T Bruker Biospec 94/20 research MRI scanner with 210mm bore diameter and the high-performance actively shielded gradient system with integrated shims was used. The strength of the gradient system was: 660 mT/m and 1T/m, depending on the gradient coil diameter.

For the experiments on nanocarriers containing standard (Fe_3O_4- and Gd-based) contrast agents, the birdcage coil, 35 mm in diameter, was used. Experiments with nanocapsules containing ^{19}F nuclei (Nafion™ and 5-fluorouracil) were carried out using a home-built small (ID of 14 mm) transmit-receive ribbon solenoid RF coil, which can be tuned either to ^{1}H or ^{19}F resonant frequency (i.e. 400.130 vs. 376.498 MHz). The geometry of that coil was adjusted to the analysed samples' size and shape to maximize the filling factor and thus SNR values. Also for comparison, the commercial Bruker $^{1}H/^{19}F$ volume coil with an inner diameter of 40 mm, designed as two geometrically decoupled linear resonators for ^{1}H and ^{19}F -nucleus frequencies, was used.

Paravision 5.1 and Topspin 2.0 software were used to accomplish MR imaging and spectroscopy. For processing and analysis of acquired spectra, relaxometry results, and images, OriginLab, ImageJ, ParaVision, and Matlab software were used.

3.3. Imaging sequences

3.3.1. MSME and RARE VTR

In the MSME (Multi-Slice-Multi-Echo) method, multiple spin echoes are generated using the CPMG sequence with slice-selective RF pulses. Each echo of the sequences generates a separate image with a different echo time. As a result, a series of images is

obtained which allows calculating T_2 time [116] [117] [118]. The timing diagram of the MSME sequence is presented in Figure 11 with:

A. Duration of read dephase that determines min. slice thickness and min. FOV in read direction;

B. Slice spoiler duration that removes residual FID signals of the refocusing pulses;

C. Phase encoding duration that determines minimum TE, minimum FOV in phase direction, and the amplitude of phase encoding;

D. Repetition spoiler duration that removes echoes of previous repetitions in experiments with short TR.

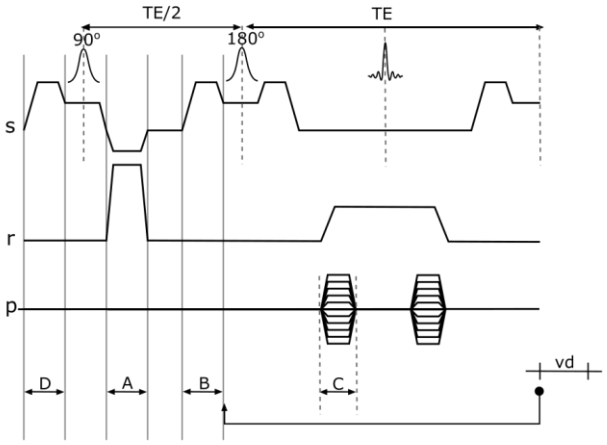

Figure 11 MESME sequence time diagram

For RARE VTR sequence principle and time diagram is the same but there's a possibility of multiple acquisitions with the repetition time (TR) varied for a saturation recovery series.

3.3.2. FLASH

FLASH (Fast Low Angle Shot) sequence uses a short repetition time (TR) and low flip angle (<< 90°) RF excitation pulses with subsequent reading gradient reversal to generate a gradient echo signal. The small flip angle pulses create an equilibrium of

longitudinal magnetization [119] [120]. The timing diagram of the FLASH sequence is presented in Figure 12 with:

A. Slice spoiler that removes incoherent components of the steady-state signal which could generate interference artifacts;

B. Duration of slice rephase that determines minimum TE, minimum slice thickness, and the amplitude of slice rephrasing;

C. Duration of read dephase that determines min. slice thickness and min. FOV in read direction;

D. Duration of read spoiler gradient that adds to the effect of the slice spoiler.

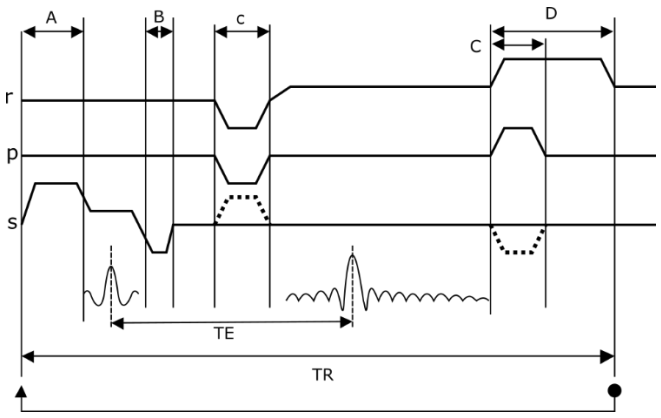

Figure 12 FLASH sequence time diagram

3.3.3. UTE 3D

The UTE 3D pulse sequence is the 3D implementation of the UTE (Ultrashort Echo Time) method with non-selective RF excitation that allows imaging with very short echo times. Here the sampling is performed already on a rising ramp of the gradient, so the data collection starts from the centre of the k-space and continues to the surface of a sphere (radial sampling trajectory). For the reconstruction of signals collected with such a trajectory, a data interpolation onto a cartesian grid is performed before the Fourier transformation. The only factors limiting minimum eco times are the duration of the RF pulse, and the time required to switch between excitation and acquisition mode (see time

diagram illustrated in Figure 13). Therefore, UTE 3D can be used for imaging samples with very short transverse relaxation times, even in the range of tens of microseconds.

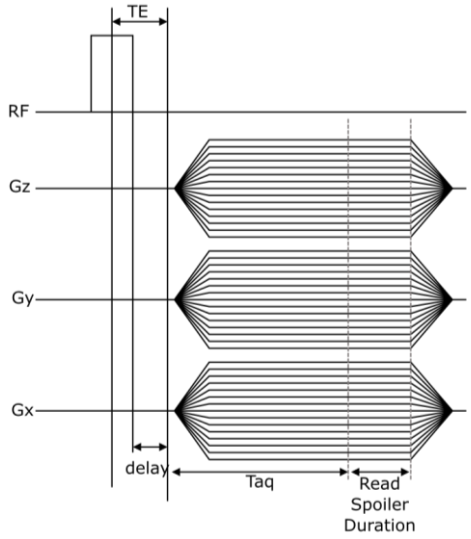

Figure 13 UTE 3D sequence time diagram

For the reconstruction based on regridding to Cartesian space, it is necessary to know the k-space trajectory. In a UTE 3D experiment, the trajectory can be measured per scan or on-demand. The latter option is especially useful when the trajectory cannot be measured due to a very low NMR signal (because of a very short T_2 relaxation time or low nuclei density). In such a situation, the trajectory should be measured using a homogenous phantom before investigations. As a measured trajectory is available only for given acquisition parameters such as FOV, slice thickness, size of acquisition matrix, and bandwidth, it has to be measured for each combination of those parameters that are planned to be used in the experiment.

The UTE 3D sequence was used for ^{19}F and ^{1}H imaging of samples containing Nafion™ polymer. For ^{19}F imaging, the NMR signal was too low to directly measure the trajectory per scan, therefore a spherical phantom filled with $CuSO_4$ solution (Figure 14) was used. The trajectory was measured with acquisition parameters planned to be used in the experiment. The images of the phantom with measured trajectories are presented in Figure 15 (each image was acquired with a different resolution described below the image).

Figure 14 Spherical $CuSO_4$ phantom for trajectory measurement

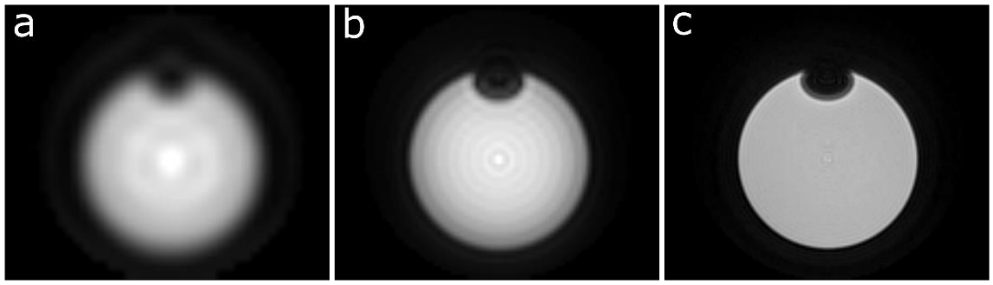

Figure 15 Trajectory measurement. UTE 3D ^{1}H Imaging of CuSO4 phantom. Imaging parameters: TE: 160 µs, TR: 8 ms, NA: 1, flip angle: 5˚, FOV: 40 mm isotropic, MTX: a) 32 x 32 x 32, b)64 x 64 x 64, c)128 x 128 x 128

If the trajectory measurement per scan is unavailable, another option is to use the theoretical trajectory. However, as the matrix size gets smaller, differences between ideal theoretical values and measured trajectory begin to be significant (Figure 16), therefore, images acquired with a theoretical trajectory suffer from severe reconstruction deviations.

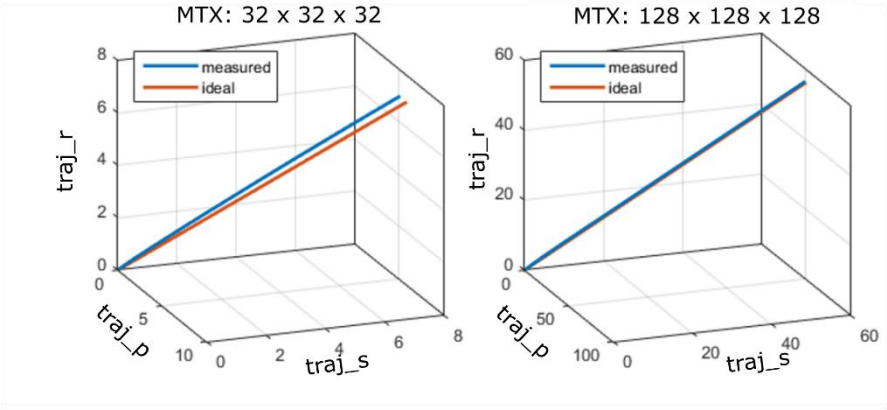

Figure 16 Measured vs. ideal (theoretical) trajectory for 3D UTE, where traj_r, traj_p, traj_s, are the measured k-space trajectory for the three orthogonal projection gradients

,

To test the influence of applied trajectory on the reconstruction of images with lower resolution (MTX = 32 isotropic), the images of the sample were acquired with the same parameters but with a theoretical or measured (using a spherical phantom) trajectory. Results presented in Figure 17 show clearly that imaging with a theoretical trajectory leads to incorrect image reconstruction with an altered size of the object and loss of some details.

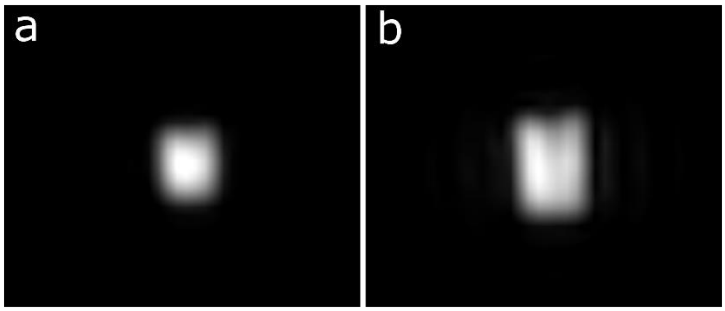

Figure 17 Comparison between images acquired with theoretical (a) and measured (b) trajectory. UTE 3D sequence, TE: 160 μs, TR: 8 ms, NA: 1, flip angle: 5°, FOV: 40 mm isotropic

Accurate image reconstruction is of utmost importance when there is a necessity for merging images obtained for different nuclei to determine the distribution of them in an anatomical (^{1}H-based) contest. As shown in Figure 18, imaging with a UTE 3D sequence with high resolution and trajectory measured per scan leads to the shape and size of the object being correctly reproduced in the ^{1}H image. Also, lower resolution ^{19}F imaging with a trajectory measured previously on the phantom allows locating ^{19}F nuclei in the correct position.

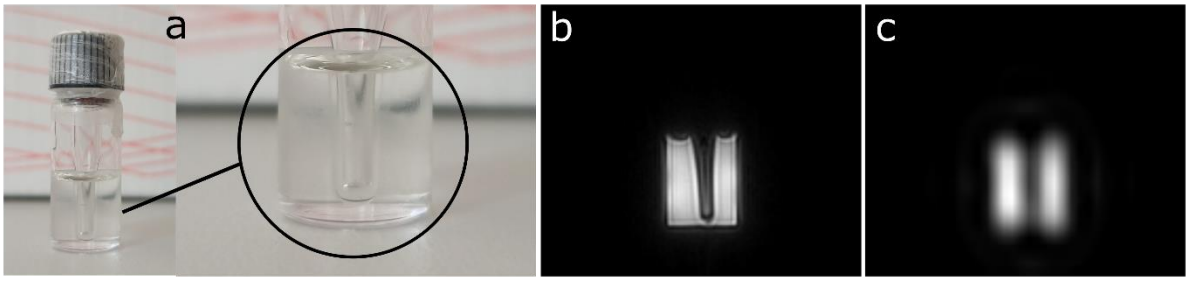

Figure 18 UTE 3D imging with measured trajectroy; a) Sample container with 20% Nafion ™ solution, b) high resolution ^{1}H UTE 3D image (resolution: 0.31 mm isotropic, NA: 1, total acq. Time: 6 min, 50s), c) lower resolution ^{19}F UTE 3D image (resolution: 1.25 mm isotropic, NA: 64, total acq. Time: 27 min 6 s)

3.4. The evaluation of contrasting properties of nanocarriers

3.4.1. Relaxation times and specific relaxivities measurement for nanocarriers with standard contrast agents

Contrasting properties of nanocarriers containing standard (Fe_3O_4 and Gd-based) contrast agents (CAs) were evaluated by analysis of image contrast alterations induced by T_1 or T_2 relaxation time changes in sites of their accumulation. The transverse (T_2) and longitudinal (T_1) relaxation times were determined from signal intensity changes in ROIs (regions of interest) in images acquired with different echo (TE) and repetition (TR) times. Values of TE and TR were chosen for each set of analysed samples to cover relaxation curves.

For T_1 measurements, RARE VTR images were used. In ParaVision 5.1 software, regions of interest were placed in the centre of each sample, and the average signal intensities for each repetition time were recovered. These values were later used for functions fitting of SI (signal Intensity) vs TR (Repetition Time). As the RARE VTR sequence generates saturation recovery series of images, the signal intensity evolution can be described by function 30:

$$I(t) = I_{max}\left(1 - e^{-TR/T_1}\right). \quad (30)$$

Signal intensity values obtained from images were plotted as TR dependence and function 30 was fitted (in OriginLab or Matlab software) to find the value of the T_1 parameter.

A similar procedure was applied to T_2 measurements. In this case, MSME images were used to obtain the average signal intensities in ROIs for each echo time, and the signal intensity vs TE dependence can be described by the function:

$$I(t) = I_0 e^{-TE/T_2}, \quad (31)$$

which was used to find T_2 values.

For acquired T_1 and T_2 values, linear regression of relaxation rates ($R_{1,2} = \frac{1}{T_{1,2}}$) vs contract agent (Gd or Fe_3O_4) concentration in samples was performed according to the equation:

$$R_{1/2} = R_{S1,S2} + r_{1,2} \cdot c, \qquad (32)$$

where: c - concentration of contrast agent (in mM), $R_{1,2}$ - the relaxation rate of a whole sample [s^{-1}], $R_{S1,S2}$- the relaxation rate of a solvent with nanocapsules without contrast agent [s^{-1}], $r_{1,2}$- the specific relaxivity of nanocarriers with contrast agents [$s^{-1}mM^{-1}$].

3.4.2. Relaxation times measurement and Signal to Noise Ration estimation for ^{19}F MRI

As there is no background signal in ^{19}F MRI, for fluorine-based contrast agents, the contrasting efficiency was evaluated by Signal to Noise Ratio (SNR) calculation. To achieve maximum SNR, it is crucial to set the sequence parameters to optimal values. For that reason, values of T_1 and T_2 have to be estimated.

The T_1 measurements for nanocarriers containing ^{19}F nuclei were performed in TopSpin 2.0 software using the Inversion Recovery (IR) method. T_2 relaxation times were estimated using the line width of peaks (under the assumption of a homogenous field). Full-Width Half Maximum (FWHM) values were measured directly on spectra. Considering the Lorentzian line shapes of spectral peaks and using:

$$FWHM = \frac{1}{\pi T_2} \qquad (33)$$

dependence, T_2 values were recovered.

Signal to noise ratio in MR images is defined as the ratio of the mean value of the signal intensity in the region of interest and the standard deviation of the noise:

$$SNR = \frac{S}{\sigma(N)}. \qquad (34)$$

The SNR was calculated as a quotient of the mean signal intensity in the area of interest and the standard deviation of signal intensity of the selected region surrounding

the object being investigated, or mean signal intensity measured with an entirely attenuated (150.00 dB) RF pulse.

Chapter 4

Experimental results

In this chapter, the results of experiments concentrating on magnetic resonance imaging, relaxometry, and spectroscopy are presented. The chapter is divided into 3 sections corresponding to each type of contrast agent used in synthesized nanocarriers. First results for nanocarriers containing Fe_3O_4 nanoparticles are presented, followed by results for nanocarriers with Gd, and finally results of imaging on fluorine nuclei.

4.1. Nanocarriers containing Fe_3O_4 nanoparticles

In this group, two types of nanocarriers were investigated: core-shell nanoparticles for MRI-guided chemo/NIR photothermal therapy (3.1.2, page 54) and magnetically responsive polycaprolactone nanocarriers (3.1.1.b, page 50). For each type of NCs first, the changes in T_1 and T_2 relaxation time values of a sample in the presence of different concentrations of nanocarriers were investigated. Next, contrast efficiency was assessed on MR images by contrast analysis.

4.1.1. Fe_3O_4@SiO_2 Core-shell nanoparticles

The first type of investigated core-shell nanocarriers were NPs with a spherical Fe_3O_4 core of 11 nm average size, coated by a 10 nm thick SiO_2 shell. For T_1 measurements, a RAREVTR sequence with the following parameters was used: slice thickness: 4 mm, FOV: 40 x 40 mm, MTX size: 128 x 128. The echo and repetition time values were adjusted to the analysed samples to fully sample relaxation curves. For higher NPs concentrations (samples 2B1 - 2B4) fifteen repetition (300, 350, 400, 450, 500, 750, 100, 1250, 1500, 2000, 3000, 4000, 6000, 8000, 10000 ms), and four echo (7.5, 22.5, 37.5, 52.5 ms) time values were used. For samples of lower NPs concentration (2B5 – 2B8) nineteen repetition (250, 500, 1000, 1250, 1500, 1750, 2000, 2250, 2500, 2750, 3000, 3500, 4000, 5000, 6000, 8000, 10000, 12500, 15000 ms), and four echo (30, 75, 120, 165 ms) time values were chosen.

For T_2 measurements, an MSME sequence with the following parameters was applied: slice thickness: 2.0 mm, FOV: 40 x 40 mm, MTX: 256 x 256, TR: 6000 ms. Again, TE values were adjusted to cover relaxation curves. For samples 2B1 – 2B4 sixteen (8, 16, 24, 32, …, 128 ms), while for samples 2B5-2B8 fifty (15, 30, 45, …, 750 ms) echo values were used.

The results of mean signal intensity measurements in regions of interest corresponding to each sample vs. TR and TE are presented in Figure 19.

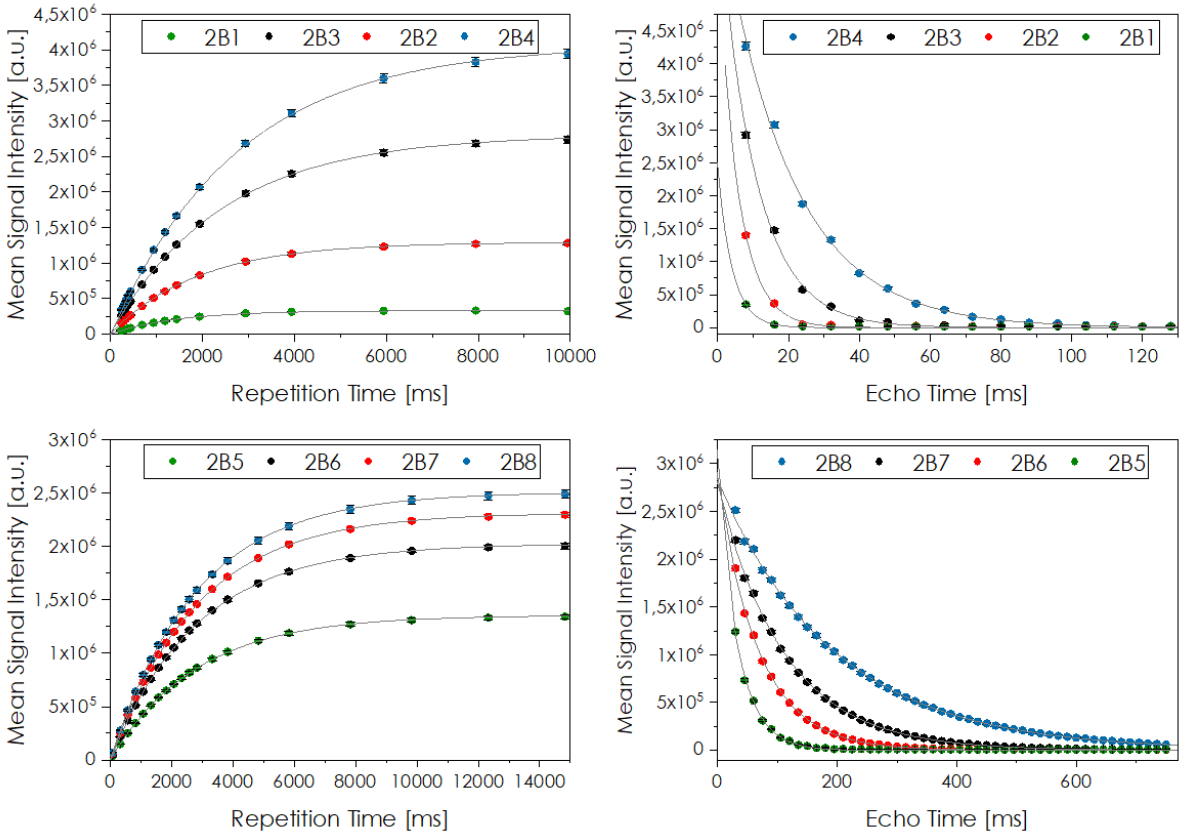

Figure 19 Mean signal intensities in regions of interest corresponding to 2B1 – 2B8 samples as the function of TR (left column) and TE (right column).

The obtained values of mean signal intensities were fitted with equations 30 and 31 in OriginLab software. All functions were fitted using the Levenberg–Marquardt iteration algorithm without weighting, with 1e-15 tolerance (reduced chi-square between two successive iterations). The adjusted R^2 for all functions was > 0.97, apart from the value obtained for T_2 relaxation curve fitting for sample 2B1, where due to very low signal,

the adj. R^2 was ~0.8. In Table 7 results of T_1 and T_2 measurements as well as calculated relaxation rates (R_1 and R_2) for 2B1 – 2B8 samples are presented.

Table 7 Magnetic resonance relaxometry results for 2B1 - 2B8 samples

Sample	Fe_3O_4 concentration [mM]	T_1 [ms]	R_1 [s^{-1}]	T_2 [ms]	R_2 [s^{-1}]
2B1	0.7311	1418.6 ± 10.9	0.7049 ± 0.0054	4.13 ± 0.94	242 ± 55.138
2B2	0.3655	1904.9 ± 6.8	0.5250 ± 0.0019	5.74 ± 0.42	174 ± 12.578
2B3	0.1828	2436.5 ± 13.9	0.4104 ± 0.0023	10.39 ± 0.33	96.2 ± 3.001
2B4	0.0914	2764.7 ± 13.9	0.3617 ± 0.0018	19.76 ± 0.28	50.60 ± 0.709
2B5	0.0457	2813.7 ± 20.8	0.3554 ± 0.0026	34.57 ± 0.78	28.93 ± 0.652
2B6	0.0228	2844.8 ± 16.8	0.3515 ± 0.0021	69.50 ± 0.66	14.39 ± 0.136
2B7	0.0114	2852.4 ± 14.2	0.3506 ± 0.0017	111.67 ± 0.51	8.955 ± 0.041
2B8	0.0057	2822.1 ± 10.0	0.3543 ± 0.0012	194.62 ± 0.61	5.138 ± 0.017

The dependences of relaxation rates R_1 and R_2 on nanocarriers concentration are presented in Figure 20 (NCs concentration is expressed by Fe_3O_4 concentration). Due to the superparamagnetic properties of Fe_3O_4, the effect of NPs on the relaxation rate is significantly higher for R_2 than for R_1. In a concentration range up to 0.1828 mM, a very good linear dependence of nanoparticles concentration on the R_2 relaxation rate (R_2 above 0.99) was observed. For higher concentrations, the effect of T_2 shortening was less pronounced, and measurement uncertainty was much higher due to very rapid signal decay (short relaxation time). Additionally, the clustering of NPs is expected to become more severe as their concentration in the solution increases. This effect of NPs clustering was observed in samples with the highest concentrations (Fe_3O_4 concentrations: 0.7311 and 0.3655 mM). For those reasons, the specific relaxivity r_2 was determined only for samples with lower concentrations ($\leq$ 0.1828 mM), as they are also more interesting for potential clinical application of the theranostic agents. The specific relaxivity r_2 obtained by linear regression (the slope of the linear function) was $r_2 = 511.7 \pm 8.9\ mM^{-1}s^{-1}$.

Conversely, the effect of T_1 shortening was practically not observed for low NPs concentrations up to 0.0457 mM, with T_1 values characteristic for distilled water, and in the higher concentration range, it was much weaker than observed for T_2. The linear regression result for R_1 relaxation rates was: $r_1=0.50 \pm 0.02\ mM^{-1}\ s^{-1}$, illustrating three

orders in magnitude differences between r_2 and r_1 relaxivities. To evaluate the behaviour of a contrast agent, two parameters are used: relaxivity (r_1 or r_2) and relaxivity ratio, i.e. transversal relaxivity (r_2)/longitudinal relaxivity (r_1). The value of r_1 or r_2 indicates the contrast enhancement potential of a contrast agent, while the r_2/r_1 ratio allows qualifying a contrast agent as positive (T_1) or negative (T_2). In general, positive contrast agents are characterized by lower r_2/r_1 ratio values (<5) while negative contrast agents have a larger r_2/r_1 ratio (>10). For investigated NCs the r_2/r_1 ratio was: 1023 ± 45.

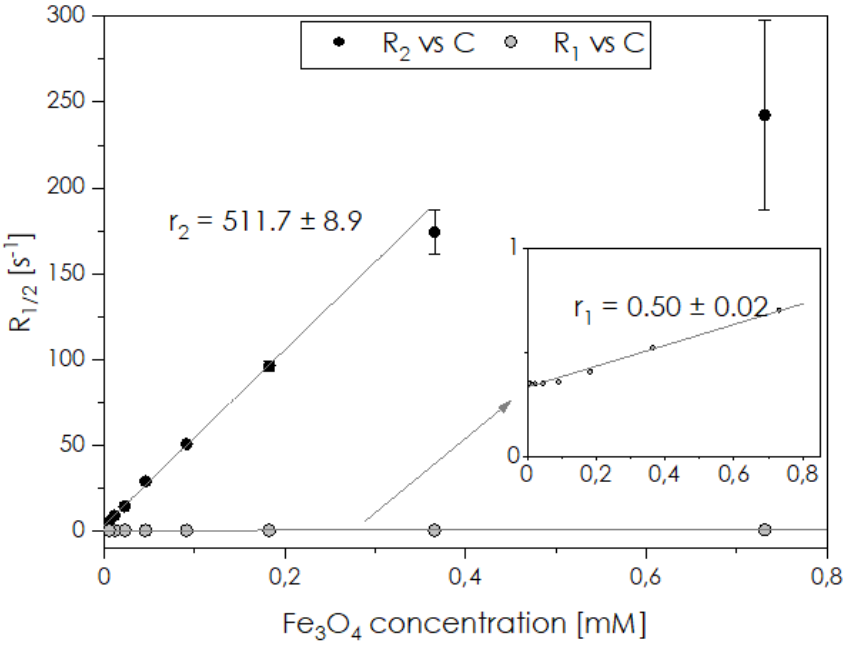

Figure 20 Dependence of relaxation rates on nanocarriers concentration for 2B1 - 2B8 samples

As investigated NCs strongly affect T_2 relaxation times, their contrasting properties were evaluated on T_2-weighted MR images. Figure 21 presents a series of axial MSME images (TR = 6000 ms, TE = 8 ms or 105 ms, FA: 180°, FOV: 40 × 40 mm, slice thickness: 2 mm) of aqueous solutions of Fe_3O_4@SiO_2 NPs of different concentrations (as marked in the figure). The MR images for high and low NPs concentration ranges are compared separately to illustrate the possibility of effective contrast in both cases. High concentrations, however, are much less probable to be achieved in vivo and require applying much shorter echo time to distinguish areas of different NCs concentrations.

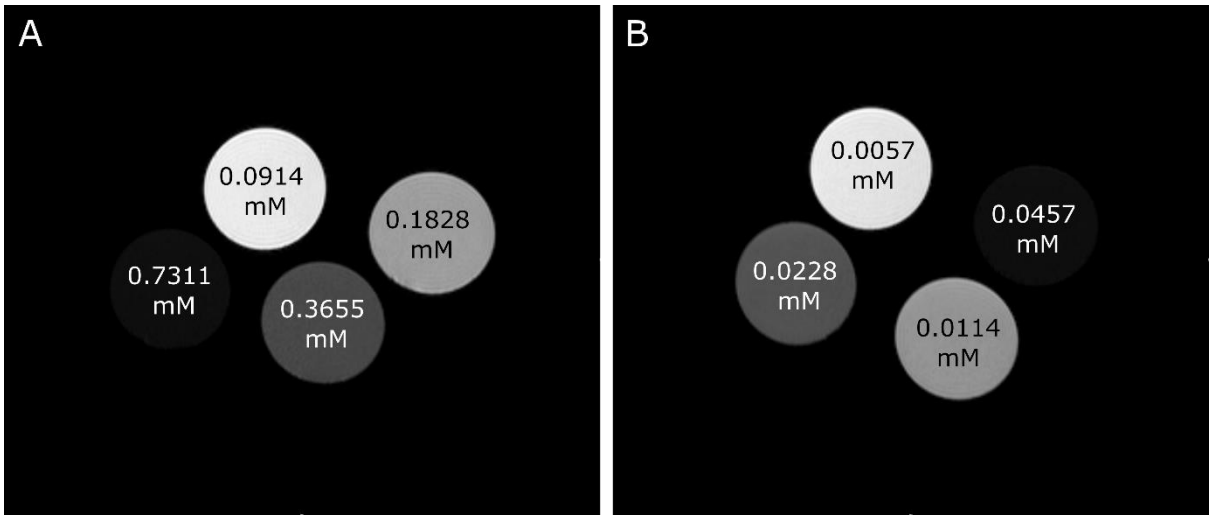

Figure 21 Axial images of samples 2B1 – 2B8 containing different concentrations of Fe_3O_4@SiO_2 nanoparticles. A) samples 2B1 - 2B8, B) samples 2B5 - 2B8. MSME sequence: TR: 6000 ms, FA: 180°, FOV: 40 × 40 mm, slice thickness: 2 mm; TE = 8 ms (A) and 105 ms (B). Concentrations of Fe_3O_4 as marked in images

To further visualize the "negative" contrasting properties of investigated NCs, images collected with different echo times are presented below (Figure 22). As the lower concentrations of NCs are more interesting from the point of view of potential applications, here only images of samples 2B5 – 2B8 are analysed. By increasing TE, stronger darkening of areas of higher NCs concentration and higher contrast between samples can be obtained.

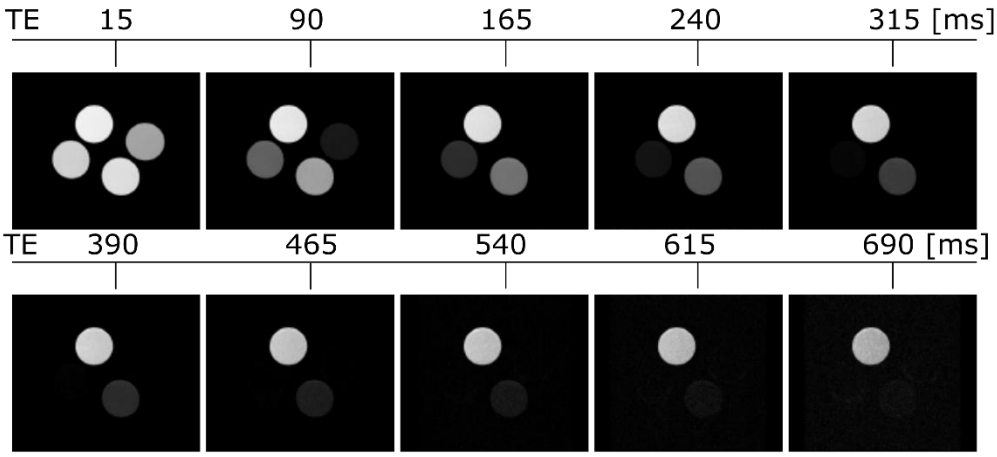

Figure 22 MR images of samples 2B5 – 2B8 collected with different echo times. Concentrations of Fe_3O_4 as in Figure 21 B. MSME sequence: TR: 6000 ms, FA: 180°, FOV: 40 × 40 mm, slice thickness: 2 mm, TE as marked above each image

To find the optimal imaging sequence parameters for contrast enhancement, the contrast was plotted as a function of the echo time. Contrast, or the signal difference between two regions of interest, can be determined as $C = \Delta S = S_{ref} - S_2$, where, $S_{ref,2}$ is the signal intensity in the region of the reference and the other region of interest. The contrast was evaluated for samples of the lower concentration range of contrast agent, so for samples: 2B5 – 2B8, as they are more probable to be achieved in vivo (Figure 23). Sample 2B8 (c = 0.0057 mM) was treated as a reference. Repetition time was 6000 ms and flip angle 180°. For each concentration, the optimal echo time can be found as the maximum of the curve: $TE_{opt\ (2B8/2B5)} = 60\ ms$, $TE_{opt\ (2B8/2B6)} = 120\ ms$, $TE_{opt\ (2B8/2B7)} = 135\ ms$.

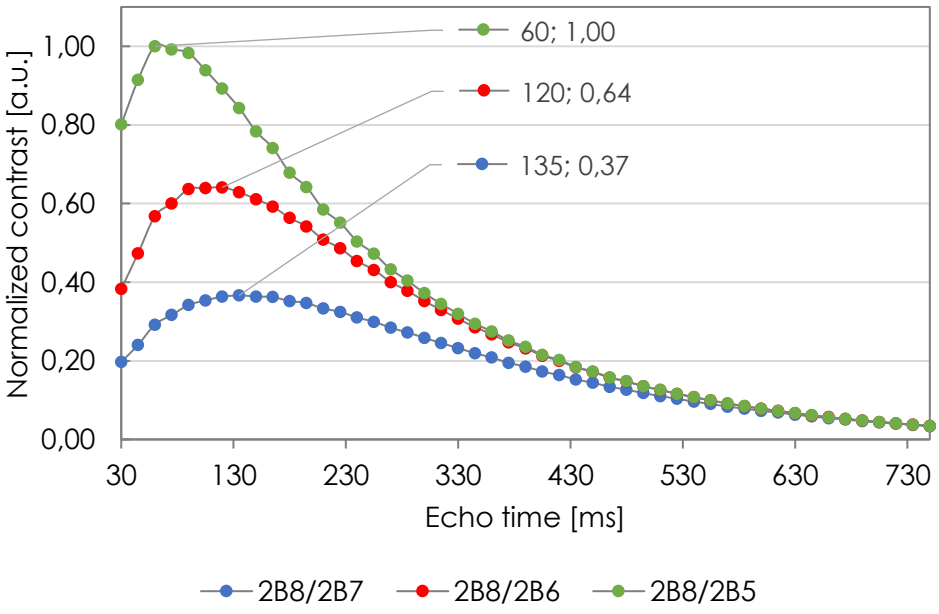

Figure 23 Contrast dependence on Echo Time for samples 2B5 - 2B8

The second type of investigated core-shell nanocarriers was NPs with a cubic Fe_3O_4 core of 18.5 nm average size, coated by a 10 nm thick SiO_2 shell.

To enable reliable comparison of contrasting properties for both types of core-shell nanocarriers with a 10 nm SiO_2 shell, the same parameters were used for 4B1 - 4B8 samples as for 2B1 - 2B8, i.e. T_1 was measured using RARE VTR sequence (slice: 4 mm, FOV: 40 x 40 mm, MTX: 128 x 128, fifteen TRs (300 – 10000 ms) and four TEs (7.5 – 52.5)

for 4B1 – 4B2 samples and nineteen TRs (250 - 15000 ms) and four TEs (30 - 165) for 4B5 – 4B8 samples) , and for T_2 measurements MSME sequence was applied (slice: 2.0 mm, FOV: 40 x 40 mm, MTX: 256 x 256, TR: 6000 ms, sixteen TEs (8 - 128 ms) for 4B1 – 4B4 samples and fifty TEs (15 - 750 ms) for 4B5 – 4B8 samples).

The results of mean signal intensity measurements in regions of interest corresponding to each sample vs. TR and TE are presented in Figure 24.

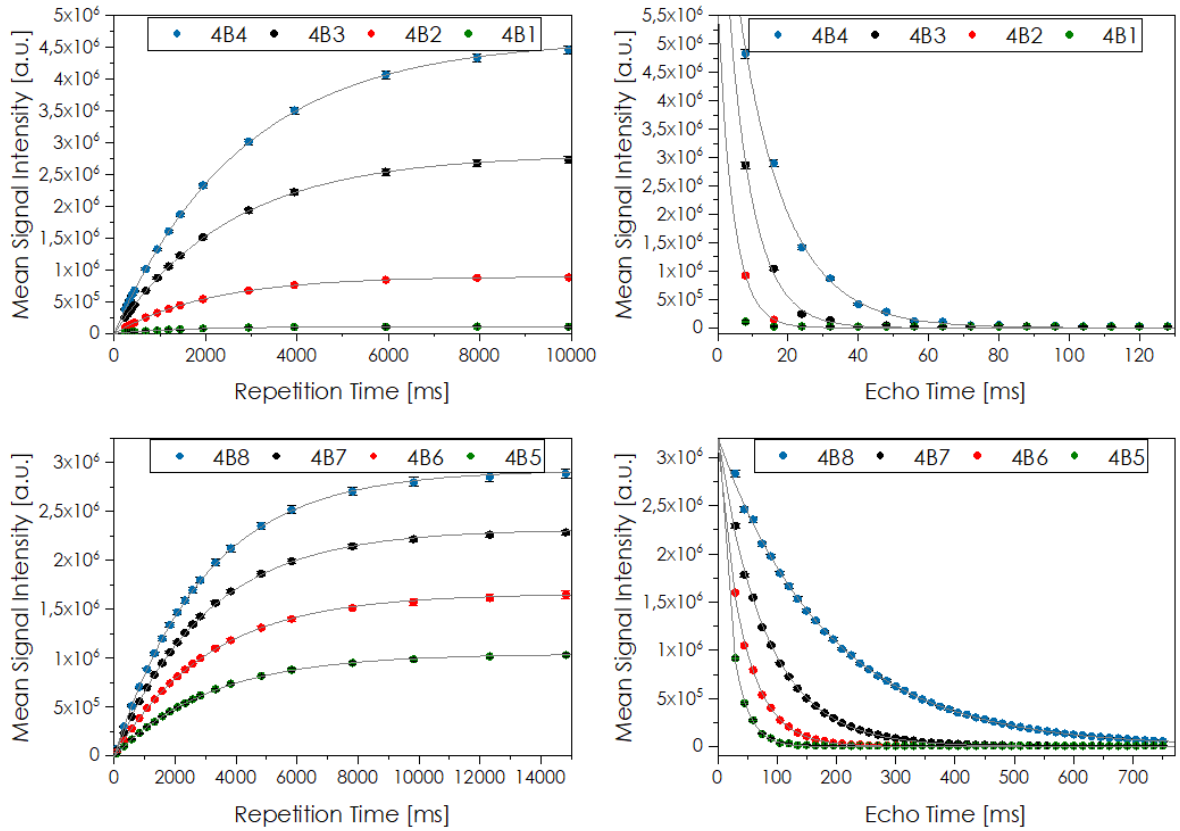

Figure 24 Mean signal intensities in regions of interest corresponding to 4B1 – 4B8 samples in the function of TR (left column) and TE (right column)

The obtained mean signal intensities for different TE and TR values were again fitted with functions 30 and 31 in OriginLab software. The adjusted R^2 for all functions was > 0.93. However, for the sample of the highest NCs concentration (4B1) due to raid transverse relaxation, the T_2 was not calculated, as the signal was at noise level for all TEs. Table 8 presents the results of T_1 and T_2 measurements as well as calculated relaxation rates (R_1 and R_2) for samples 4B1 – 4B8.

Table 8 Magnetic resonance relaxometry results for 4B1 - 4B8 samples

Sample	Fe_3O_4 concentration [mM]	T_1 [ms]	R_1 [s^{-1}]	T_2 [ms]	R_2 [s^{-1}]
4B1	1.3352	1604 ± 19	0.6236 ± 0.0074	-	-
4B2	0.6676	2122 ± 11	0.4711 ± 0.0024	4.40 ± 0.54	227.028 ± 27.570
4B3	0.3338	2549 ± 16	0.3923 ± 0.0022	7.21 ± 0.34	138.708 ± 6.363
4B4	0.1669	2809 ± 16	0.3560 ± 0.0020	13.53 ± 0.32	73.912 ± 1.718
4B5	0.0835	3202 ± 26	0.3123 ± 0.0025	24.40 ± 0.85	40.985 ± 1.426
4B6	0.0413	3090 ± 33	0.3236 ± 0.0034	44.19 ± 0.65	22.630 ± 0.330
4B7	0.0209	2996 ± 25	0.3338 ± 0.0028	81.68 ± 0.56	12.243 ± 0.083
4B8	0.0104	2985 ± 19	0.3350 ± 0.0020	184.31 ± 0.49	5.426 ± 0.015

The dependences of relaxation rates R_1 and R_2 on nanocarriers concentration for samples 4B1 – 4B8 are presented in Figure 25. As expected, the effect of NPs on the relaxation rate is significantly higher for R_2 than for R_1. In the low concentration range (up to 0.1669 mM Fe_3O_4) the T_1 contrasting effect was not observed. Only for higher concentrations, very weak T_1 shortening can be achieved with relaxivity $r_1 = 0.228 \pm 0{,}010$ $mM^{-1}s^{-1}$.

Similarly to 2B1 – 2B8 samples, the effect of T_2 shortening was much more obvious. This was manifested in a very high relaxivity r_2 value. In a concentration range of up to 0.3338 mM Fe_3O_4, very good linearity of nanoparticles concentration on the R_2 dependence was preserved (R^2 above 0.99) with relaxivity: $r_2 = 406.4 \pm 9.0$ $mM^{-1}s^{-1}$. For higher concentrations, the effect of T_2 shortening starts to weaken and is subjected to high measurement uncertainty. Additionally, as only low concentrations of contracting agents are clinically applicable, the specific relaxivity r_2 was determined using results obtained for samples with concentrations ≤ 0.3338 mM Fe_3O_4. For investigated 4B1 – 4B8 NCs, the r_2/r_1 ratio was: 1782 ± 88, therefore they can be classified as strong negative contrast agents.

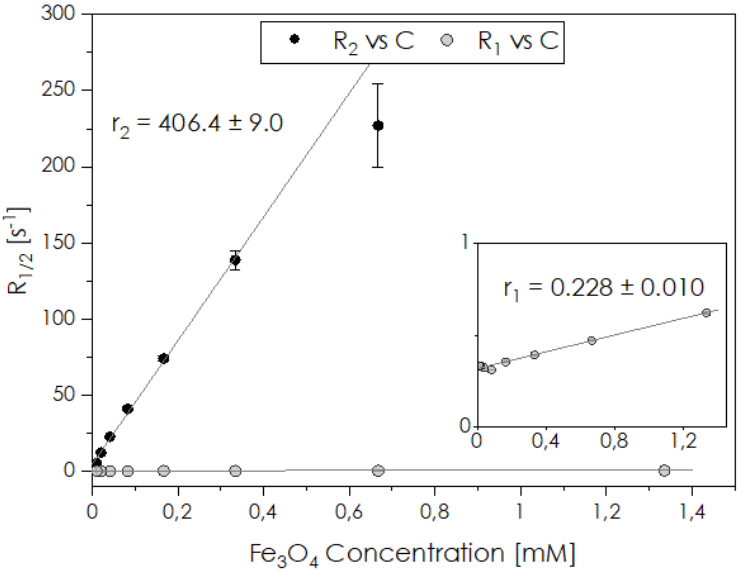

Figure 25 Dependence of relaxation rates on nanocarriers concentration for 4B1 - 4B8 samples

Similarly to previously described results, contrasting properties of 4B1 – 4B8 samples were evaluated on T_2-weighted MR images. In Figure 26, a series of axial MSME images (TR = 6000 ms, TE = 8 ms or 105 ms, FA: 180°, FOV: 40 × 40 mm, slice thickness: 2 mm) of aqueous solutions of different NCs concentrations (as marked in the figure) is presented.

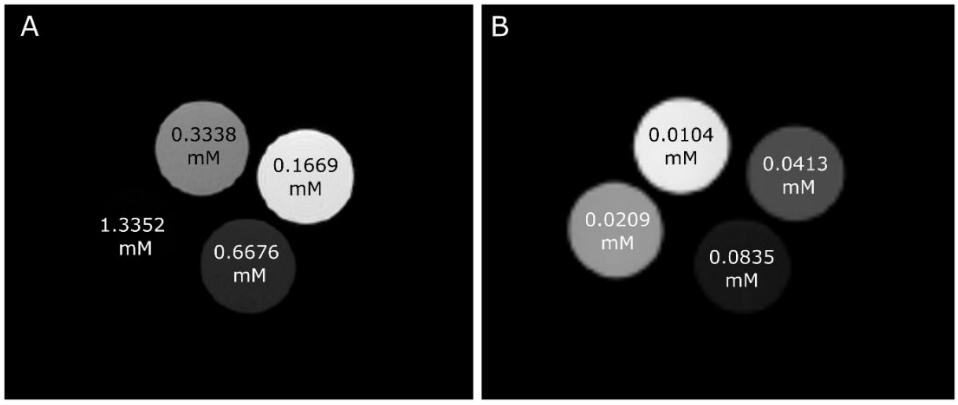

Figure 26 Axial images of samples 4B1 – 4B8 containing different concentrations of Fe_3O_4@SiO_2 nanoparticles. MSME sequence: TR: 6000 ms, FA: 180°, FOV: 40 × 40 mm, slice thickness: 2 mm; TE = 8 ms (A) and 45 ms (B). Concentrations of Fe_3O_4 as marked in images

The negative contrasting properties of investigated NCs were visualized by a collection of images with different echo times (Figure 27). For long repetition and echo times (T_2-weighting), very strong suppression of MR signal in samples with a higher concentration of NCs was observed, confirming their negative contrasting effect.

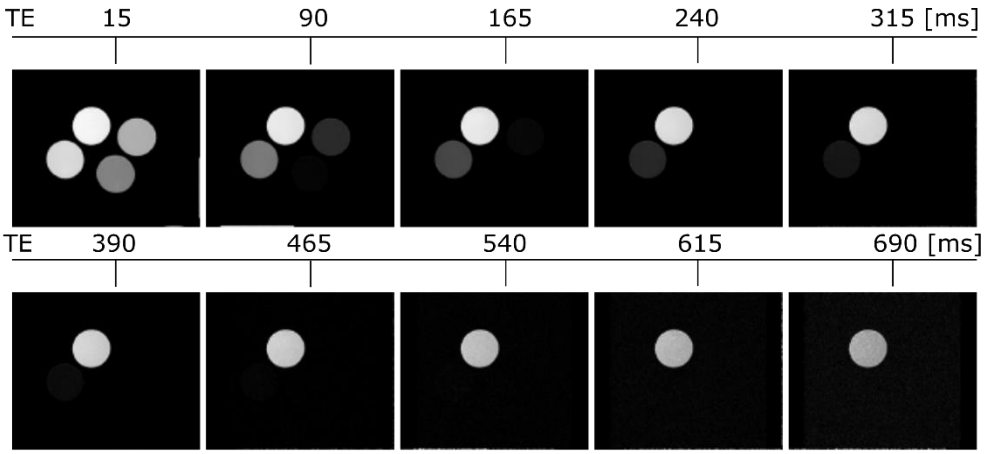

Figure 27 MR images of samples 4B5 – 4B8 collected with different echo times. Concentrations of Fe_3O_4 as in Figure 26 B. MSME sequence: TR: 6000 ms, FA: 180°, FOV: 40 × 40 mm, slice thickness: 2 mm, TE as marked above each image

To find the optimal imaging sequence parameters for contrast enhancement, the contrast was evaluated for samples of the lower concentration range of contrast agent, so for samples: 4B5 – 4B8 (Figure 28). Sample 4B8 (c = 0.0104 mM) was treated as reference. Repetition time was 6000 ms, and the flip angle was 180°. For each concentration, the optimal echo time can be found as the maximum of the curve: $TE_{opt\ (4B8/4B5)} = 60\ ms$, $TE_{opt\ (4B8/4B6)} = 90\ ms, TE_{opt\ (4B8/4B7)} = 120\ ms$.

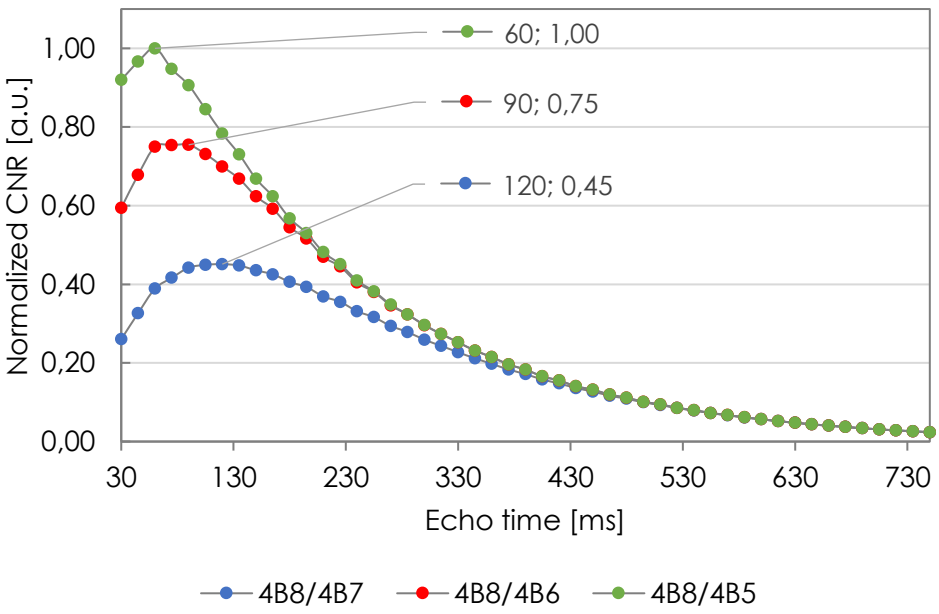

Figure 28 Contrast dependence on Echo Time for samples 4B5 - 4B8

The last type of investigated core-shell nanocarriers was NPs with a cubic Fe_3O_4 core of 18.5 nm average size, coated by a 2 nm thick SiO_2 shell. Here, ten investigated samples were divided into three groups to adjust echo and repetition time values to sample T_1 and T_2 relaxation curves. T_1 was measured using RARE VTR sequence (slice: 4 mm, FOV: 40 x 40 mm, MTX: 128 x 128) with twelve TRs (250, 500, 750, 1000, 1500, 2000, 2500, 5000, 7500, 10000, 15000, 20000 ms) and eight TEs (16, 40, 64, 88, 112, 136, 160, 184 ms) for samples of the highest NCs concentrations (TD4Y1 – TD4Y2), and with twelve TRs (250, 500, 750, 1000, 1500, 2000, 2500, 5000, 7500, 10000, 15000, 20000 ms) and eight TEs (20, 50, 80, 110, 140, 170, 200, 230 ms) for TD4Y3- TD4Y6 and TD4Y7- TD4Y10 samples.

For T_2 measurements, a MSME sequence was applied (slice: 2.0 mm, FOV: 40 x 40 mm, MTX: 256 x 256, TR: 6000 ms) with fifty TEs (8, 16, 24, … , 400 ms) for TD4Y1 – TD4Y2 samples, fifty TEs (10, 20, 30, … , 500 ms) for TD4Y3- TD4Y6 and fifty TEs (50, 100, 150, … , 2500 ms) for TD4Y7- TD4Y10 samples. The results of mean signal intensity measurements in regions of interest corresponding to each sample vs. repetition and echo time values are presented in Figure 29. As before, equations 30 and 31 were fitted to mean signal intensities vs TE and TR values in OriginLab software. The adjusted R^2 for all fitted functions was > 0.98. The results of T_1 and T_2 measurements as well as calculated relaxation rates (R_1 and R_2) for samples TD4Y1 – TD4Y10 are presented below (Table 9).

Table 9 Magnetic resonance relaxametry results for TD4Y1 – TD4Y10 samples

Sample	Fe_3O_4 concentration [mM]	T_1 [ms]	R_1 [s^{-1}]	T_2 [ms]	R_2 [s^{-1}]
TD4Y1	4.8897	2446.8 ± 9.0	0.4087 ± 0.0015	5.14 ± 0.53	194.4803 ± 19.8606
TD4Y2	2.4449	2681.2 ± 10.0	0,3730 ± 0.0014	9.12 ± 0.34	109.6293 ± 4.0237
TD4Y3	1.2224	2822.0 ± 24.4	0.3544 ± 0.0031	17.26 ± 0.71	57.9497 ± 2.3775
TD4Y4	0.6112	2833,6 ± 34.1	0.3529 ± 0.0043	31.42 ± 0.45	31.8259 ± 0.4528
TD4Y5	0.3056	2841.9 ± 35.4	0.3519 ± 0.0044	54.53 ± 0.33	18.3394 ± 0.1108
TD4Y6	0.1528	2828,7 ± 26.9	0.3535 ± 0.0034	100.07 ± 0.23	9,9935 ± 0.0229
TD4Y7	0.0764	2759,3 ± 20.4	0.3624 ± 0.0027	148.97 ± 3.54	6.7128 ± 0.1594
TD4Y8	0.0382	2727.3 ± 10.8	0.3667 ± 0.0015	205.77 ± 2.47	4.8599 ± 0.0582
TD4Y9	0.0192	2760.3 ± 14.8	0.3623 ± 0.0020	246.50 ± 2.33	4.0568 ± 0.0383
TD4Y10	0.0097	2764.1 ± 16.5	0.3618 ± 0.0022	409.75 ± 1.44	2.4405 ± 0.0086

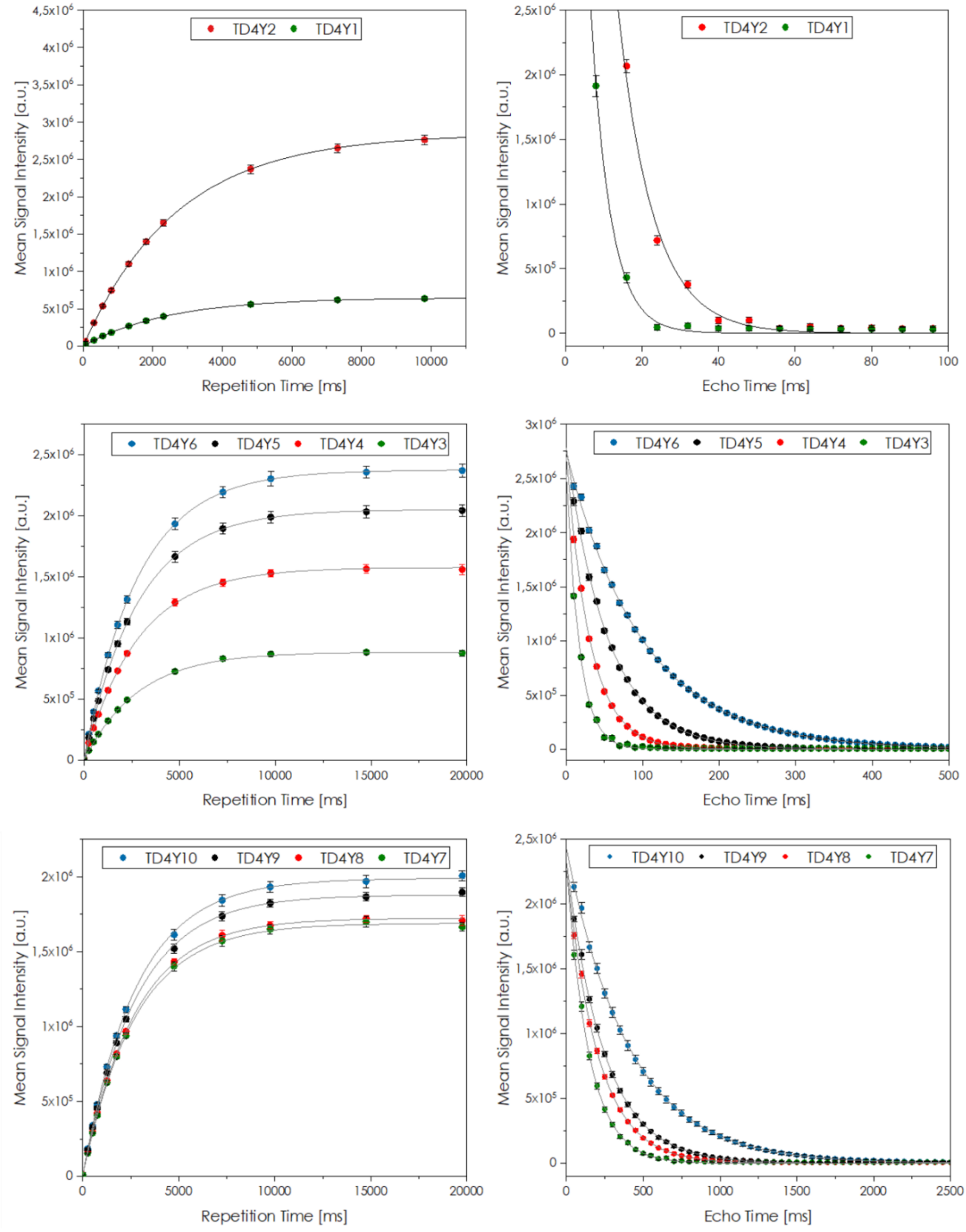

Figure 29 Mean signal intensities in regions of interest corresponding to TD4Y1 – TD4Y10 samples in the function of TR (left column) and TE (right column)

Calculated R_1 and R_2 relaxation rates values for samples TD4Y1 – TD4Y10 are presented in the function of NCs concentration (expressed as the concentration of Fe_3O_4) in Figure 30. The T_1 contrasting effect was not observed in the low concentration range (up to approximately 0.3056 mM Fe_3O_4) and for higher concentrations, the T_1 shortening induced by investigated NCs was very weak, with a specific relaxivity $r_1 = 0.0131 \pm 0.0010$ $mM^{-1}s^{-1}$.

As expected, the effect of T_2 shortening is significantly higher. Similarly to previous results, the influence of increasing NCs concentration on R_2 changes was much more pronounced. In the entire concentration range, very good linearity of nanoparticles concentration on the R_2 dependence was observed (adj. R^2 above 0.99) with however much lower (at least one order of magnitude) relaxivity: $r_2 = 39.72 \pm 0.83$ $mM^{-1}s^{-1}$ than for previously described samples. For investigated TD4Y1 – TD4 Y10 NCs, the r_2/r_1 ratio was: 3030 ± 240.

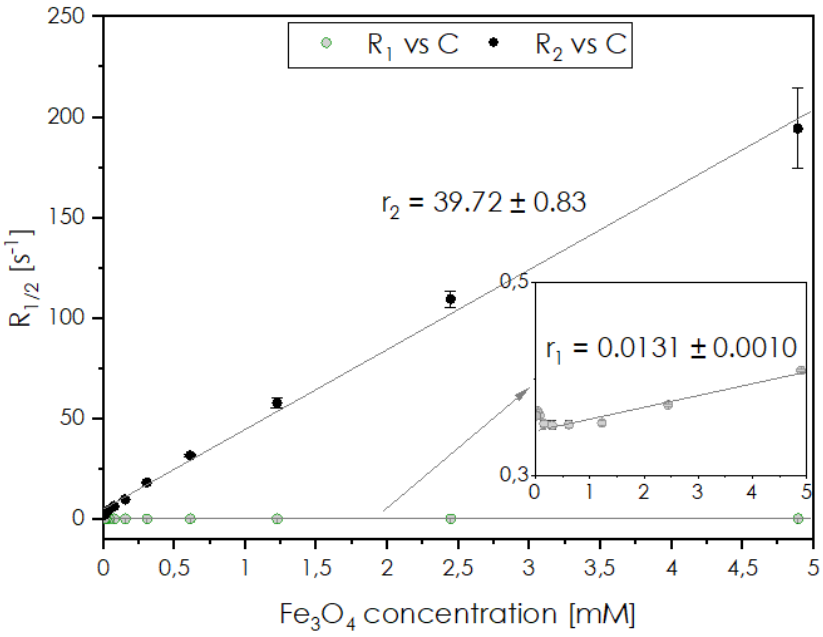

Figure 30 Dependence of relaxation rates on nanocarriers concentration for TD4Y1 – TD4Y10 samples

Signal intensity changes in MR images induced by investigated NCs in regions of their accumulation were assessed. In Figure 31, a series of axial MSME images (TR = 6000 ms, TE = 8 ms, 30 ms, or 300 ms, FA: 180°, FOV: 40 × 40 mm, slice thickness: 2 mm) of aqueous solutions of different NCs concentrations is presented. For each concentration range (A: 4.8897 – 2.449 mM, B: 1.2224 – 0.1528 mM, C:0.0764 – 0.0097 mM) it is possible

to distinguish regions of different NCs accumulation. Therefore, effective contrasting can be achieved even for smaller concentrations of analysed NCs. This was also confirmed by a collection of images for samples TDY7 – TDY10 with different echo times (Figure 32), where for long repetition and echo time (T_2-weighted image), very strong darkening in areas corresponding to higher NCs concentrations was observed.

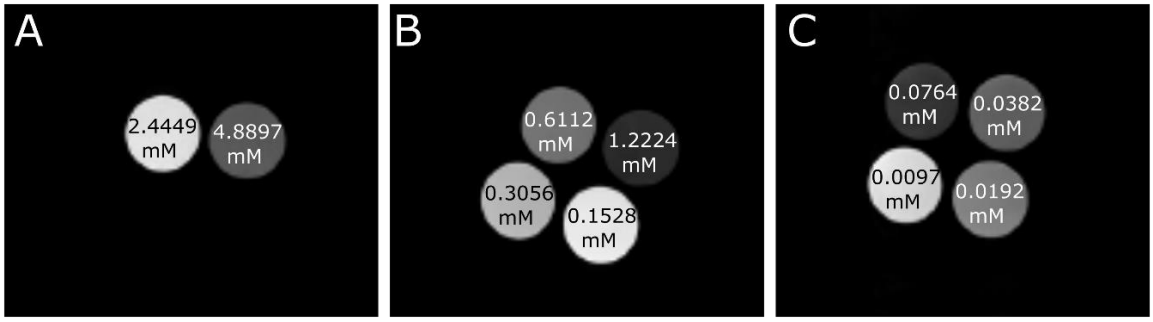

Figure 31 Axial images of samples TD4Y1 – TD4Y10 containing different concentrations of Fe_3O_4@SiO_2 nanoparticles. MSME sequence: TR: 6000 ms, FA: 180°, FOV: 40 × 40 mm, slice thickness: 2 mm; TE = 8 ms (A), 30 ms (B) and 300 ms (C). Concentrations of Fe_3O_4 as marked

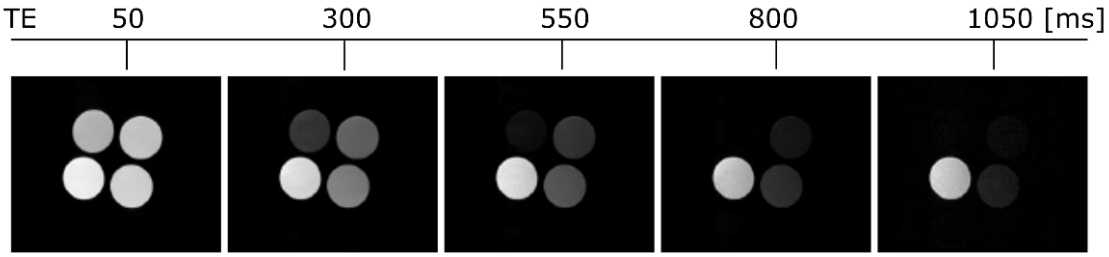

Figure 32 MR images of samples TD4Y7 – TD4Y10 collected with different echo times. Concentrations of Fe_3O_4 as in Figure 31 C. MSME sequence: TR: 6000 ms, FA: 180°, FOV: 40 × 40 mm, slice thickness: 2 mm, TE as marked above each image

The contrast was evaluated for samples of the lower concentration range of contrast agent, so for samples: TD4Y7 – TD4Y10. Sample TD4Y10 (c = 0.0104 mM) was treated as a reference. Repetition time was 6000 ms and a flip angle 180°. For each concentration, the optimal echo time can be found as the maximum of the curve: $TE_{opt\ (TD4Y10/TD4Y7)} = 200\ ms$, $TE_{opt\ (TD4Y10/TD4Y8)} = 250\ ms$, $TE_{opt\ (TD4Y10/TD4Y9)} = 300\ ms$ (Figure 33).

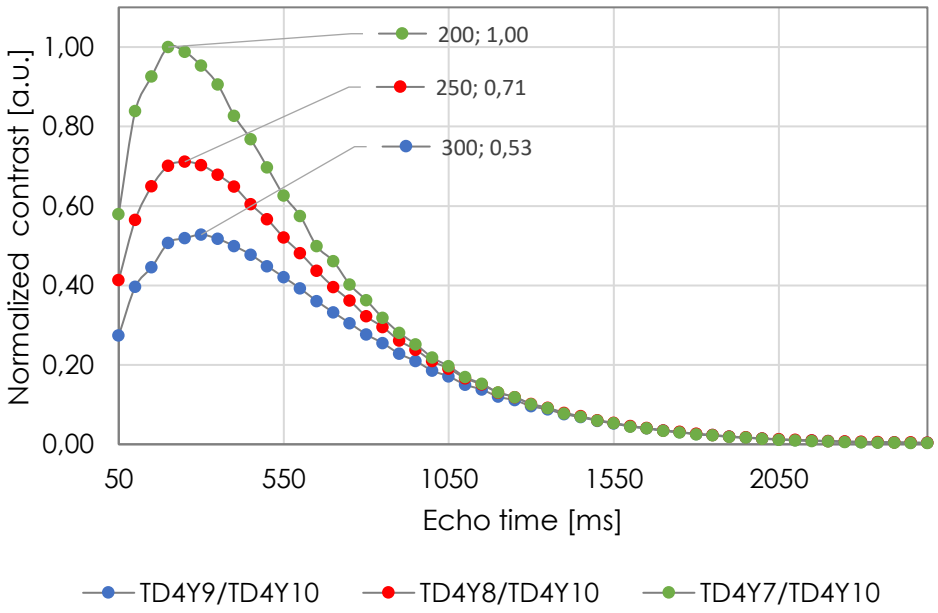

Figure 33 Contrast dependence on Echo Time for samples TD4Y7 - TD4Y10

4.1.2. Magnetically responsive polycaprolactone nanocarriers

In this group, two types of NCs with different shell compositions were investigated. For both types, four sets of agarose gel phantoms with varied NCs concentrations were prepared: two sets with higher concentrations (0.232 - 1.857 mM for NCs of the first type or 0.248 - 1.986 mM Fe_3O_4 for NCs of the second type) and two sets with lower concentrations of NCs. (0.015 - 0.232 mM for NCs of first type or 0.016 - 0.248mM Fe_3O_4 for NCs of second type) .

Both types of NCs were investigated using the same parameters to reliably compare the obtained results. Mean signal intensity values for different echo and repetition times were acquired simultaneously using the RARE VTR sequence with the following parameters: slice thickness: 4 mm, FOV: 40 x 40 mm, MTX size: 64 x 64. six TR values (5472, 2972, 1472, 772, 372, 172 ms) and eight TE values (3.7, 7.4, 11.1, 14.8, 18.5, 22.2, 25.9, 29.6 ms).

For samples with the highest concentration of NCs of both types (1.856 mM - MR NC 0 or 1.986 mM Fe_3O_4 - MR NCx 0), very rapid transverse relaxation was observed, resulting in signal intensity at the level of background noise even for the shortest (3.7 ms)

applied echo time. For that reason, T_2 relaxation time was not calculated for those samples. For all other samples, the initial calculation of the mean signal intensities in the regions of interest for all repetition or echo times was performed in Paravision 5.1, while further analysis (T_1 and T_2 fitting) was carried out in OriginLab.

The results of mean signal intensity measurements in regions of interest corresponding to each sample vs. TR and TE are presented in Figure 34 and Figure 35 (mean signal intensity vs. TR) and Figure 36 and Figure 37 (mean signal intensity vs. TE).

T_1 and T_2 values were determined via single exponential curve fitting (equations 30 and 31) in OriginLab software. The adjusted R_2 for all fitted functions was > 0.97. The final T_1 and T_2 relaxation times were calculated as an average of results obtained for samples with the same concentration from both series. Results of relaxation times T1 and T_2, as well as calculated relaxation rates (R_1 and R_2) for samples MR NC 2 – MR NC 128, are presented in Table 10, while corresponding results for MR NCx 2 – MR NCx 128 can be found in Table 11.

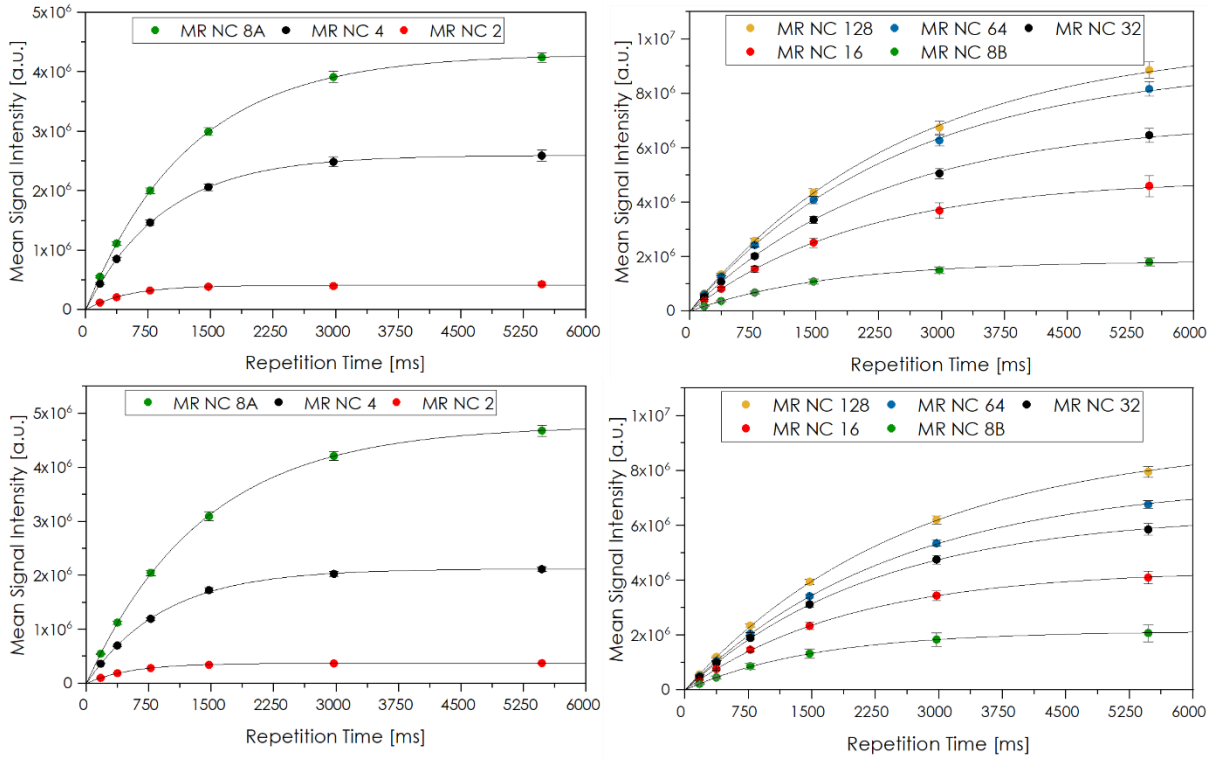

Figure 34 Mean signal intensities in regions of interest corresponding to MR NC 2 – MR NC 128 samples in the function of TR for series 1 (first row), and series 2 (second row)

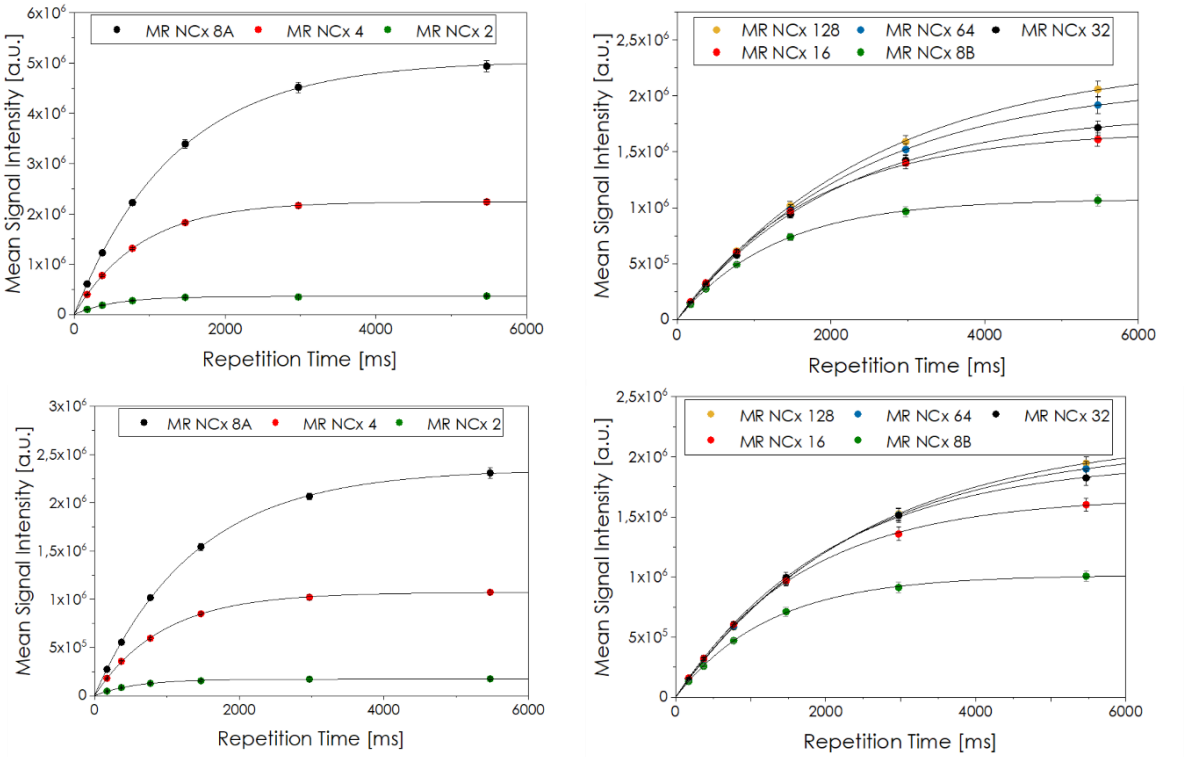

Figure 35 Mean signal intensities in regions of interest corresponding to MR NCx 2 – MR NCx 128 samples in the function of TR for series 1 (first row), and series 2 (second row)

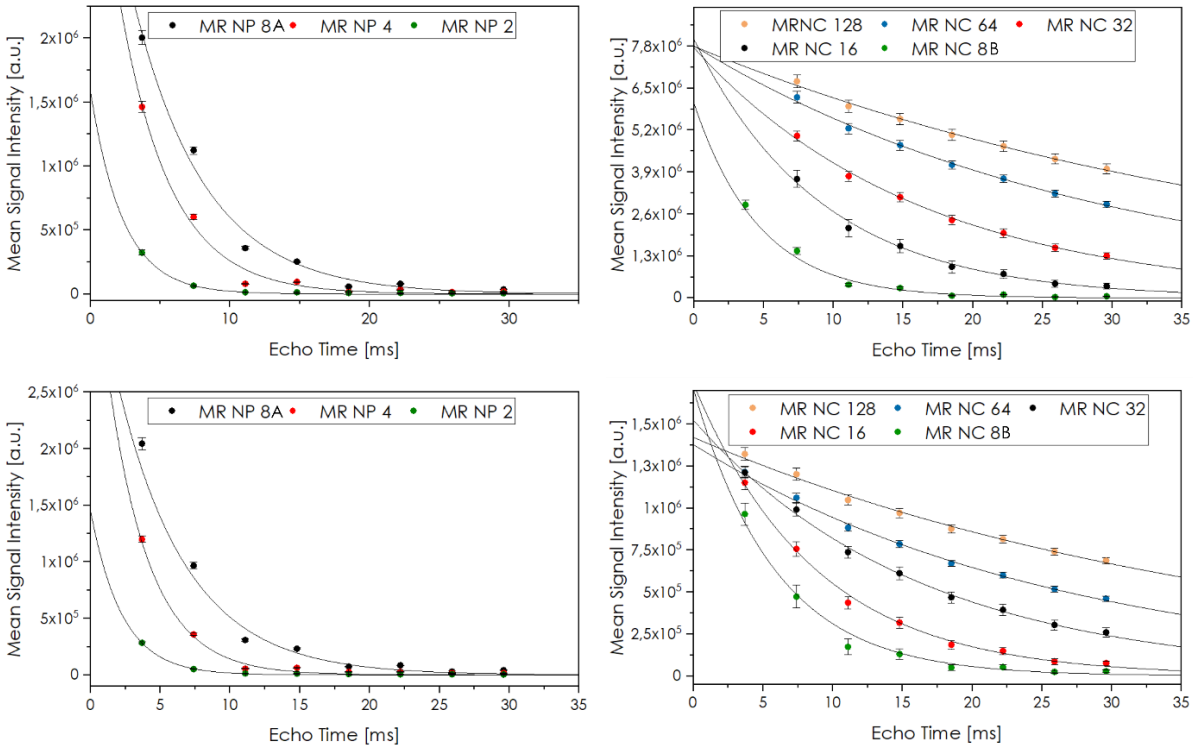

Figure 36 Mean signal intensities in regions of interest corresponding to MR NC 2 – MR NC 128 samples in the function of TE for series 1 (first row), and series 2 (second row)

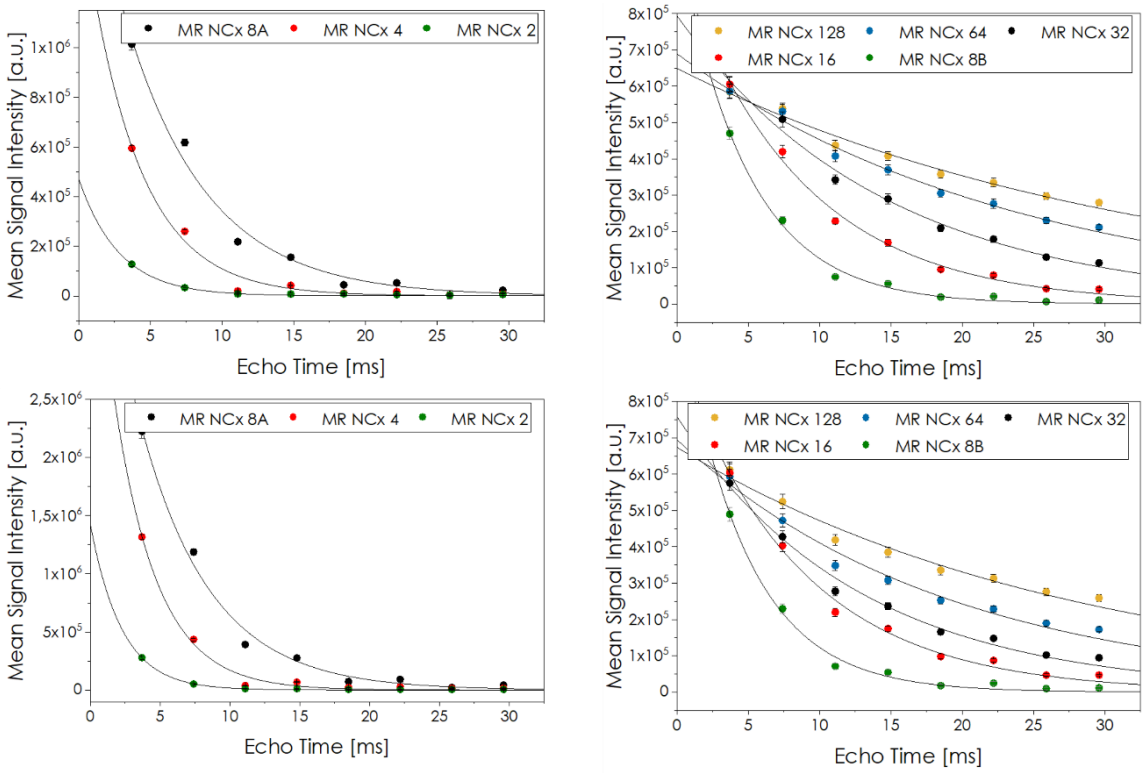

Figure 37 Mean signal intensities in regions of interest corresponding to MR NCx 2 – MR NCx 128 samples in the function of TE for series 1 (first row), and series 2 (second row).

Table 10 Magnetic resonance relaxametry results for MR NC 2 – MR NC 128 samples

Sample	Fe_3O_4 concentration [mM]	T_1 [ms]	R_1 [s^{-1}]	T_2 [ms]	R_2 [s^{-1}]
MR NC 128	0.015	2606.7 ± 43.4	0.3837 ± 0.0064	41.66 ± 1.34	24.06 ± 0.77
MR NC 64	0.029	2489.0 ± 32.6	0.4018 ± 0.0053	27.95 ± 0.69	35.89 ± 0.88
MR NC 32	0.058	2246.7 ± 31.0	0.4451 ± 0.0062	16.17 ± 0.42	61.84 ± 1.59
MR NC 16	0.116	1975.6 ± 30.6	0.5065 ± 0.0079	8.91 ± 0.35	112.36 ± 4.34
MR NC 8 B	0.232	1603.5 ± 30.4	0.6248 ± 0.0118	5.27 ± 0.46	192.24 ± 17.23
MR NC 8 A	0.232	1316.8 ± 9.2	0.7622 ± 0.0051	5.06 ± 0.45	197.69 ± 17.68
MR NC 4	0.464	927.2 ± 7.6	1.0786 ± 0.0090	3.31 ± 0.35	305.53 ± 34.67
MR NC 2	0.929	515.9 ± 12.5	1.9407 ± 0.0486	2.30 ± 0.17	435.83 ± 31.50
MR NC 0	1.857	-	-	-	-

Table 11 Magnetic resonance relaxametry results for MR NCx 2 – MR NCx 128 samples

Sample	Fe_3O_4 concentration [mM]	T_1 [ms]	R_1 [s^{-1}]	T_2 [ms]	R_2 [s^{-1}]
MR NCx 128	0.016	2523.8± 25.0	0.3962 ± 0.0040	41.66 ± 1.34	32.77 ± 2.06
MR NCx 64	0.031	2354.4 ± 15.8	0.4247 ± 0.0029	27.95 ± 0.69	46.71 ± 2.63
MR NCx 32	0.062	2066.3 ± 26.2	0.4840 ± 0.0062	16.17 ± 0.42	73.80 ± 3.79
MR NCx 16	0.124	1716.6 ± 24.7	0.5825 ± 0.0084	8.91 ± 0.35	117.72 ± 5.69
MR NCx 8 B	0.248	1260.1 ± 17.2	0.7936 ± 0.0108	5.27 ± 0.46	214.82 ± 12.93
MR NCx 8 A	0.248	1354.5 ± 10.3	0.7383 ± 0.0057	5.06 ± 0.45	186.39 ± 13.55
MR NCx 4	0.497	909.3 ± 6.9	1.0997 ± 0.0083	3.31 ± 0.35	295.42 ± 28.81
MR NCx 2	0.993	547.8 ± 17.0	1.8254 ± 0.0567	2.30 ± 0.17	392.93 ± 33.20
MR NCx 0	1.986	-	-	-	-

The dependences of relaxation rates R_1 and R_2 on nanocarriers concentration for samples MR NC 2 – MR NC 128 are presented below (Figure 38), while corresponding results for samples MR NCx 2 – MR NCx 128 can be found in Figure 39 (NCs concentration is expressed by Fe_3O_4 concentration). Despite the incorporation of Fe_3O_4 in the layered structure of polyelectrolytes, strong superparamagnetic properties were preserved, resulting in a very effective shortening of T_2 relaxation time. In a concentration range up to 0.232 mM for MR NC samples and up to 0.248 mM for MR NCx samples, a very good linear dependence of nanoparticles concentration on the R_2 relaxation rate (adj. R^2 above 0.99) was observed. As mentioned before, due to very rapid signal decay for high NCs concentrations, the uncertainty of T_2 results is much higher. The specific relaxivity r_2 obtained by linear regression for obtained T_2 values (in the range where the linear relationship was observed) was $r_2 = 788 \pm 25$ $mM^{-1}s^{-1}$ for MR NC samples and $r_2 = 710 \pm 23$ $mM^{-1}s^{-1}$ for MR NCx samples.

The relationship between NCs concentration and relaxation rate R_1 was linear in the whole analysed range. Linear regression results for R_1 relaxation rates were: $r_1 = 1.702 \pm 0.042$ mM^{-1} s^{-1} for MR NC samples, and 1.447 ± 0.016 mM^{-1} s^{-1} for MR NCx samples. The specific relaxivity r_2/r_1 ratio was: 463 ± 19 for MR NC and 491 ± 17 for MR NCx.

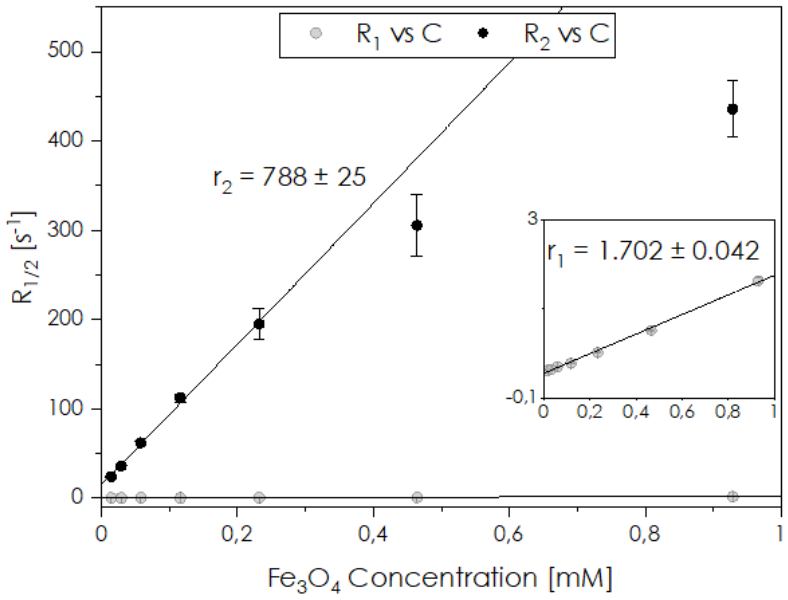

Figure 38 Dependence of relaxation rates on nanocarriers concentration for MR NC 2 – MR NC 128 samples

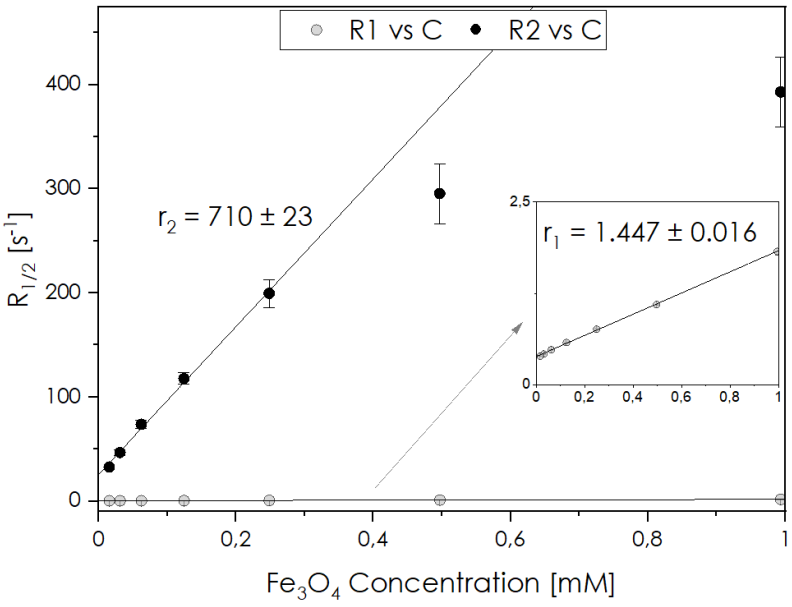

Figure 39 Dependence of relaxation rates on nanocarriers concentration for MR NCx 2 – MR NCx 128 samples

Due to the presence of Fe_3O_4 in the shell of both types of nanocapsules, they cause a much stronger shortening of T_2 than for T_1. The very high value of r_2 specific relaxivity (and r_2/r_1 ratio) makes them excellent negative contrast agents. The MR contrasting

properties of both types of magnetically responsive polyelectrolyte nanocapsules were evaluated on MR images.

Figure 40 and Figure 43 present axial MSME images (TR = 6000 ms, TE = 8 ms or 105 ms, FA: 180°, FOV: 40 × 40 mm, slice thickness: 2 mm) of agarose phantoms of MR NC and MR NCx nanocapsules, respectively. Areas of different signal intensities correspond to NCs concentrations as marked in the figures. The MR images for high and low NPs concentration ranges are compared separately to adjust imaging parameters that allow for detection of all samples. As mentioned above, for both types of NCs for samples of the highest concentrations (1.857 mM Fe_3O_4 for MR NC and 1.968 mM for MR NCx) very rapid signal decay (to the level of the background) was observed, resulting in extremely high contrast between those samples and references (samples without contrast agents), even for a very short 3.7 ms echo time.

However, as such high concentrations are very unlikely to be achieved in vivo, contrasting properties of NCs were further analysed for samples in a lower concentration range (0.015 - 0.232 mM Fe_3O_4 for MR NC and 0.016 - 0.248 mM Fe_3O_4 for MR NCx samples). Figure 41 and Figure 44 present a series of images obtained with different echo times for MR NC and MR NCx samples, respectively. In images with long repetition and echo times (T_2-weighted images), very effective darkening in areas of higher NCs accumulation was observed, confirming strong negative contrast.

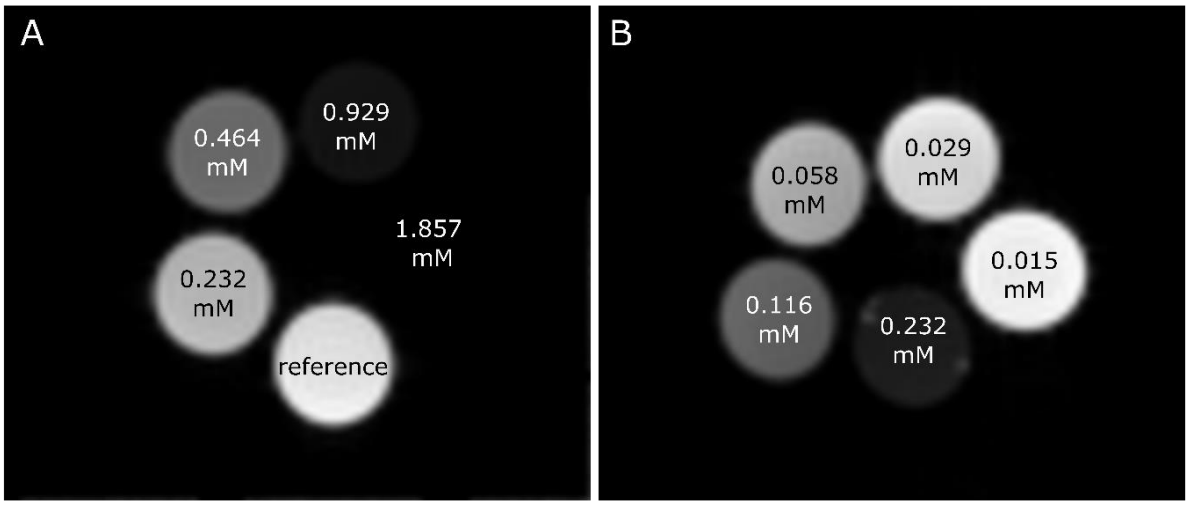

Figure 40 Axial images of samples containing different concentrations of polyelectrolyte nanocapsules (MR NC). RARE VTR sequence: TR: 772 ms, FA: 180°, FOV: 40 × 40 mm, slice thickness: 2 mm; TE = 3.7 ms (A) and 14.8 ms (B). Concentrations of Fe_3O_4 as marked in pictures.

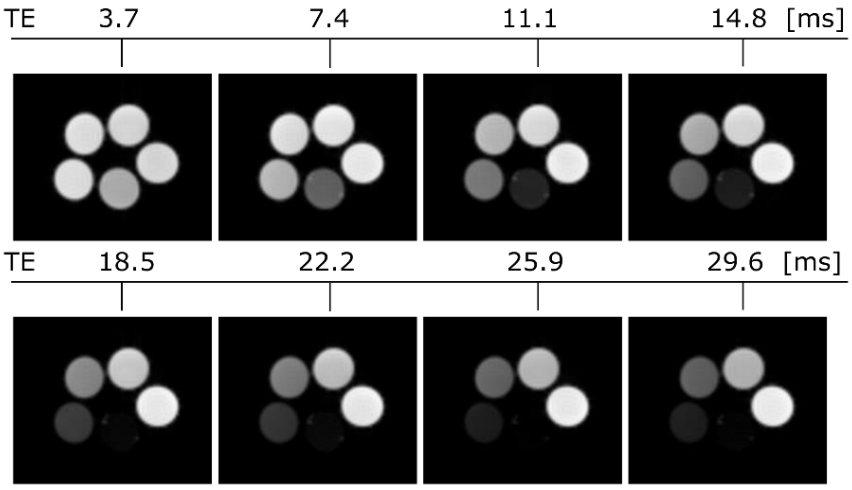

Figure 41 MR images of samples MR NC 8B – MR NC 128 collected with different echo times. Concentrations of Fe_3O_4 as in Figure 40 B. RARE VTR sequence: TR: 772 ms, FA: 180°, FOV: 40 × 40 mm, slice thickness: 2 mm; TE as marked above each image

The contrast was evaluated for samples of the lower concentration range of contrast agent, so for samples: MR NC 8B – MR NC 128. The sample MR NC 128 (c = 0.015 mM) was treated as a reference, as the sample referred to as a reference in Figure 40 A contains nanocapsules without Fe_3O_4 NPs in the shell at a high concentration equal to the sample of the highest concentration, which also alters the relaxation time but due to a different mechanism. Repetition time was 5472 ms and a flip angle 180°. For each concentration, the optimal echo time can be found as the maximum of the curve: $TE_{opt\ (MR\ NC\ 128/\ 64\ )} = 29.6\ ms$, $TE_{opt\ (MR\ NC\ 128/\ 32)} = 25.9\ ms$, $TE_{opt\ (MR\ NC\ 128/\ 16)} = 18.5$, $TE_{opt\ (MR\ NC\ 128/\ 8B)} = 11.1\ ms$.

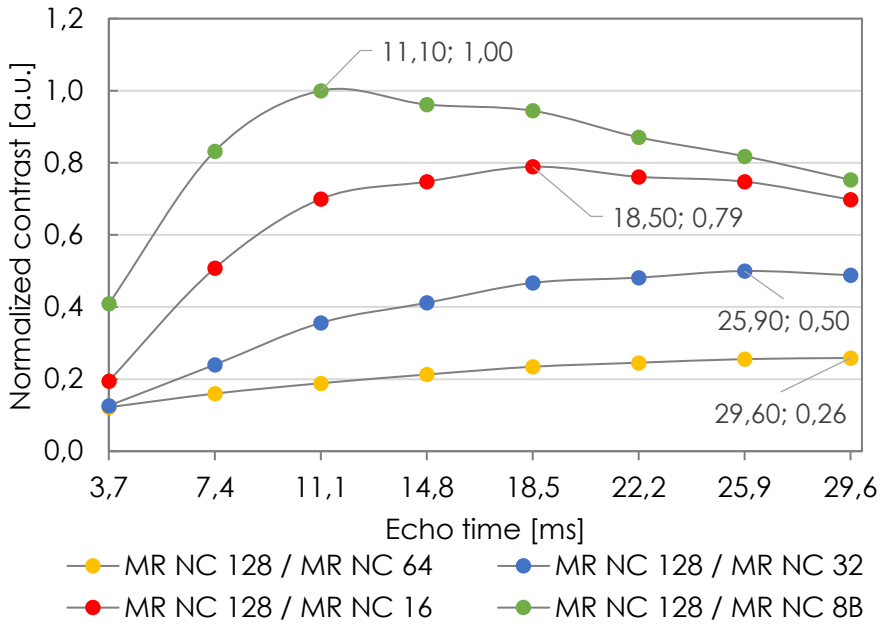

Figure 42 Contrast dependence on Echo Time for samples MR NC 8B - MR NC 128

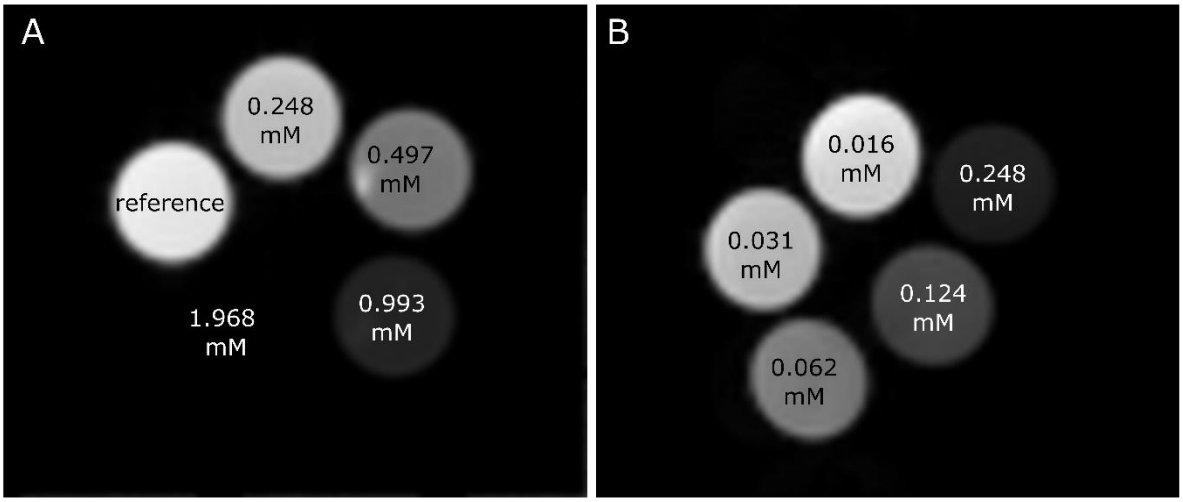

Figure 43 Axial images of samples containing different concentrations of polyelectrolyte nanocapsules (MR NCx). RARE VTR sequence: TR: 772 ms, FA: 180°, FOV: 40 × 40 mm, slice thickness: 2 mm; TE = 3.7 ms (A) and 14.8 ms (B). Concentrations of Fe_3O_4 as marked in the image

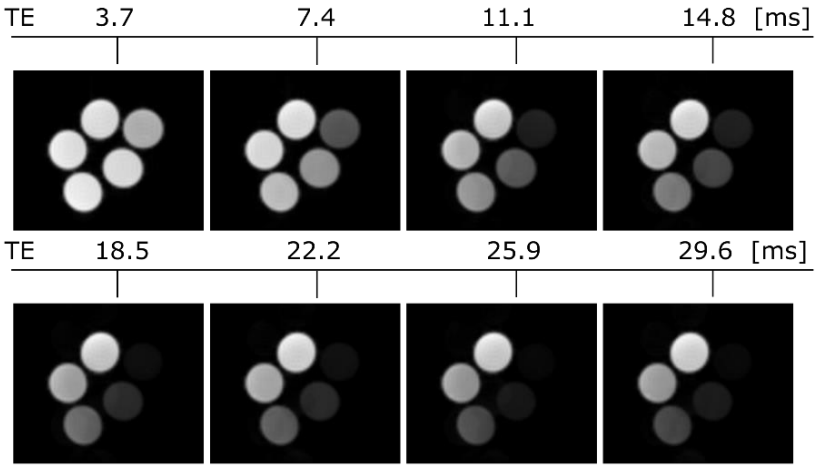

Figure 44 MR images of samples MR NCx 8B – MR NC 128x collected with different echo times. Concentrations of Fe_3O_4 as in Figure 43 B. RARE VTR sequence: TR: 772 ms, FA: 180°, FOV: 40 × 40 mm, slice thickness: 2 mm; TE as marked above each image

Contrast evaluation for samples: MR NCx 8B – MR NCx 128 was performed in the same way as for samples MR NC 08 – MR NC 128, i.e. the sample with the lowest nanocarriers concentration, MR NCx 128 (c = 0.016 mM), was treated as a reference. Repetition time was 5472 ms, and a flip angle 180°. For each concentration, the optimal echo time can be found as the maximum of the curve: $TE_{opt\ (MR\ NCx\ 128/\ MR\ NCx\ 64\ )} = 25.9\ ms$, $TE_{opt\ (MR\ NCx\ 128/\ MR\ NCx\ 32)} = 25.9\ ms$, $TE_{opt\ (MR\ NCx\ 128/\ MR\ NCx\ 16)} = 18.5$, $TE_{opt\ (MR\ NC\ 128/\ MR\ NCx\ 8B)} = 11.1\ ms$.

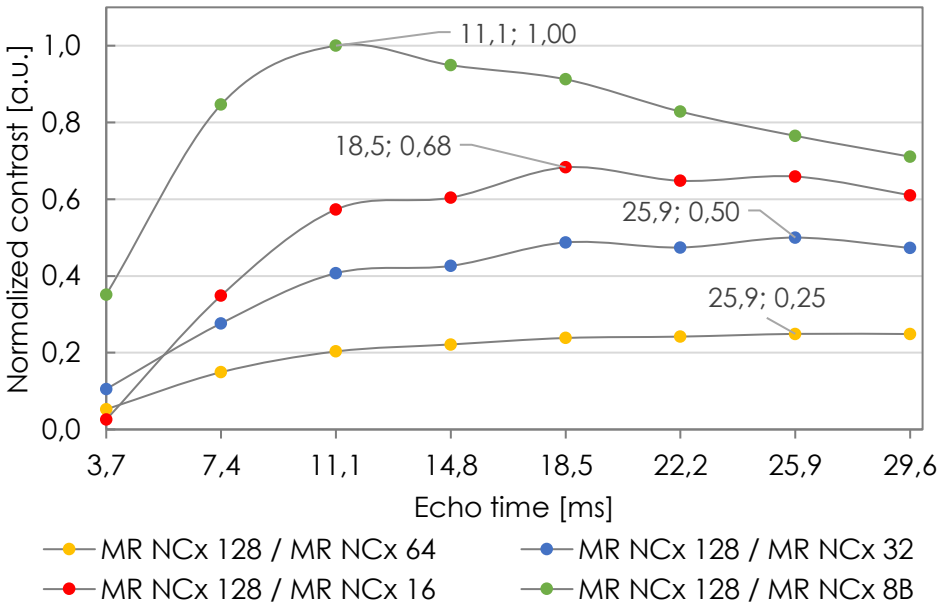

Figure 45 Contrast dependence on Echo Time for samples MR NCx 8B - MR NCx 128

4.2. Nanocarriers containing Gd complexes

In this group, two types of nanocarriers were investigated: with nanoemulsion (samples AOT/PLL-Gd) and polymeric (samples PCL/AOT/PLL-Gd) cores. For investigation of T_1 and T_2 relaxation times changes induced by nanocarriers, agarose gel phantoms with varied NCs concentrations were prepared.

All samples were measured with the same sequences and the same parameters. For measurements of T_2 values, a MSME sequence with the following parameters was applied: FOV: 30 × 30 mm, slice thickness: 2.0 mm, MTX: 256 × 256, TR: 6000 ms. Sixteen echo time values were used to fully sample the T_2 decay curve: TE = (11, 22, 33, …, 176 ms).

Next, the RAREVTR sequence was used for the measurement of the T_1 relaxation times of samples of both types. Six TR values (5500, 3000, 1500, 800, 400 and 200 ms) and five TE values (10, 30, 50, 70 and 90 ms) were used. Other imaging parameters were as follows: RARE factor: 2, FOV: 30 × 30 mm, slice thickness: 2.0 mm, MTX: 256 × 256.

Mean signal intensities in regions of interest for varied echo and repetition times were fitted directly in ParaVision software using the Image Sequence Analysis (ISA) module. Results of T_1 and T_2 relaxation times and corresponding relaxation rates are presented in Table 12.

Table 12 Magnetic resonance relaxametry results for AOT/PLL-Gd and PCL/AOT/PLL-Gd samples

Sample	Gd concentration [mM]	T_1 [ms]	R_1 [s^{-1}]	T_2 [ms]	R_2 [s^{-1}]
AOT/PLL	0	2615 ± 42	0.38 ± 0.0061	80.12 ± 0.82	12.48 ± 0.13
AOT/PLL-Gd 1	0.0036	2388 ± 28	0.42 ± 0.0048	66.83 ± 2.75	14.96 ± 0.62
AOT/PLL-Gd 2	0.0073	2205 ± 30	0.45 ± 0.0062	67.71 ± 1.86	14.77 ± 0.41
AOT/PLL-Gd 3	0.0182	1777 ± 31	0.56 ± 0.0097	66.83 ± 2.75	12.32 ± 0.89
PCL/AOT/ PLL	0	2635 ± 11	0.38 ± 0.0016	56.36 ± 0.33	17.74 ± 0.11
PCL/AOT/ PLL-Gd 1	0.0036	2405 ± 15	0.42 ± 0.0026	55.34 + 0.80	18.07 ± 0.27
PCL/AOT/ PLL-Gd 2	0.0073	2221 ± 17	0.45 ± 0.0034	56.01 ± 1.16	17.85 ± 0.37
PCL/AOT/ PLL-Gd 3	0.0182	1909 ± 11	0.52 ± 0.0030	59.22 ± 1.23	16.89 ± 0.35

The obtained values of R_1 and R_2 relaxivities for both types of nanocarriers were plotted as a function of NCs concentration (expressed by the concentration of Gd). For R_1, a good linear dependence of concentration on R_1 relaxation rates was observed (adj. R^2 > 0.98 for PCL/AOT/PLL-Gd samples and > 0.99 for samples AOT/PLL-Gd), whereas R_2 values didn't demonstrate any significant tendency, at least in the investigated concentration range (Figure 47). The relationship between relaxation rates R_1 vs. gadolinium concentration for both NCs types is presented in Figure 46. The linear regression results for r_1 specific relaxivities were as follows: 8.11 ± 0.51 $mM^{-1}s^{-1}$ for PCL/AOT/PLL-Gd and 9.97 ± 0.13 $mM^{-1}s^{-1}$ for AOT/PLL-Gd samples. Obtained results showed that examined nanocapsules exhibit beneficial T_1 relaxation properties, while enhancement of T_2 relaxivity was not observed. Therefore, the specific relaxivity r_2 was not taken into consideration.

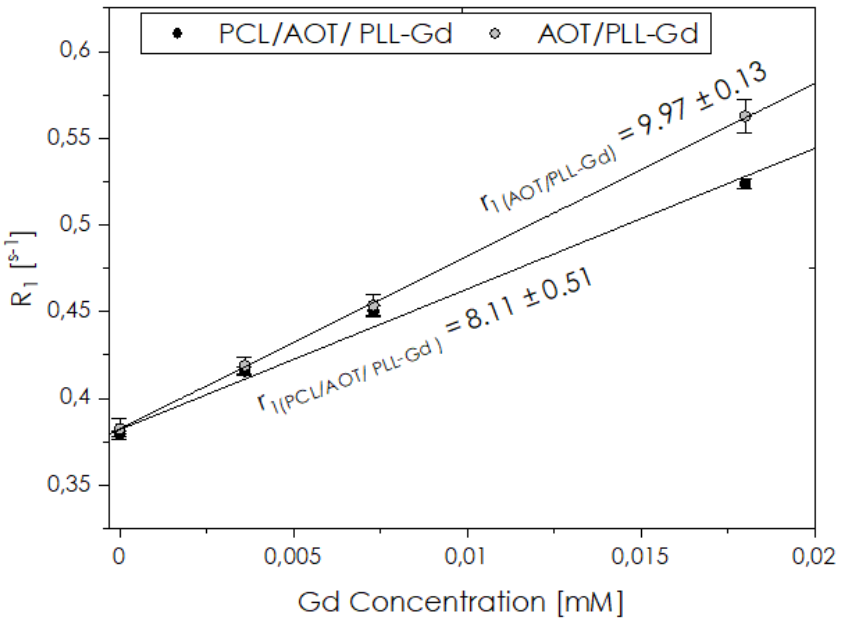

Figure 46 Dependence of R_1 relaxation rates on nanocarriers concentration for PCL/AOT/PLL-Gd and AOT/PLL-Gd samples

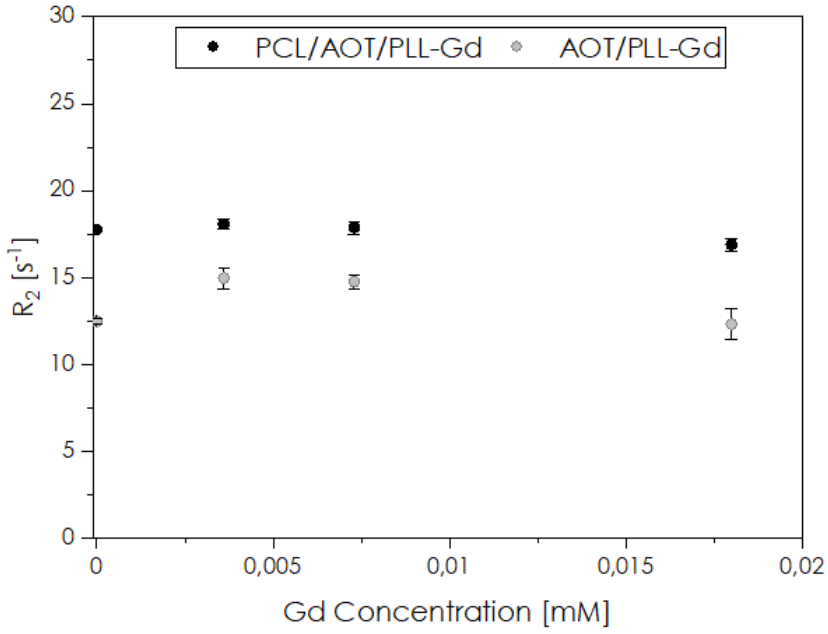

Figure 47 Dependence of R_2 relaxation rates on nanocarriers concentration for PCL/AOT/PLL-Gd and AOT/PLL-Gd samples

High r_1 specific relaxivity values obtained for both types of nanocapsules indicate that they exhibit positive MR contrasting properties, causing the appearance of brighter areas in regions of their higher accumulation. To confirm that, MR images were acquired with short echo and relaxation times. Examples of T_1-weighted images (Figure 48) show that a very good positive contrast between samples with the highest concentration of NCs and reference samples with nanocapsules without Gd complexes can be achieved.

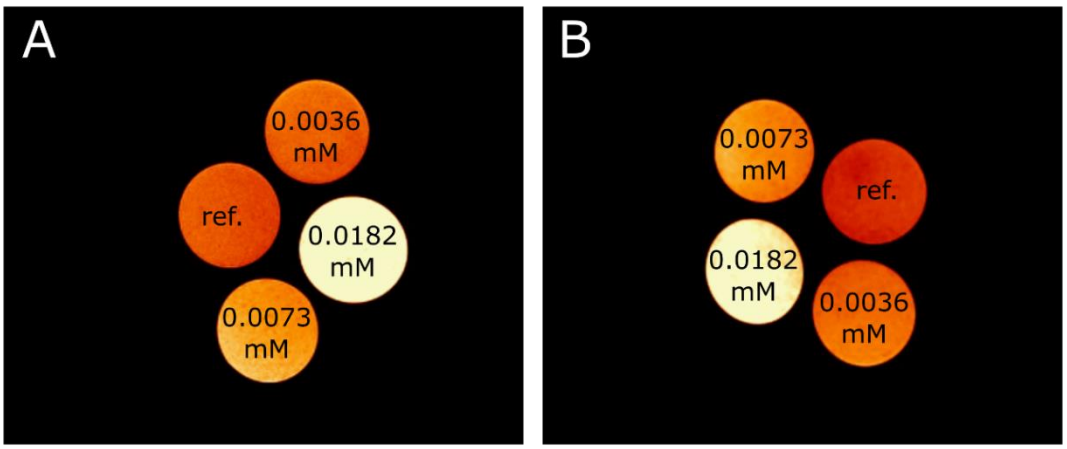

Figure 48 Comparison of MR image intensities for agar gel phantoms with different Gd concentrations as displayed in the figure. T1-weighted images of A) PCL/AOT/PLL-Gd nanocapsules, B) AOT/PLL-Gd nanocapsules; MSME sequence (with single), TR = 200 ms, TE = 10.5 ms

4.3. Nanocarriers containing ^{19}F nuclei

In this group, two types of nanocarriers were investigated. The first type was polyelectrolyte multilayer nanocapsules loaded with an anticancer drug (paclitaxel), where Nafion™ polymer used as a direct detection contrast agent was built into a nanocapsules' shell. The other type was also polyelectrolyte nanocapsules, however, this time ^{19}F-containing anticancer drug (5-fluorouracil) was encapsulated inside the NCs that serve as both therapeutic, and a ^{19}F MRI-detectable agent [121].

Opposingly to standard contrast substances, ^{19}F-containing agents do not induce significant changes in T_1 and T_2 relaxation times of the medium in the accumulation area. In this case, a contrasting effect is achieved by imaging on ^{19}F nuclei and imposing the MR image of their spatial distribution over the standard anatomical image on protons. For that reason, the contrasting efficiency of those so-called hot-spot agents is evaluated based on values of the signal-to-noise ratio achieved in ^{19}F MR images. As the signal from ^{19}F compounds in-vivo is usually only a little above detection limits, the low SNR is the biggest challenge in ^{19}F imaging. Therefore, the main objective in ^{19}F imaging is to optimize the imaging conditions to reliably determine the location of ^{19}F-containing agents.

4.3.1. Nafion™-Based Theranostic Nanocapsules

The first type of investigated ^{19}F-containing contrast agents were polyelectrolyte nanocapsules with Nafion™ (ethanesulfonyl fluoride, 2-[1-[difluoro-[(trifluoroethenyl)oxy]methyl]-1,2,2,2-tetrafluoroethoxy]-1,1,2,2,-tetrafluoro-, with tetrafluoroethylene) built into two layers of the NCs shell. The chemical structure of Nafion™ is presented in Figure 49, which illustrates the variability of the material i.e. unreported by a vendor co-monomer distribution of molecular groups x and y, which results in differences in ^{19}F signal strength arising from specified fluorine groups from one synthesis to another [122].

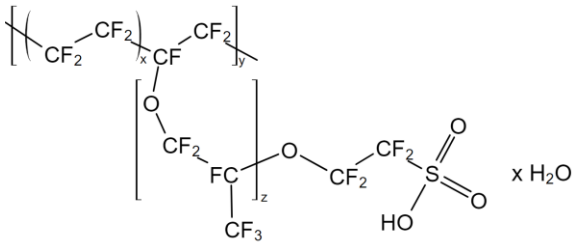

Figure 49 Nafion™ chemical structure

The initial material used in experiments was Nafion™ 20 wt. % solution in lower aliphatic alcohols and water (663492 Sigma-Aldrich). This solution was used first to acquire the ^{19}F NMR spectrum of Nafion™ to prepare imaging experiments, i.e. to set imaging sequence parameters to values enabling optimal visualization of NCs distribution. Figure 50b presents a full acquired spectrum of Nafion™ solution with five visible resonances, which have been assigned to chemical groups of MR equivalent fluorine nuclei as marked with adequate colours on chemical structure (Figure 50a). Hexafluorobenzene (10 µl C_6F_6) was used as the reference.

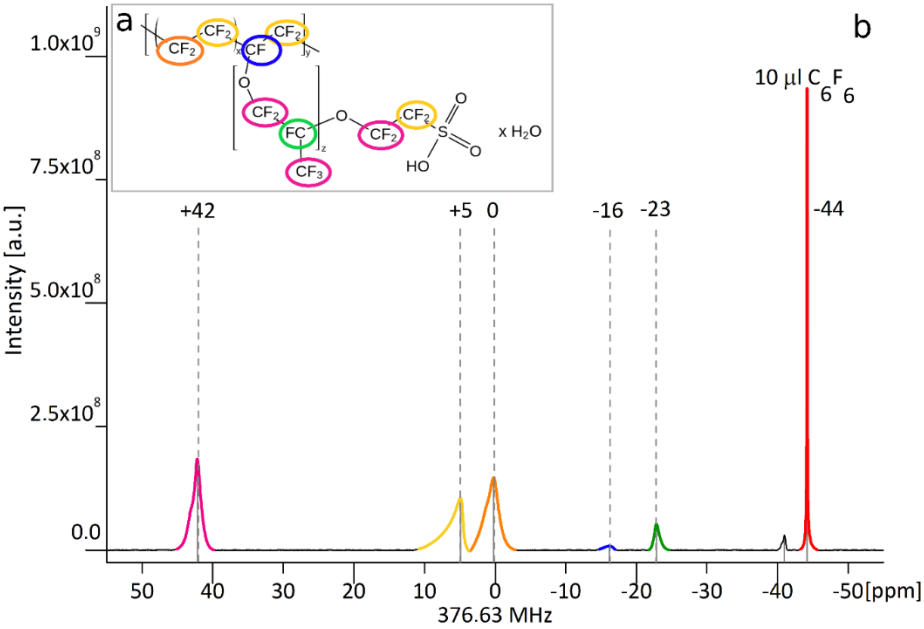

Figure 50. (b) ^{19}F MR spectrum of initial Nafion™ with C_6F_6 used as a reference. Different colors correspond to individual chemical groups, as marked on chemical structure in (a)

Next, T_1 relaxation times of each resonance were measured in TopSpin 2.0 using the Inversion Recovery method, while T_2 values were estimated by calculating the reciprocal of their full width at half maximum (FWHM). Obtained relaxation times were

in the range from 691 to 910 ms for T_1, and of single milliseconds for T_2. The T_1 and T_2 relaxation times, as well as half-widths of spectral lines and chemical groups assignment are presented in the table below.

Table 13 T_1 and T_2 relaxation times and FWHM values of the observed resonances with chemical groups assignment

Chemical Shift (ppm)	Corresponding Chemical Groups	FWHM (Hz)	T_1 (ms)	T_2 (ms)
+42	OCF_2, OCF_2, CF_3	483	909	2.1
+5	CF_2, CF_2, SCF_2	739	691	1.4
0	$(CF_2)_a$	789	733	1.3
−16	CF (II)	640	775	1.6
−23	CF (I)	329	864	3.0

In the next step, three dilutions in the water of the initial Nafion™ solution were prepared to investigate the detection limit. For the estimation of the minimal number of ^{19}F nuclei in a sample that can be visualized in reasonable scan time, hexafluorobenzene (C_6F_6) was used as a reference substance.

In MR imaging, it is preferable to use the signal arising from a single peak; otherwise, ghost artifacts, being a superposition of two (or more) images obtained for signals with different frequencies, are observed. For that reason, to obtain good quality images with the least apparent artifacts, a peak at +42 ppm was chosen, as it exhibits a relatively high MR signal and is well separated from the other resonances. Based on a difference in the area under this peak for subsequent dilutions with respect to signal intensity from the standard, an estimation of the number of ^{19}F nuclei in 1 ml of the sample that contributed to the image was made (Figure 51). Using equivalent weight formula EW = 100x + 446 [122], and an EW value of 1100 g/mole (reported by the vendor), the average x length in the Nafion™ molecule (Figure 49) was calculated. Next, using this value, and therefore assuming the average length of x chain was 6.6, the molar concentration of Nafion™ was estimated (Table 14).

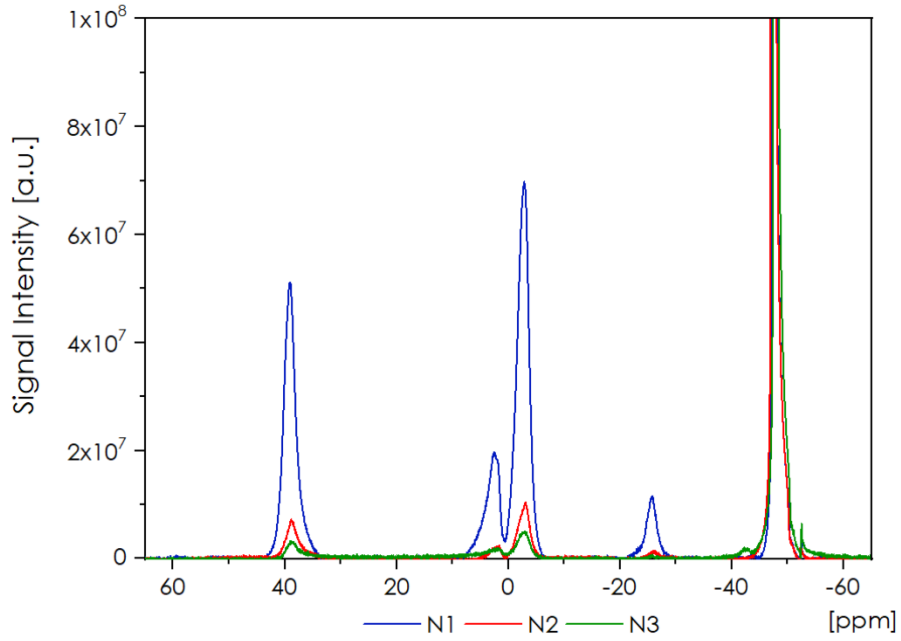

Figure 51 Acquired ^{19}F MR spectra of solutions with different Nafion™ concentrations

Table 14 Estimated number of ^{19}F nuclei in 1 ml of the sample

Sample	Content of initial Nafion™ solution in H_20 dilution [ml]	Number of ^{19}F nuclei in 1ml of the sample contributing to + 42 ppm peak	Total number of ^{19}F nuclei in 1ml of the sample	Estimated Nafion™ concentration in the sample [mM]
N0	1.000	6.4×10^{20}	2.1×10^{21}	88.50
N1	0.100	4.5 s 10^{19}	1.5×10^{20}	6.32
N2	0.010	6.0×10^{18}	2.0×10^{19}	0.84
N3	0.005	2.8×10^{18}	9.2×10^{18}	0.39

Next, MR imaging was performed for the initial solution of Nafion™ and N1-N3 dilutions. There are only a few commercially available sequences that allow the imaging of very rapidly-relaxing components. These include the ultrashort echo time (UTE) or its 3D implementation (UTE 3D), and the zero-echo time (ZTE) imaging sequences. The UTE 3D sequence was applied and the imaging parameters were optimised based on results from MR relaxometry and spectroscopy to values as follows: TR: 8 ms, TE: 0.16 ms, RF pulse BW: 4.27 kHz, FOV: 4.0 x 4.0 x 4.0 cm. For ^{1}H images, MTX: 128 x 128 x 128 and NA: 1 were used, resulting in a total acquisition time of ~6m 51s, while for ^{19}F images: MTX: 32 x 32 x 32, NA: 64, and acquisition time: ~27m 6s were applied. The FA was set at 6.4° taking into account the modified Ernst angle formula [123].

Results of MR imaging of initial 20% Nafion™ solution and N1 - N3 dilutions are presented in Table 15, where the first second column contains ^{1}H MR images of Nafion™ solutions of a different concentration; the third column - corresponding ^{19}F MR images, and fourth column - an overlay of ^{1}H and ^{19}F images. The SNR value in the last column was calculated as a quotient of the mean signal intensity in the area of the sample and the mean signal intensity measured with an entirely attenuated (150.00 dB) RF pulse. In the selected time frame below 30 minutes, that would be reasonable for preclinical in-vivo imaging, for N0 sample SNR value was higher than 600. Therefore, imaging with only one average would still produce an image with a very high SNR in order of 75. For sample N3 with the lowest ^{19}F content, SNR was equal to around five. However, due to close to zero ^{19}F background signal in the organism, this value would still be sufficient to reliably determine the spatial distribution of ^{19}F nuclei.

Table 15 MR Imaging results for samples N0 – N3. Series of ^{1}H and ^{19}F axial images with absolute intensities as displayed on bars.

Sample	^{1}H image	^{19}F image	Overlay	SNR (^{19}F)
N0	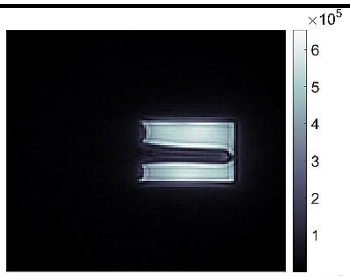	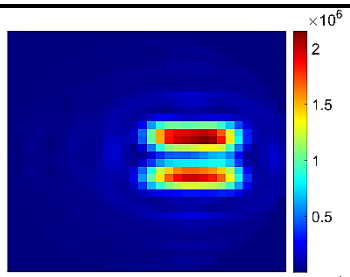	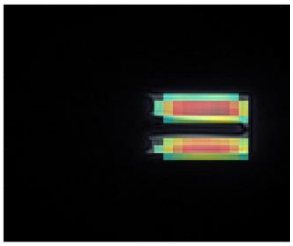	674
N1	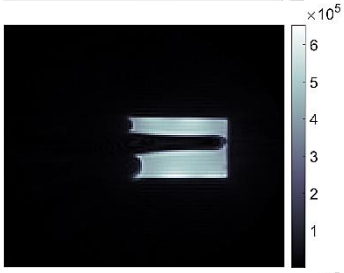	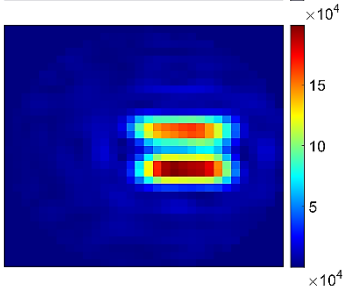	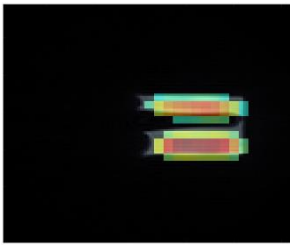	69
N2	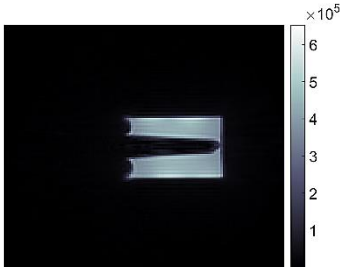	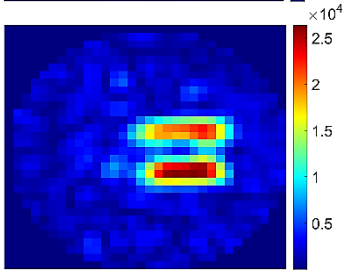	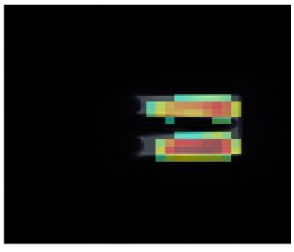	7

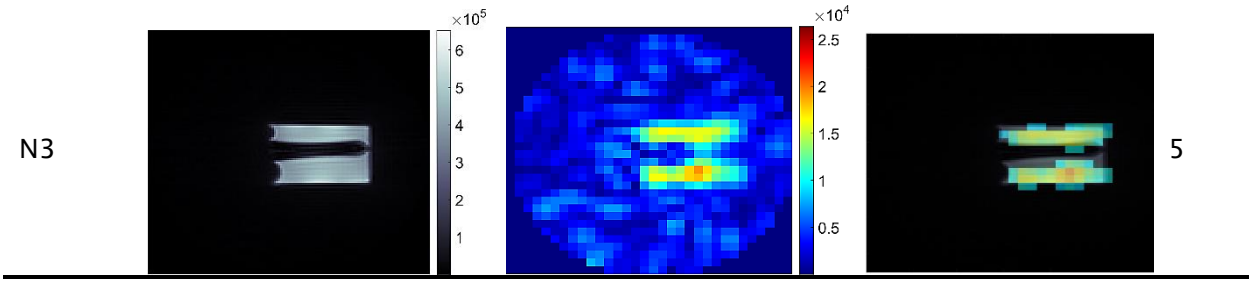

The next part of the investigation covered the imaging of the sample with polyelectrolyte nanocapsules containing Nafion™ in two layers of the shell. First, the MR spectroscopy was performed to examine if the incorporation of the Nafion™ in the nanocapsules' shell results in significant changes in the ^{19}F spectrum. The comparison of MR spectroscopy results for NCs and Nafion™ solution (sample N1) is presented in Figure 52. No significant changes in frequencies for corresponding peaks that would result in alteration of basic frequency for imaging were observed. However, the peak broadening in the range of between 1.5 to 2 times for the main peaks at 42 ppm and 0 ppm was observed. This result corresponds to even shorter T_2 relaxation times in the range of 1 – 1.5 ms, and therefore, a rapidly decaying FID signal available for imaging.

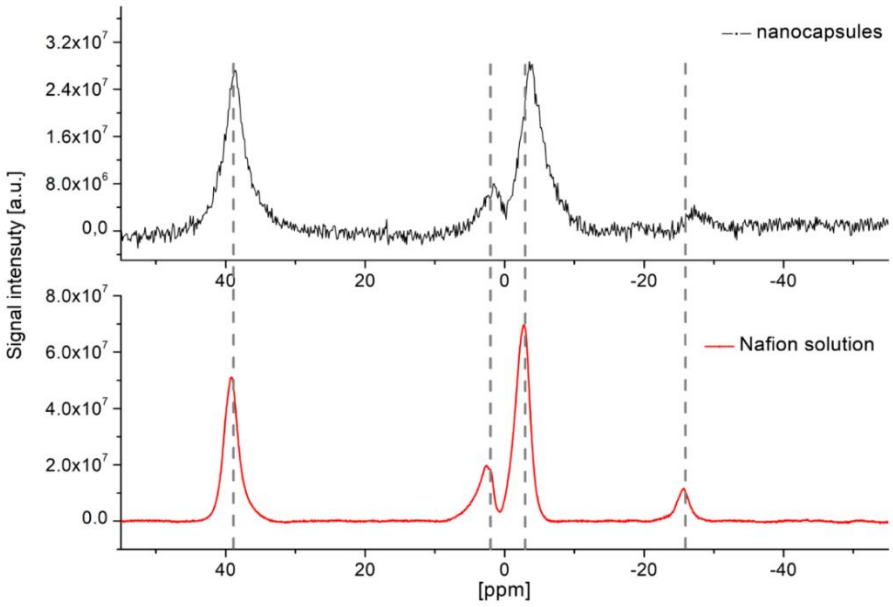

Figure 52 Comparison of acquired ^{19}F MR spectra of Nafion® loaded nanocapsules (NA = 5800) and solution (sample N1, NA = 256).

Subsequently, UTE3D imaging of a phantom containing theranostic nanocarriers with Nafion™ was performed (Figure 53). The imaging parameters were as follows: TR: 8 ms, TE: 0.16 ms, FA: 6.4°, RF pulse BW: 4.27 kHz, FOV: 4.0x4.0x4.0cm. For ^{1}H images: MTX: 128x128x128 and NA: 1 were applied, which resulted in an acquisition time ~6m 51s, while for ^{19}F images, MTX: 32x32x32, and NA: 256 or 500 were applied, resulting in a total acquisition time of ~1h 48min 24s and ~3h 31m 44s, respectively.

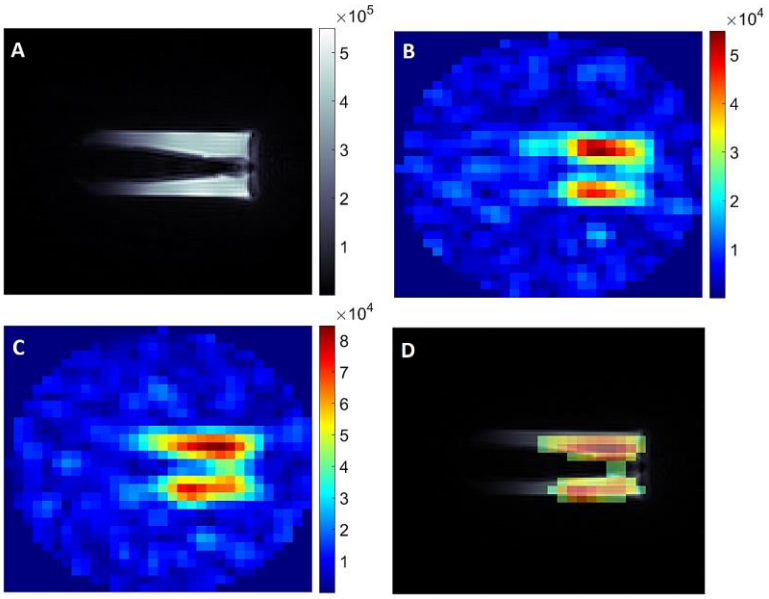

Figure 53 MR Imaging of Nafion™-containing nanocapsules. (A) ^{1}H MR Image of a phantom containing nanocapsules (UTE3D, FOV: 4.0 cm, MTX: 128, NA:1), (B, C) corresponding ^{19}F MR images (UTE 3D, NA: 256 and 500 respectively) and (D) an overlay of ^{1}H and ^{19}F (C) images.

The UTE 3D imaging of theranostic nanocapsules with 256 averages gave SNR = 12. Increasing the number of averages to 500 (acq. time: ~3h 32 min) caused an improvement in SNR to around 20. As the SNR is proportional to $\sqrt{NA}$, we can estimate that for 64 averages that have been used for imaging of Nafion™ dilutions in water, its value would be around 3, which would still be enough to localize ^{19}F nuclei in the space. By comparing this value with values obtained for dilutions, it can be predicted that the Nafion™ concentration in the sample with NCs was similar to the concentration of the N3 sample (9.2 x 10^{18} ^{19}F nuclei/ml).

4.3.2. Polyelectrolyte nanocapsules with 5-FU

The last type of investigated theranostic nanocarriers was polyelectrolyte nanocapsules with 5-fluorouracil (5-Fluor-1,2,3,4-tetrahydropyrimidin-2,4-dion). Contrary to Nafion™, all fluorine atoms in the 5-FU molecule are MR equivalent, therefore a simple NMR spectrum with one sharp peak is expected.

The ^{19}F NMR spectrum of theranostic nanocapsules with 5-fluorouracil was measured with an added 55 µl of 10 g/l solution of NaF in distilled water using a small transmit-receive ribbon solenoid RF coil (ID of 14 mm), which can be tuned either to ^{1}H or ^{19}F resonant frequency (i.e. 400.130 vs. 376.498 MHz). The results of ^{19}F MR spectroscopy for 5-FU NCs are presented in Figure 54. Based on the difference in peak integrals, the content of ^{19}F nuclei in nanocapsules and the 5-fluorouracil concentration in the sample was calculated. The peak observed for 5-FU corresponds to 4.55×10^{18} ^{19}F nuclei, which is equivalent to 983 mg/l fluorouracil concentration.

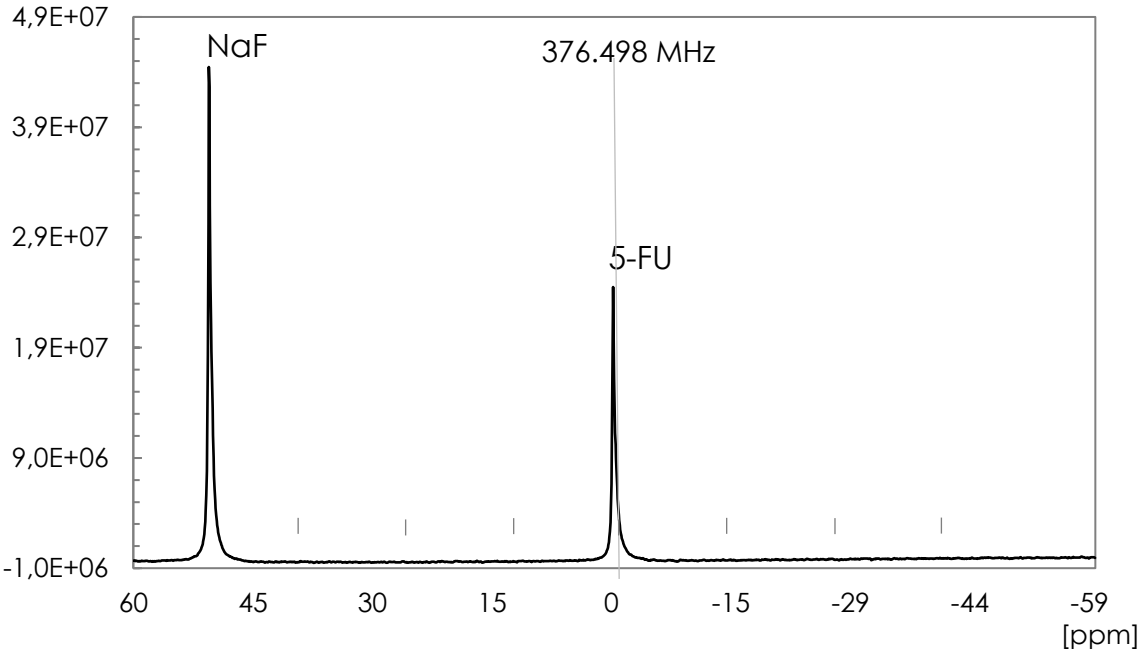

Figure 54 ^{19}F MR spectrum of 5-FU NCs with NaF used as a reference for concentration measurement.

To assess if the formation of a 5-fluorouracil/AOT/PLL nanocore affects the structure and properties of 5-FU, the ^{19}F MR spectrum obtained for nanocores was

compared with the spectrum of a 5-fluorouracil solution for injections (50 mg/ml). Both spectra are presented in Figure 52. No significant changes in frequencies or broadening of corresponding peaks were observed, which suggests no or very weak interaction between liquid 5-fluorouracil cargo and the AOT/PLL interfacial layer.

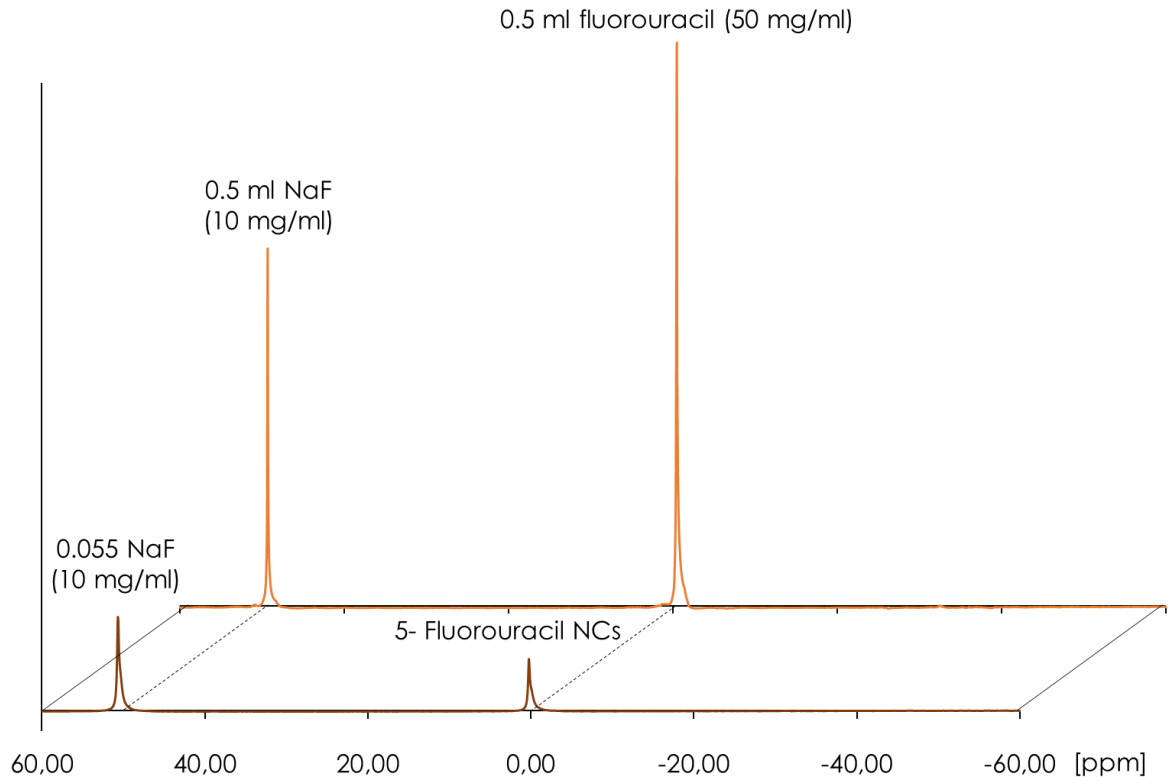

Figure 55 Comparison of acquired ^{19}F MR spectra of 5-fluorouracil nanocores and Fluorouracil 50 mg/ml Solution for Injection

To calculate the optimal flip angle for the imaging part of experiments, the T_1 value was measured. For that, the Inversion recovery method was used (Figure 56). Experimental points were measured for: 30000, 20000, 15000, 10000, 5000, 4500, 4000, 3750, 3500, 3250, 3000, 2000, 1000, 500, 100 ms inversion recovery times. For measured points function: $I(t) = I_0\left(1 - 2e^{(-t/T1)}\right)$ was fitted resulting in T_1 = 3.23 ± 0.12s.

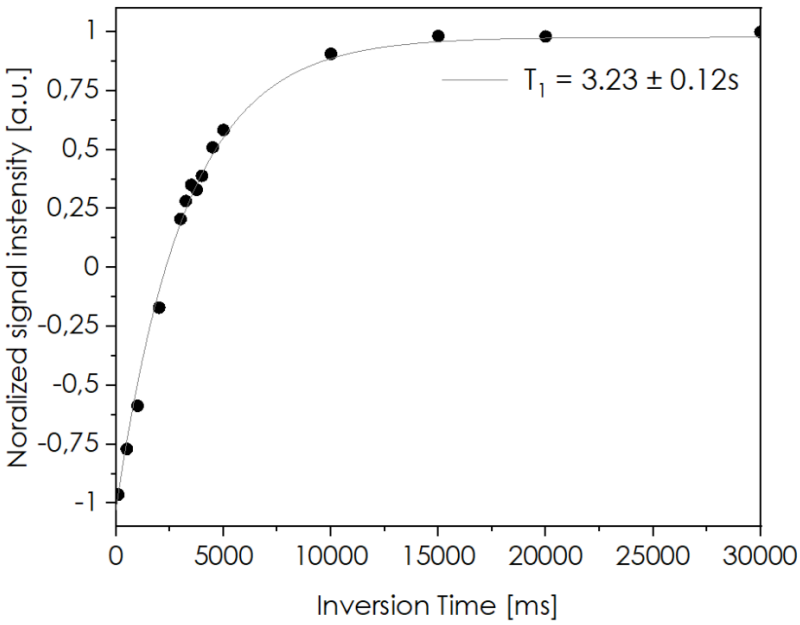

Figure 56 T_1 relaxation time of 5-FU nanocapsules

For the acquisition of axial ^{1}H and ^{19}F images, the FLASH sequence was used. For ^{1}H images, sequence parameters were as follows: TE: 6 ms, FA: 30°, TR: 100 ms, NA: 4, total acquisition time: 51 s. ^{19}F imaging was performed at high and low spatial resolution. High-resolution images were acquired with an in-plane resolution of 0.63 mm in both the y and x-direction and with a 4 mm slice. Echo time was 4.7 ms, flip angle 10.1°, and repetition time 50 ms. For low-resolution images, the in-plane resolution was 1.25 mm while slice thickness was kept the same,4 mm. In this case, echo time was 3.1 ms, while flip angle and repetition time remained the same.

^{19}F images were acquired with three different numbers of averages NA = (144, 256, 512) to find the value that would give an acceptable compromise between SNR (Signal-to-noise) value and total acquisition time. SNR was measured as the quotient of the mean value of the signal intensity in the region of interest placed within the sample and the standard deviation of the signal intensity in the region next to it. SNR results obtained for different spatial resolutions are presented in Table 16, and are further visualized in Figure 57, where SNR dependence on the number of acquisitions is presented.

Table 16 Signal to noise values of ^{19}F images obtained for 5-FU nanocapsules

	High Resolution		Low Resolution	
NEX	SNR	Total acquisition time	SNR	Total acquisition time
144	4.9 ± 1.4	7 min 41 s	12.5 ± 1.8	3 min 50 s
256	6.4 ± 1.5	13 min 39 s	17.3 ± 3.3	6 min 50 s
512	8.8 ± 1.3	27 min 18 s	25.5 ± 2.3	13 min 39 s

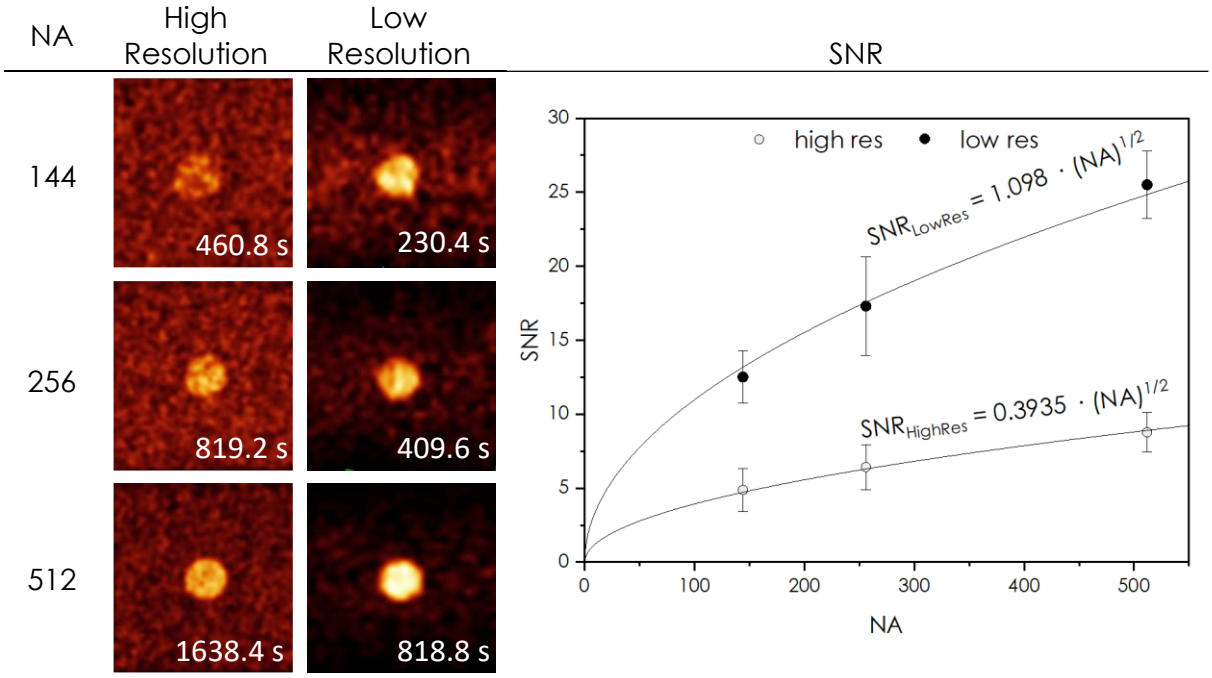

Figure 57 SNR/resolution dependence for 5-FU nanocapsules. Left: NA - number of averages, High resolution - MR images with an in-plane resolution of 0.63 mm, Low resolution – MR images with an in-plane resolution of 1.25 mm, total acquisition time as marked in each image, gaussian filtered σ=5; Right: Signal-to-noise (SNR) dependence on Number of Averages (NA) for 5-FU nanocapsules.

To visualize the distribution of ^{19}F nuclei in the sample, ^{19}F images were overlaid over a standard ^{1}H image. In Figure 58, two extreme cases are presented, with the shortest and the longest acquisition times. Within a total acquisition time of 3 minutes and 50 seconds, the SNR value was equal to approximately 15.5, which is already enough to reliably determine nanocapsules' location. Increasing the number of acquisitions to 1024 (and total acquisition time to 27 min and 18 s) resulted in a very high SNR of 32.5.

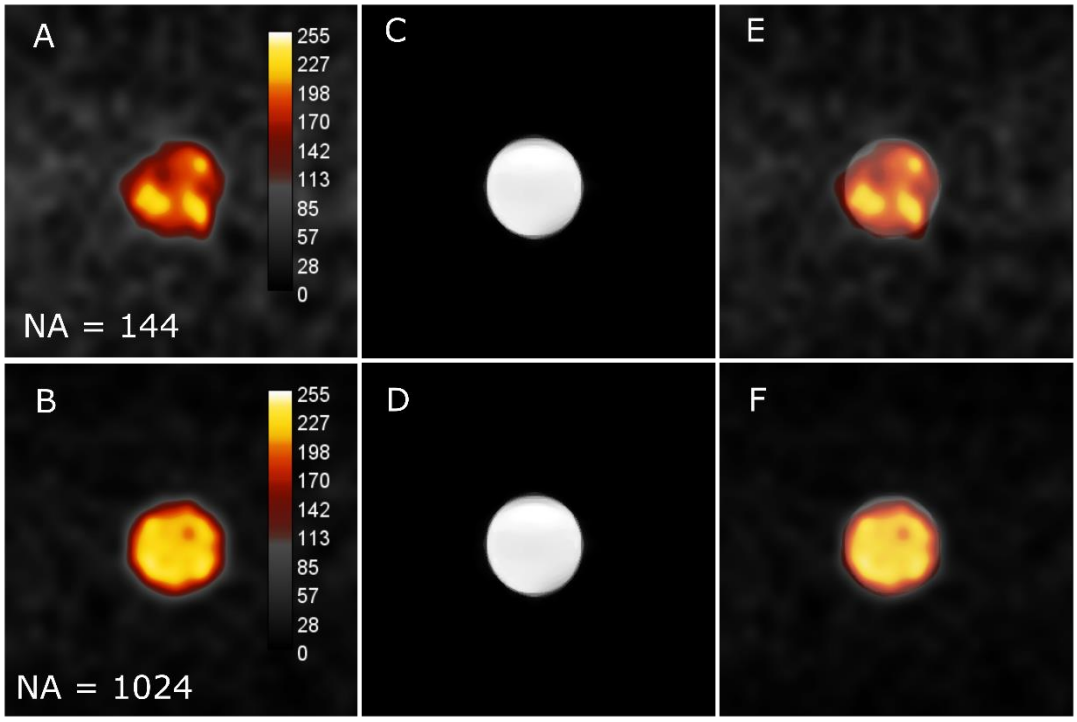

Figure 58 ^{19}F and ^{1}H MR imaging results for 5-FU nanocapsules. A,B – ^{19}F Images (total acquisition time for A: t_A =3 min 50 s, for B: t_B =27 min 18 s); C, D – ^{1}H image; E, F -overlay of ^{19}F and ^{1}H images

Chapter 5

Discussion

5.1. Theranostic nanocarriers with relaxation contrast agents

In this work, theranostic nanocarriers with relaxation contrast agents of both paramagnetic and superparamagnetic types were investigated. Regarding the similarity of the composition and the application of nanocarriers, two groups can be distinguished, namely polyelectrolyte nanocapsules with a multilayer shell for anticancer (paclitaxel) drug delivery and core-shell nanoparticles for photothermal therapy. In the case of polyelectrolyte nanocapsules, variations with paramagnetic (based on gadolinium) and superparamagnetic CAs (based on iron oxides) were investigated. For gadolinium-labeled NCs, two types of nanocarriers were investigated: those with nanoemulsion and those with polymeric cores. For nanocapsules with IONPs, also two types of NCs were formed: one with and one without the AOT surfactant in the shell. The second main group was core-shell nanoparticles for MRI-guided chemo-photothermal therapy. In this case, two different shapes of magnetic Fe_3O_4 core and two SiO_2 shell thickness dimensions were investigated.

5.1.1. Polyelectrolyte nanocapsules for drug delivery

The results of specific relaxivities for nanocapsules for drug delivery labelled with superparamagnetic IONPs are shown in Figure 38 for nanocapsules with the following composition: PCL-PTX/AOT/PLL/PGA/Fe_3O_4/PGA and in Figure 39 for PCL-PTX/PLL/PGA/Fe_3O_4/PGA NCs. To compare those values with commercially available contrast agents, and other nanocarriers present in literature, it is convenient to recalculate relaxivities for Fe concentration instead of Fe_3O_4 (Figure 59). It was hypothesized that there would be no significant difference in the relaxivities of those nanocarriers as the addition of AOT creates an interfacial complex in the vicinity of the

NCs cargo. Therefore, this additional layer is not in direct contact with Fe_3O_4 nanoparticles and also does not limit water diffusion near superparamagnetic centers. Indeed, the difference is less than 10 percent and can be explained by the statistical differences of T_2 values between the measured series of the same types of nanoparticles. For samples with the same Fe_3O_4 concentration, but from different series, the difference in measured T_2 times was in the range of around 8% for samples in the lower concentration range and up to 20% for higher concentrations (see Figure 36 and Figure 37).

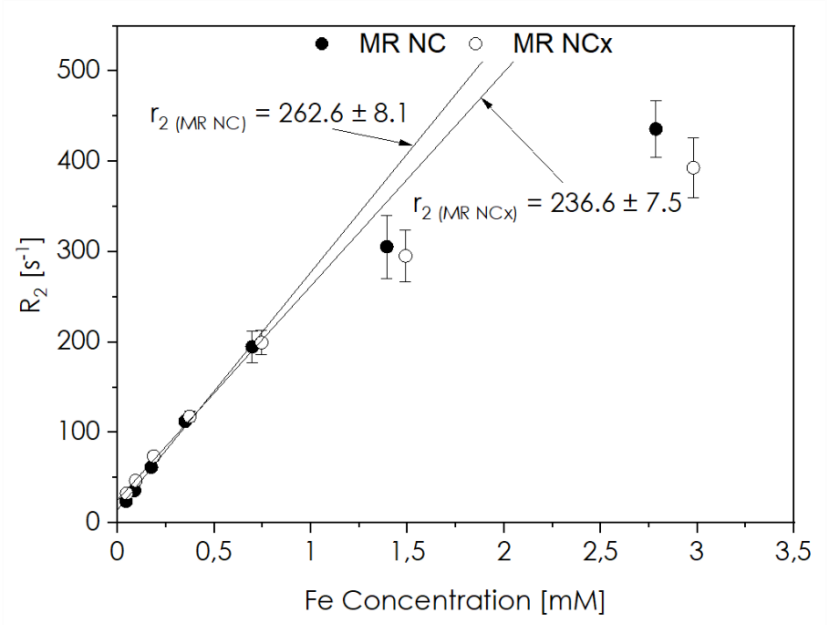

Figure 59 Relaxivities (r_2) comparison for nanocapsules for drug delivery

The average size of the obtained hybrids was ~120 nm (PDI < 0.4) with the mean size of individual Fe_3O_4 nanoparticles used for shell synthesis of 8 ± 3 nm. While the effect on T_1 relaxation times was negligible (r1 = 0. 57 and 0.48 $s^{-1}mM^{-1}$ (Fe) for MR NC and MR NCx NCs respectively), both nanocarrier types displayed very high values of r_2, which were higher than values reported for contrast agents used in clinical practice [14]. This can be attributed to the appropriate surface chemistry that leads to the controlled aggregation of magnetic nanoparticles to form nanoclusters in nanocarriers shells. As a result, higher local saturation magnetization is produced and the effective radius of magnetic field inhomogeneity is extended, resulting in an improved relaxation effect [124].

This phenomenon has been observed before and has been utilized to produce particles having high r_2 values. In [125], a series of nanoclusters of iron oxide NPs of different sizes and shapes (cubes, spheres, plates) were investigated. It was shown that those controlled nanoclusters produce artificially enhanced field inhomogeneity, which results in a 3-8 fold boost in the r_2 value compared to individual NPs. In [126], authors investigated nanoparticles consisting of a biocompatible amphiphilic polymer (Pluronic F127), magnetic nanoparticles (Fe_3O_4) clusters, PTX (paclitaxel), and a hydrophilic polymeric shell derived from stearoyl-polyethyleneimine-2,3-dimethylmalefic anhydride. They reported an r_2 value of 142.68 $mM^{-1}s^{-1}$, which was much higher than the r_2 relaxation rate of contrast agents based on single SPIONs such as the Endorem® and Resovist® (30-50 $mM^{-1}s^{-1}$). Finally, in [127], the impact of nanoparticle arrangement and the overall morphology on the magnetic relaxivity was evaluated. Various morphologies of nanoparticle-encapsulating block-copolymer assemblies were formed with iron oxide NPs of an average diameter of 5.6 nm. The obtained relaxivities were: 154, 64, and 167 $s^{-1}\,mM^{-1}$ for magneto-core shell assemblies, magneto-micelles, and the mixture of magneto-micelles and magneto-polymersomes samples, respectively. The magneto-core shell structure showed a significantly higher relaxivity rate than the simple micelles, while the sizes of the two assemblies and IONPs contents were similar. Very high relaxivity was also observed for magneto-polymersomes (167 – 228 $s^{-1}\,mM^{-1}$ depending on the mass percent of IONPs) that have iron oxide nanoparticles packed in vesicle walls and therefore have a structure similar to the investigated nanocarriers in this thesis.

The obtained high values of r_2 relaxivity result in very strong contrasting effects in T_2-weighted MR images (Figure 40 and Figure 43). To visualize the possibility of achieving high contrast in a wide range of nanocarrier concentrations, images of low and high concentration phantoms were presented. However, to achieve maximum contrast, not only should the accumulation of contrast agents be enhanced, but also the choice of optimal imaging conditions has to be considered. In images with long repetition and echo times, very effective darkening in areas of higher NCs accumulations was observed, confirming the strong negative contrasting properties of nanocarriers.

With Figure 41 and Figure 44, the importance of adjustment of imaging sequence parameters is shown. Only for appropriate echo time values can large contrast be achieved between areas of different accumulations of contrast agent. Therefore, the

evaluation of optimal echo time for the expected concentration of contrast agent is crucial. For that reason, in Figure 42 and Figure 45, the contrast between selected regions of interest corresponding to different concentrations is plotted as a function of echo time. For regions with the largest difference in T_2 relaxation time, the highest contrast is achieved for a relatively short echo time of 11.1 ms for both types of nanocarriers. As the concentration of nanocarriers and the T_2 relaxation time difference between samples get smaller, longer echo times (up to 29.6 ms) are required to achieve sufficient contrast.

Theoretically, to further increase the relaxation properties, it would be advantageous to directly expose nanoparticles to the surrounding. However, for biomedical applications, specific modification of nanocarriers is required to reduce the macrophage cellular uptake and to avoid fast clearance. For that reason, the multilayer shell of the analysed nanocarriers ended with poly-l-glutamic acid (PGA) [128]. Embedding the F_3O_4 NPs in a polymeric multilayer shell preserves their magnetic properties, especially the possibility of being accumulated at the desired site by an external magnetic field. Such an approach results in the increase of the nanocarriers concentration in the region of interest, and the enhancement of both contrasting and therapeutic effects compared to passive targeting. The possibility of magnetic targeting was proven by a simple experiment with a permanent magnet, where nanocarriers suspended in water were attracted to the container wall near the magnet. Naturally, such a test can be treated only as a proof of concept, and for biomedical applications, this has to be further evaluated as the biodistribution of nanocarriers depends not only on factors related to nanocarriers design (size, shape, charge, biocompatibility, and stability), but also on factors related to the environment, like the morphology and vasculature of the tumor. The therapeutic potential of nanocarriers in magnetic hyperthermia was evaluated by the Specific Absorption Rate (SAR) measurement. The 1 mL of MN-PCL NCs suspension, with 1×10^{11} nanocarriers per mL, was treated with a 25 mT magnetic field oscillating at 429 kHz. In such conditions, SAR = 55 ± 1 Wg^{-1} was obtained [112].

Most of the theranostics based on relaxivity contrast agents studied in this thesis and present in literature, use SPIONs as negative contrast agents for T_2-weighted MRI. However, in some pathological events, such as internal bleeding or calcifications, or at the boundaries between air and the tissue, the negative-contrast MRI does not allow the CA

signal to be differentiated from artifacts [129]. In such cases, T_1-weighted MRI-guided theranostics can be used.

Results regarding MR relaxometry and imaging of Gd-labelled nanocapsules are presented in Figure 46 (R_1/concentration dependence), Figure 47 (R_2/concentration dependence), and Figure 48 (imaging). For nanocarriers with nanoemulsion and polymeric core, values of longitudinal relaxivity r_1 were slightly different: 9.97 and 8.11 $m^{-1}Ms^{-1}$, respectively. However, for concentrations up to 0.0073 mM Gd, values of relaxation rates were almost identical. At the same time, for both types of NCs, the contribution of nanocarriers to T_2 relaxation wasn't observed, which means that investigated nanoparticles are perfect positive MRI contrast agents.

The obtained results are comparable with other polymeric assemblies present in the literature. In general, the range of r_1 relaxivity values achievable for polymeric devices is very wide and depends on the structure of the designed nanocarrier. It was mentioned already in the introductory chapter that the r_1 relaxivity is governed by several factors including the number of coordinated fast-exchanging inner-sphere water molecules on the Gd(III) surface, the rotational correlation time of Gd(III), and water exchange from Gd(III) to the bulk phase. Therefore, an appropriate nanocarrier design that leads to prolonged correlation time and allows the effective exchange of water molecules with a bulk pool can result in a significant boost in r_1 relaxivity. For instance, in [130], authors synthesized polymersome molecules from polycaprolactone-poly(ethylene oxide) (PCL-PEO) block copolymers. The surface of as-fabricated nanocapsules was subsequently functionalized with either small molecule or dendritic alkyne derivatives of a DTPA-Gd(III) complex, resulting in ionic relaxivities of 10.6 $mM^{-1}s^{-1}$ and 26.1 $mM^{-1}s^{-1}$, respectively. In the case of small DTPA-Gd molecules, the relaxivity value was very close to the one obtained in this work. A higher r_1 value that was obtained for a dendritic complex of DTPA-Gd(III) is characteristic for dendrimer systems. In [131], authors obtained polymeric nanocapsules from the self-assembly of a lipid-containing copolymer, poly(acrylic acid-co-distearin acrylate) in an aqueous solution, that were loaded with near-infrared detectable fluorophore Cy5.5 and Gd(III) molecules ($GdCl_3$). It was demonstrated the longitudinal relaxivity of as-prepared NCs was are at least 15-fold higher than of the commercially available Magnevist: 65.0 $mM^{-1}s^{-1}$ in pH 7.4 buffer and 58.0 $mM^{-1}s^{-1}$ in PBS. This pronounced enhancement of r_1 was attributed to the entrapment

of Gd(III) species within a highly hydrated vesicle membrane, which prolongs the rotational correlation time of Gd(III) cations and retains high-level water exchange from Gd(III) cations to the bulk solution. A different approach to drug delivery than its encapsulation was proposed in [132], where a polymeric prodrug-based nanotheranostic system with imaging agents (Cy5.5 and Gd(II)) and anticancer (paclitaxel) drug was prepared via polymerization and conjugating chemistry. Those nanoparticles demonstrated high enhancement of r_1 compared to Gd-DTPA (8.6 vs. 3.6 $mM^{-1}s^{-1}$) allowing accurate mapping of the temporal change profile of the tumor volume after injection of NPs.

The sizes of investigated Gd-labelled nanocarriers were in the range of 140–160 nm, which is considered as an optimum dimension suggested for passive tumor targeting based on enhanced permeability and retention (EPR) effect [133]. The toxicity and therapeutic effect of Gd-labelled theranostic nanocarriers were tested on four mouse cancer cell lines: CT26- CEA, B16-F10, and 4 T1 that were incubated with empty polymeric nanocapsules, nanocapsules labelled with Gd, and with Gd-labelled nanocapsules loaded with paclitaxel at a concentration 10^{10} NCs/ml. The exposition of cells to Gd(III) ions released from paramagnetic Gd(III) chelates resulted in observable toxicity, leading to the increase of 5-15 % mortality in cells incubated with either with AOT/PLL-Gd or PCL/AOT/PLL-Gd NCs. Significantly higher cytotoxicity was observed only after incubation of cells with AOT/PLL-Gd-PX NC. Incubation with paclitaxel (0.45 μg/ml) encapsulated in NCs decreased the viability of cells to 55–65%, which was comparable with the effect of incubation with free paclitaxel at the same dose. At the same time, PCL/AOT/PLL-Gd-PX induced very weak toxicity on cancer cells (apart from the B16F10 line, where viability was around 55%), which can be attributed to a much lower paclitaxel concentration of 0.12 μg/ml [107] [112].

5.1.2. Core-shell nanoparticles for photothermal therapy

The second group of investigated theranostic contrast agents with relaxation contrast agents was core-shell nanoparticles for MRI-guided chemo- and photothermal therapy. Those nanoparticles consisted of a magnetic Fe_3O_4 core and a continuous shell of SiO_2 that can be further functionalized with Au and cis-Pt nanoparticles for therapeutic

applications. Here, two geometries of Fe_3O_4 core (cubic and spherical) and two sizes of SiO_2 shell (10 nm and 2 nm) were tested. The table below presents a summary of the dimensions of the investigated nanoparticles.

Table 17 Summary of dimensions of investigated Fe_3O_4@SiO_2 nanoparticles

	Fe_3O_4 core mean size	Fe_3O_4 core calculated volume	SiO_2 shell thickness	m(Fe_3O_4)/m(NP) ratio
Spherical Fe_3O_4@SiO_2 (10 nm) NPs	11 nm	660 nm^3	10 nm	0.091
Cubic Fe_3O_4@SiO_2 (10 nm) NPS	19 nm	2460 nm^3	10 nm	0.167
Cubic Fe_3O_4@SiO_2 (2 nm) NPs	19 nm	2460 nm^3	2 nm	0.610

For the comparison of obtained results with similar studies, relaxivity was recalculated for Fe concentration instead of Fe_3O_4 (Figure 60). Regardless of the shape of the core, nanocarriers with a 10 nm layer of SiO_2 shell exhibited very strong relaxivities equal to 170.6 and 135.5 $s^{-1}mM^{-1}$, while a 2 nm shell layer resulted in a much lower value of 13.2 $s^{-1}mM^{-1}$.

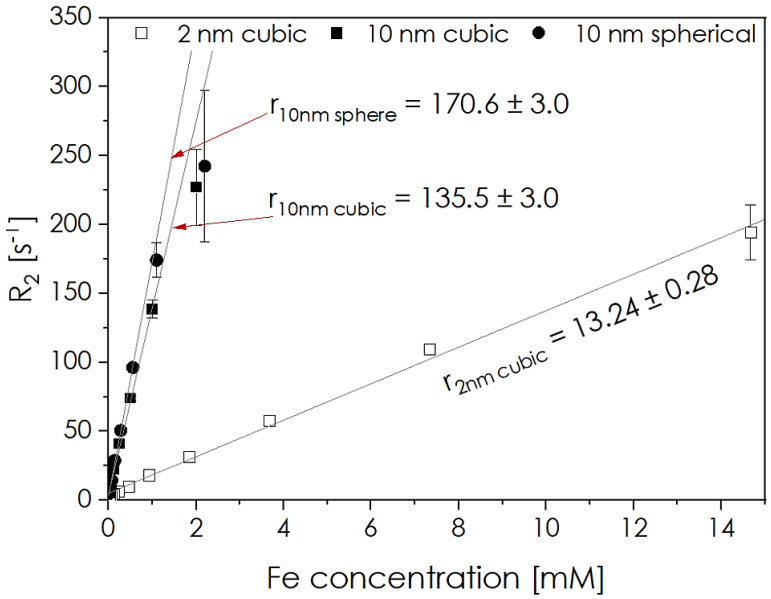

Figure 60 Relaxivities (r_2) comparison for nanoparticles for photothermal therapy

The relaxivity of superparamagnetic contrast agents can be described by equation 29 $\left(r_2 = \frac{256\pi^2\gamma^3}{405}\frac{V^* M_S^2 a^2}{D\left(1+\frac{L}{a}\right)}\right)$. Therefore it is expected that it will increase with nanoparticle radius (a) if the volume fraction (V^*) remains the same. It also states that the decrease in the thickness of a shell (L) and the increase in saturation magnetization (M_S) will result in higher relaxivity. Even though the size of investigated cubic nanoparticles is almost twice as big as that of spherical NPs (19 nm diagonally vs. 11 nm diameter, respectively), for the same shell thickness of 10 nm, the value of r_2 for spherical nanoparticles is higher. In addition, a reduced shape/surface anisotropy, which is related to the surface spin disorder, enhances the magnetization and produces larger perturbations of the magnetic field that are necessary for T_2 relaxation. In particular, it was shown that non-spherical NPs i.e. cubes, rods, or octapods, demonstrate higher saturation magnetization than spherical NPs of similar volume [134], [135], [136], [137]. For nanoparticles investigated in this thesis, despite the larger volume of Fe_3O_4 in cubic nanoparticles, they demonstrated the opposite effect, i.e. a lower relaxivity value, r_2. Moreover, surprisingly cubic nanoparticles with a thin 2nm shell exhibited significantly lower relaxivity than nanoparticles with a 10 nm shell.

To understand this unusual behaviour of investigated nanoparticles, the magnetic properties of nanoparticles have been taken into consideration. In Figure 61 and Figure 62 magnetometry results for spherical and cubic nanoparticles, respectively, are presented. For uncoated nanoparticles, saturation magnetization at 300 K was 46 emu/g for spherical and 47 emu/g for cubic NPs. The 10 nm SiO_2 shell reduced the magnetization to 15 emu/g for spherical and 9 emu/g for cubic NPs while reducing the shell thickness to 2 nm resulted in an M_S value of 15 emu/g. However, it must be taken into consideration that the net magnetic moment for each sample arises from a different amount of the magnetic component. In other words, the contribution of the magnetic core to the total mass of NPs is different (see Table 17). To reliably compare the effect of the shell on saturation magnetization for each sample, M_S values were recalculated to unit mas of Fe_3O_4 resulting in M_S values: 164.5, 54.0 and 24.6 emu/g for spherical Fe_3O_4@SiO_2(10nm), cubic Fe_3O_4@SiO_2(10nm) and cubic Fe_3O_4@SiO_2(2nm) NPs, respectively. This leads to the following observations. The effect of the 10 nm coating on spherical nanoparticles is less pronounced than what would be explained by the mass difference of Fe_3O_4 in uncoated NPs and coated NPs (obtained 15 emu/g, expected 4.2 emu/g). This effect of the mass

difference of Fe_3O_4 is present in many papers but seems to be unnoticed [138], [139], [140]. For 10 nm coated cubic nanoparticles, M_S is almost the same as described by the mass difference (obtained 9 emu/g vs. calculated 7.8 emu/g). Finally, for 2 nm coating on cubic nanoparticles, the lowering of saturation magnetization is much more pronounced to be explained simply by the Fe_3O_4 mass difference (obtained 15 emu/g, expected 28.7 emu/g).

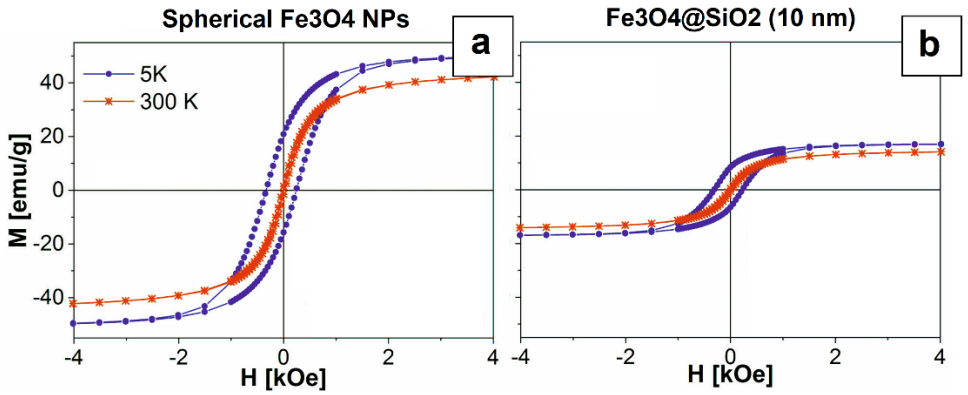

Figure 61 Magnetometry results for spherical NPs, a) spherical Fe_3O_4 NPs, b) spherical Fe_3O_4 NPs with 10 nm SiO_2 shell [115]

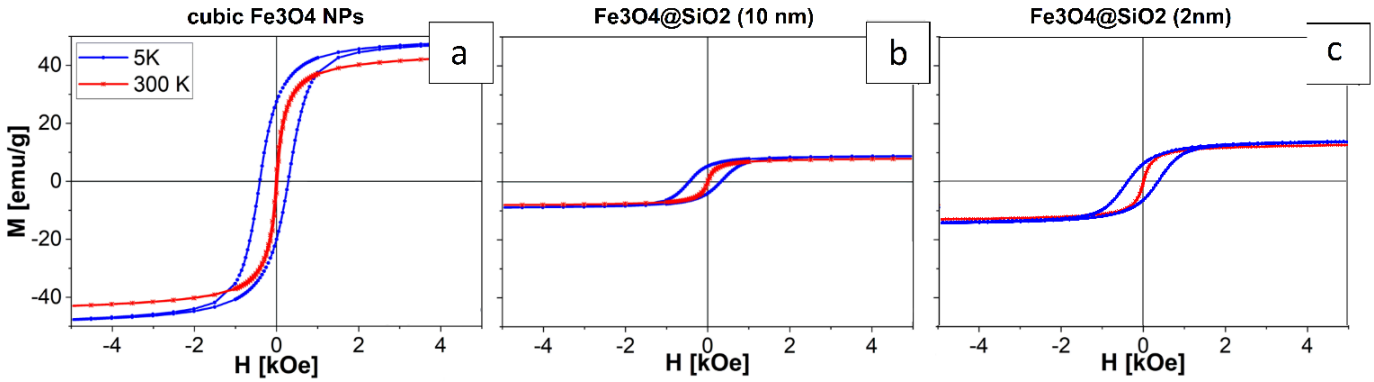

Figure 62 Magnetometry results for cubic Nanoparticles, a) cubic Fe_3O_4 NPs, b) cubic Fe_3O_4 NPs with 10 nm SiO_2 shell, c) cubic Fe_3O_4 NPs with 2 nm SiO_2 shell [115]

Apart from the mass difference, other factors and mechanisms are influencing the magnetization of coated nanoparticles. As part of silica bonds to the surface of magnetite particles through the chemical Fe-O-Si bonds, the magnetic moment of Fe on the surface of magnetite decreases [140]. The SiO_2 coating can also affect the arrangement of surface atoms which results in either increased or decreased spin canting on NPs surface, thus

increasing or reducing magnetization [141]. Finally, Mössbauer spectroscopy revealed that in reality, the magnetic core of investigated NPs doesn't consist only of magnetite, but also, due to partial oxidation of Fe_3O_4 NPs, some amounts of maghemite or wüstite are present, especially in cubic NPs (appendix A) [115]. The quantification of the magnitude of each effect is, in general, a very complex subject and was not in the scope of this work. Nonetheless, the magnetometry and Mössbauer results helped to understand surprising r_2 dependencies.

Regarding the shell thickness, one more effect should be taken into account. Equation 29 states that decreasing the shell layer should result in enhanced r_2 relaxivity. However, increasing the thickness of the SiO_2 shell prevents uncontrolled agglomeration and aggregation of nanoparticles, which has an impact on the diffusion of water molecules near the superparamagnetic cores that is necessary for sufficient enhancement of T_2 relaxation. In the introductory chapter, it was explained that T_2-relaxation is primarily governed by the outer-sphere relaxation theory, i.e. local magnetic flux generated by magnetic nanoparticles influences the dephasing of hydrogen protons diffusing in the vicinity of CAs. Depending on the size of the NPs cluster, r_2 is described by three behavioural regimes based on protons' diffusion, namely the motional averaging regime (MAR), static dephasing regime (SDR), and echo-limited region (ELR) or slow-motion regime (SMR). For individual NPs or small NP clusters with small hydrodynamic sizes, water residency in the secondary sphere is short. This means that molecules rapidly diffusing around NPs experience fast-changing magnetic fields and the relaxation rate is governed by the water molecular motions. As the hydrodynamic size increases, the area influenced by the magnetic inhomogeneity is increased, which results in prolonged water residency and r_2 enhancement. However, by increasing the cluster size beyond a critical value in SDR, the fluctuating magnetic field will no longer be enhanced, and the overall r_2 becomes independent of the hydrodynamic size. Further increasing the dimensions of the clusters or further uncontrolled NPs agglomeration will lead to ELR, where the increase in size affects negatively the r_2 for particles occupying space in the secondary sphere [124], [142], [143]. This effect might further explain the difference in relaxivity values obtained for cubic nanoparticles and can justify choosing a thicker coating layer.

Regarding magnetic resonance contrasting properties, it can be concluded that observed significant differences in saturation magnetization seem to have a predominant

effect as they correlate with the obtained r_2 relaxivity results. Although the size of the spherical Fe_3O_4@SiO_2 was the smallest and the ratio between shell thickness and NPs size was the largest, they demonstrated the highest relaxivity.

In Figure 21, Figure 26, and Figure 31, it is shown that despite the significant differences in r_2 relaxivities, effective contrast can be achieved for all nanoparticles. This is due to the different content of Fe_3O_4 as presented in Figure 63. As the cubic nanoparticles are characterized by higher Fe_3O_4 content, it partially compensates for their lower relaxivities, and for the same concentration of the whole nanocarriers, cubic nanoparticles with a 10 nm shell may produce a slightly higher contrast than spherical NPs. Therefore, from the point of view of MRI, it can be considered that spherical-Fe_3O_4@SiO_2(10nm) and cubic-Fe_3O_4@SiO_4(10nm) nanoparticles will exert a very similar effect on images.

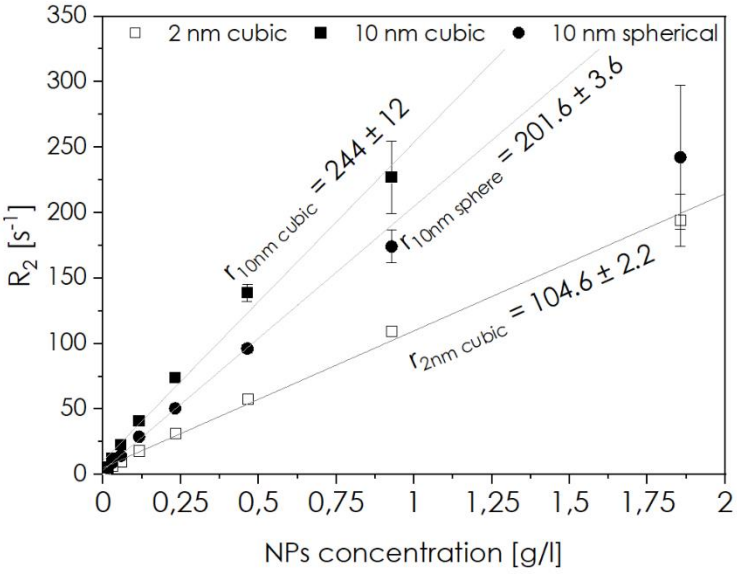

Figure 63 Relaxation rates dependence on the concentration of the whole Fe_3O_4@SiO_2 NPs

For all nanoparticles, the optimal imaging parameters were found by the investigation of contrast dependence on applied echo time for samples in the lower concentration range that is more likely to be achieved in-vivo (Figure 23, Figure 28, Figure 33). To ensure that the contrast arises from T_2 differences, a long TR of 6000 ms was applied. For regions with the largest difference in Fe_3O_4 concentration, the maximum contrast is achieved for a relatively short echo time of 60 ms for NPs with a 10 nm shell,

while a much longer TE of 200 ms is required for NPs with a 2 nm SiO_2 layer. As the difference in concentration of nanocarriers and, consequently, T_2 relaxation times difference between samples gets smaller, higher echo times of up to 135 ms for spherical-Fe_3O_4@SiO_2(10nm), 120 ms for cubic-Fe_3O_4@SiO_2(10nm), and 300 ms for cubic-Fe_3O_4@SiO_2(2nm) are required to achieve sufficient contrast.

The therapeutic effects and toxicity of cubic and spherical nanoparticles with 10 nm SiO_2 shell were investigated after further functionalization of their surface with small gold nanoparticles that serve as photosensitizers. Additionally, the concept of combined chemo-photothermal therapy was tested for spherical nanoparticles by the attachment of cisplatin, a cytostatic chemotherapy medication used to treat a number of cancers. The effect was studied in terms of cell viability (MTT assay) on two colon cell lines: SW480 and SW620. Regarding the toxicity of Fe_3O_4@SiO_2-Au NPs, the viability test showed that they cause 13% to 18% mortality depending on particle shape and cell line. Consequently, the investigated nanoparticles are characterized by a low cytotoxic effect. Cells cultured with non-functionalized Fe_3O_4@SiO_2@Au NPs and irradiated by laser demonstrated very high mortality compared with non-irradiated NPs. For cubic nanoparticles, an increase in the cells mortality to around 50-55% for SW480 cells and 35% - 40% for SW620 cells was observed. For spherical NPs irradiated with a laser this mortality was slightly lower, 40 -45% and 30 – 35% for SW480 and SW610 cell lines, respectively. However, for those NPs the combination of photothermal therapy and chemotherapy was investigated causing ~50 % and ~43 % mortality of the SW480 and SW620 cells in the case of laser irradiation of Fe3O4@SiO2-Au-cPt NPs [115].

5.2. Theranostic nanocarriers with direct-detection agents based on ^{19}F nuclei

Both investigated nanocarriers with fluorine atoms were in the form of polyelectrolyte nanocapsules where the liquid core consisting of the anticancer drug is surrounded by a multilayer shell of opposingly charged polymer layers. In one composition, fluorine is embedded in the polymeric shell in the form of Nafion™ polymer as a ^{19}F detectable agent and a drug (paclitaxel) is encapsulated in the core, while in the

other composition, the drug itself (5-fluorouracil) contains ^{19}F atoms, which allows for its detection via ^{19}F MRI.

There are several properties that a polymer probe should possess for the application in ^{19}F MRI. Most importantly, the content of equivalent fluorine atoms in the particle has to be high to ensure sufficient SNR for ^{19}F imaging. It should also have adequate solubility in water and mobility, as well as an easily modifiable surface for effective accumulation at the desired site. Regarding safety and therapeutic efficiency, requirements for reliable biodegradability and elimination from the system have to be fulfilled [144]. The surface of both the analysed nanocarriers was covered with a PGA-g-PED layer that limits their toxicity. It was shown before that empty pegylated polyelectrolyte nanocapsules do not show any deleterious effects on mammalian cells in culture, while the cytotoxic effect of the encapsulated drug was preserved [145].

Regarding MR properties, both probes introduce some challenges. Nafion™ (N-(3-acetylphenyl)-4-(2-phenylethyl)thieno[3,2-b]pyrrole-5-carboxamide) is a polymer with relatively high fluorine content per molecule ($C_7HF_{13}O_5S \cdot C_2F_4$). However, those nuclei are not MR equivalent and 5 peaks are observed in the ^{19}F MR spectrum, resulting in limited signal available for ^{19}F imaging. In all experiments with Nafion™, only the resonance that was well separated from others was used, which corresponds to only about 30% of the entire signal. Additionally, peaks observed in the Nafion™ spectrum are significantly broadened, which indicates that the T_2 relaxation time is very short. This severely restricts the range of available imaging sequences to Ultrashort Echo Time (UTE), its 3D implementation (UTE3D), and Zero Echo Time (ZTE). The ^{19}F spectrum of 5-FU (5-fluoro-1*H*-pyrimidine-2,4-dione) is characterized by a single sharp peak, which is preferable for imaging. On the other hand, the 5-FU molecule ($C_4H_3FN_2O_2$) consists of only one ^{19}F atom, which affects the maximum achievable SNR for acceptable concentrations. Consequently, for both ^{19}F compounds, the number of ^{19}F nuclei contributing to the image was much lower than for the most frequently used tracers based on perfluorocarbons. To visualize ^{19}F tracers with less preferable characteristics, the choice of an adequate sequence and the optimization of its parameters is are utmost importance.

Both the applied imaging sequences (FLASH for 5-FU imaging and UTE 3D for Nafion™) belong to a family of spoiled gradient echo (SPGR) methods. Signal intensity for SPGRs is described by the steady-state equation [146]:

$$S = A\sin(\alpha)\cdot\frac{1-e^{\left(-\frac{TR}{T1}\right)}}{1-\cos(\alpha)\cdot e^{\left(-\frac{TR}{T1}\right)}}\cdot e^{\left(-\frac{TE}{T2^*}\right)}, \quad (35)$$

with α – flip angle and A -global sensitivity factor. The dependence of flip angle on normalized signal intensity (S/A) is plotted in Figure 64.

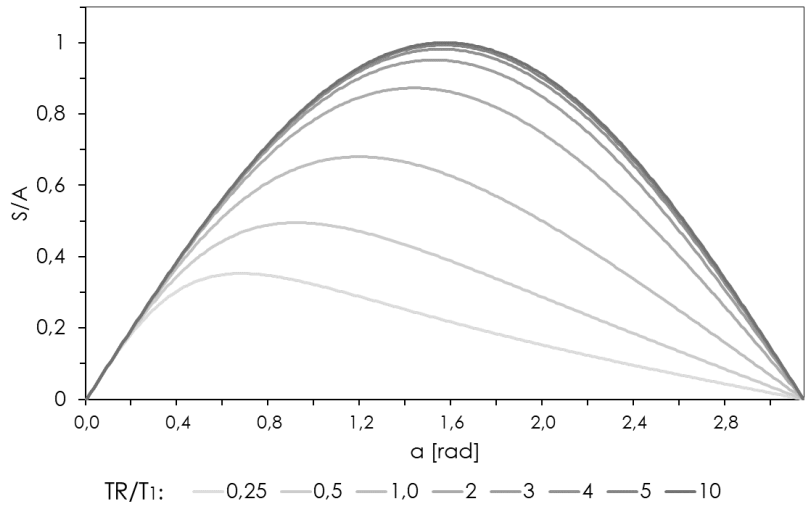

Figure 64 S/A vs flip angle (α) dependence

As it's shown in the figure above, for each value of TR/T_1, there is an optimal angle (Ernst angle) that maximizes the achievable signal intensity, while angles that are either smaller or larger can significantly reduce it. Ernst angle can be calculated from the formula $\alpha_E = arcos\left(-\frac{TR}{T1}\right)$ or $\alpha_{ET2} = \sqrt{{\alpha_E}^2 - \left(\frac{T_{rf}}{2\cdot T2}\right)^2}$, which takes into account relaxation during RF pulse excitation [147]. For imaging of 5-fluorouracil nanocarriers, the theoretically calculated 10.1° angle was applied, whereas for Nafion™ NCs, a 6.4° angle instead of theoretical 7.5° was used as it gave a higher signal. This can be caused by the more rapid relaxation of the Nafion™ when embeamed in NCs shell, or by the uncertainty of calibration of the flip angle for the x-nucleus with a very low signal from Nafion™.

Additionally, as there is no background ^{19}F signal within the body, contrasting efficiency for ^{19}F MRI contrast agents is assessed in terms of the ratio between the signal produced by the probe and the noise. Therefore, the SNR enhancement is the main objective in ^{19}F imaging of ^{19}F labelled nanocarriers. The signal-to-noise ratio in MR imaging depends on a number of factors [148] [149]:

$$SNR \propto I \cdot f(B_0) \cdot f(QF) \cdot V_{voxel} \cdot \frac{\sqrt{Ny}}{\sqrt{BW}} \cdot \sqrt{NA}, \qquad (36)$$

where:

I – intrinsic signal intensity for applied sequence, that is based on T_1, T_2, and spin density.

$V_{voxel} = slice\ thickness \cdot \frac{FOV_x}{N_x} \cdot \frac{FOV_y}{N_y}$ – voxel size; SNR is linearly proportional to the volume of the voxel ;

NA – number of acquisitions; Signal averaging is achieved by averaging sets of data that were acquired with the same sequence parameters. SNR is proportional to the square root of NA, while acquisition time scales linearly with SNR. Therefore, in order to increase the SNR two times, total acquisition time has to be doubled [150];

BW – RF bandwidth; narrow spread of frequencies around basic frequency result in higher $SNR \propto \frac{\sqrt{Ny}}{\sqrt{BW}}$, but at the same it requires a longer time for sampling, resulting in longer minimum TE possible for imaging [151]. Therefore for most ^{19}F compounds excitation with rather wide BW is necessary;

$f(B_0)$ – function of B_0 field induction; Higher fields incuse larger spins polarization, resulting in larger SNR by a factor ${B_0}^{1.0} - {B_0}^{1.75}$ [152];

$f(QF)$ – function of the coil quality factor, which is the indicator of RF coil sensitivity to signals arising from the object. SNR is reduced by the 'loading' effect and eddy currents. Eddy currents are produced by the changing magnetic field in the direction perpendicular to this field, and they cause artifacts and SNR decrease, especially in fast imaging sequences [153] [154]. The loading effect relates to SNR losses caused by the electric impedance of the object, which causes the variation of the magnetic field due to susceptibility effects. This effect is different for each object. Therefore, to minimize it, tuning of the RF coil is performed before image acquisition.

Several strategies for increasing the SNR were applied to ensure optimal detection of ^{19}F probes via ^{19}F MRI. All measurements were performed using a high-field 9.4 T MRI scanner, which provides 3 to around 6 times higher than most clinical scanners (3 T). Regarding the coil quality, the small in-house built ribbon coil that can be tuned either to ^{1}H or ^{19}F resonance frequency, with a size optimised for imaging of small samples, was used. The performance in terms of signal-to-noise enhancement for this simple solenoid coil was compared with the commercially available Bruker $^{1}H/^{19}F$ volume coil with an inner diameter of 40 mm, designed as two geometrically decoupled linear resonators for ^{1}H and ^{19}F-nucleus. In Figure 65, the comparison of two images of the same phantom with 5-fluorouracil. The image on the left was acquired with a commercial Bruker coil, and the image on the right with the coil was optimised for small samples. Both images were acquired with FLASH sequence with the same geometry, i.e. slice thickness = 4 mm, FOV = 40 x 40 x 40 mm, MTX = 32 x 32 x 32, and with the same TR = 100 ms, TE = 3.1 ms and FA = 15°. For an image on the right, 1024 averages were used, resulting in a total acquisition time of almost 55 min, while for an image on the left, the number of averages was extended o 2048 (acquisition time = 1h 49 min) for more accurate SNR measurement. SNR was calculated as the mean signal intensity in the region of interest placed within the sample and the average noise from three regions selected outside the sample was 5, and 14 for the image on the left and the right, respectively. SNR on the image recalculated for the same number of averages (2048) was 20, demonstrating a fourfold increase in achievable SNR by the coil selection.

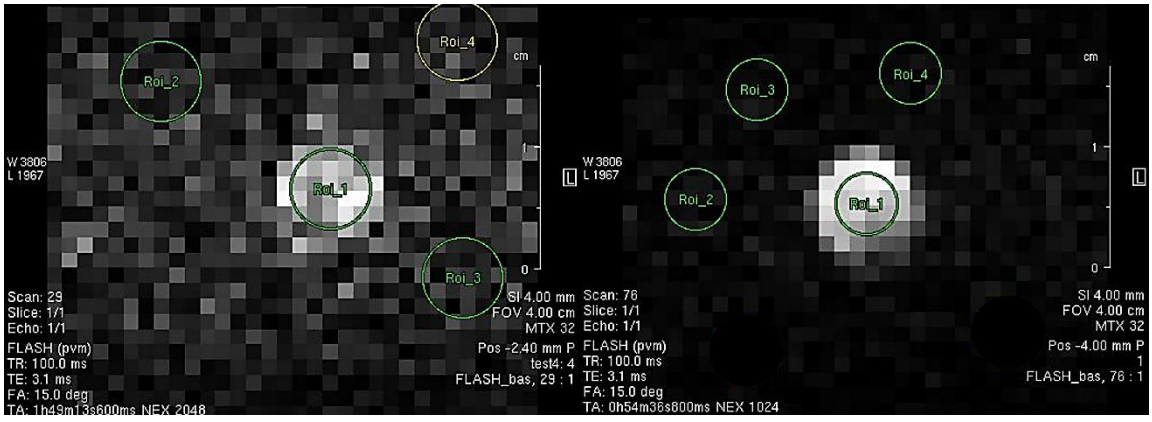

Figure 65 SNR comparison for images obtained with Bruker $^{1}H/^{19}F$ volume (left) and small ribbon coil for small samples (right)

MR image quality is an interplay between three parameters: scan time, spatial resolution, and SNR. To increase the SNR, a compromise between two other parameters has to be made. In most cases, scan time has to be limited to be tolerable for the animal under anesthesia and reasonable in terms of resources used for the experiment. To achieve that, the spatial resolution has to be lowered to a range that allows resolving important features but doesn't compromise the SNR. For fluorine imaging, even with lower resolution, a reliable assessment of the tracer distribution can be achieved due to zero background signal. For both types of nanocarriers, ^{1}H images were recorded with a high resolution of 0.3 mm isotropic for Nafion™ nanocapsules and 0.3 mm in-plane with 1 mm slice thickness for 5-FU nanocarriers, while ^{19}F imaging was performed with larger voxels. For Nafion™ NCs, 1.25 mm isotropic voxel was used, while for 5-FU NCs two different in-plane resolutions were tested: 0.63 x 0.63 mm and 1.25 x 1.25 mm (slice thickness of 4 nm). For the SNR dependence on the number of acquisitions, the $SNR \sim a \cdot \sqrt{NA}$ function was fitted, which accounts for $SNR \sim V_{voxel} \cdot \frac{\sqrt{Ny}}{\sqrt{BW}} \cdot \sqrt{NA}$ contribution, according to equation 36. The ratio of fitted 'a' coefficients was 2.79, which is very close to the theoretical 2.82 (BW = 10 kHz, Ny = 32 or 64). Therefore, by lowering the spatial resolution, almost three times higher SNR was achieved.

Another strategy for SNR enhancement is increasing the number of averages (NA). In MR imaging, higher SNR values are obtained by averaging the signal, i.e. by repeating acquisition with the same parameters multiple times and summing the results pixel-wise. Due to the statistical fluctuation nature of the noise, its resultant value gets suppressed while the signal arising from the object is increased, which results in a net SNR enhancement proportional to $\sqrt{NA}$. As the total scan time scales linearly with NA, the number used in the experiments was selected as a compromise between achievable SNR and an acquisition time that should be kept in a reasonable range.

For both types of nanocarriers, it was shown that within 30 minutes of total scan time it is possible to visualize their distribution. For 5-FU samples, the highest applied NA of 1024 resulted in an acquisition time of 27 min and 18 s and a high SNR of 32.5 for imaging of a single 4 nm slice and 1.25 x 1.25 mm in-plane resolution. For Nafion™ samples, imaging with 64 averages and a total acquisition time of 27 min was assessed to produce SNR = 3. Furthermore, due to radial k-space sampling, the whole volume of 4.0

x 4.0 x 4.0 cm is covered with 1.25 mm isotropic voxels. This result can be treated as a proof of concept of utilizing ^{19}F MRI for Nafion™ and 5-FU nanocarriers detection and constitutes the first step of investigations for biomedical application which is mandatory for the planning of any in vitro and in vivo studies. Additionally, for 5-FU nanocapsules, the toxicity was tested in terms of the viability of murine cancer cells (4T1 and CT26-CEA lines) that were incubated with either empty capsules, or with free or encapsulated 5-fluorouracil. Results showed that empty AOT/PLL nanocores demonstrate significant toxicity (around 40% viability for both cell lines), which is greatly reduced (90% viability) for the pegylated multi-layered structure. At the same time, 5-FU loaded nanocarriers demonstrated similar toxicity to free fluorouracil, causing 25% (vs. 30% for free 5-FU) viability for the 4T1 line, and around 40% for both encapsulated and free 5-FU for CT26-CEA cells [114]. Nanocarriers for 5-fluorouracil delivery have been extensively studied resulting in many different formulations including solid lipid nanoparticles [155], polymeric nanocarriers [156] [157], nanoliposomes [158], core-shell NPs [159] [160], quantum dot-based nanocarriers [161] and dendrimers [162] [163], however only in few papers application of ^{19}F MRS for NCs detection can be found [164] [165], while ^{19}F MRI has not been considered in any of them. Nevertheless, results obtained for 5-FU solution for injections indicate that it is possible to obtain quantitative results of 5-FU distribution in vivo. Successful in-vivo detection of localized ^{19}F signal has been reported not only for 5-FU but also for its metabolites. After the injection of 5 FU at a dose of 455 - 550 mg/kg at 3.0 T field [166], 250 mg/kg at 7.0 T field [167], and 130–260 mg/kg at 9.4 T field [168], the ^{19}F signal was successfully spatially resolved. As the SNR scales linearly with the ^{19}F dose, we expect that imaging with the dose in a range of 100 – 300 mg/kg, that was previously used in animal studies on small rodents would still produce sufficient SNR (SNR of 3 - 10) to evaluate the 5-FU nanocarriers distribution within a 30 minutes time frame.

For Nafion™ nanocarriers, cytotoxicity has not been tested yet. However, biocompatibility studies of Nafion™ have shown no acute or chronic foreign body response. Moreover, it is characterized by thermal stability up to 200 °C, and chemical and biological inertness [169]. Nafion™ was originally created as an electrolyte material for proton exchange membrane fuel cells, so only a few papers describe its biomedical applications. These include insulin pH-controlled delivery LbL films [170], hybrid

biosensors for dopamine [171] and glucose [172], films with antibiotic-loaded mesoporous silica nanoparticles where Nafion™ was used as a protective layer [173] and multilayer UV triggered microcapsules [174]. To my best knowledge, it is the first attempt to visualize Nafion™- containing nanoparticular systems via ^{19}F MRI.

Chapter 6

Conclusions

This thesis aimed to evaluate the theranostic potential of various nanocarriers in terms of their contrasting efficiency for magnetic resonance imaging. The nanocarriers that contained standard and relaxation contrast agents, as well as direct-detection CAs based on ^{19}F nuclei, were investigated.

Relaxation contrast agents were embedded in nanocapsules for drug delivery and the core-shell nanoparticles for photothermal therapy. For nanocapsules with multilayer shells with F_3O_4 nanoparticles, very high relaxivities ($r_2 > 235\ mM^{-1}s^{-1}$) were obtained for both proposed formulations. The hypothesis that the additional AOT polymer layer which stabilizes the cargo does not influence the contrasting properties of the whole NCs was confirmed. Because the additional layer did not have direct contact with Fe_3O_4 nanoparticles and did not limit water diffusion near superparamagnetic centers, which is required for efficient T_2 shortening of the environment, the difference in r_2 relaxivities, which was less than 10 percent, can be explained by statistical differences in T_2 values between the measured series. For the core-shell nanocarriers, where Fe_3O_4 constituted the core of NCs, which was covered with a SiO_2 shell and decorated with small Au NPs, surprising results were obtained. In this case, three different compositions of NCs were tested: with a spherical core and a 10 nm shell, with a cubic core and a 10 nm shell, and with a cubic core and a 2 nm shell. It was expected that nanocarriers with a cubic core would cause more effective relaxation due to their shape and larger volume compared to spherical NPs. Moreover, it was assumed that the relaxivity of nanocarriers would decrease with increased SiO_2 shell thickness. However, the opposite results were obtained. To understand the relationship between the obtained relaxivities and the composition of NCs, the Mössbauer spectroscopy, and SQUID magnetometry results were used. Regarding magnetic resonance contrasting properties, it appears that observed considerable changes in saturation magnetization have a predominant influence since they coincide with r_2 relaxivity results. Even though the spherical NPs had the smallest dimensions and the ratio between shell thickness and NPs size was the largest, they

induced the highest relaxation. Nevertheless, it was demonstrated that despite the significant differences in r_2 relaxivities, effective contrasting can be achieved for all nanoparticle geometries. As the cubic nanoparticles are characterized by higher Fe_3O_4 content, it compensates to some extent for their lower relaxivities, and for the same concentration of the whole nanocarriers, cubic nanoparticles with a 10 nm shell induce slightly higher contrast than their spherical equivalents. Moreover, for both types of nanocarriers (nanocapsules and core-shell nanocarriers) the analysis of contrast allowed the determination of optimal echo time values for the effective visualization of samples. Additionally, results of relaxivities were compared with similar compositions of nanocarriers and with clinically approved contrast agents. For all proposed NPs, except for core-shell NPs with a 2 nm shell, relaxivities were at least as high as those of Resovist™ or Feridex™. With the anticipated more preferable distribution of theranostic nanocarriers compared to the standard contrast agents, namely high accumulation in tumour sites, it is expected that in-vivo MR imaging would enable the therapeutics tracking due to very high contrast enhancement. Because the negative-contrast MRI does not allow the detection of the Fe_3O_4-labelled nanocarriers when artifacts induced by pathological events (like bleeding or calcifications) are present, the positive contrast agents were also investigated. Results regarding MR relaxometry and imaging of Gd-labelled nanocapsules revealed slightly different values of longitudinal relaxivity r_1: 9.97 and 8.11 $m^{-1}Ms^{-1}$ for nanoemulsion and polymeric cores, respectively. Nevertheless, for very low concentrations of Gd, which are generally more probable to be achieved in-vivo, the values of relaxation rates were almost identical. Notably, the r_1 values obtained for both types of NCs were around two times higher than those of clinically approved CAs: Magnevist™, Dotarem™, and Gadovist™, which indicates that Gd-labelled NCs would produce high contrast in T_1-weighted images. This was confirmed by acquiring the images with short repetition and echo times, where regions with different concentrations of Gd could be distinguished.

Unlike typical relaxation contrast agents, ^{19}F-containing compounds do not cause substantial changes in the medium's T_1 and T_2 relaxation times in the accumulation area. For those hot-spot agents, which are based on nuclei other than ^1H that also undergo nuclear magnetic resonance (so-called x-nuclei), the contrasting effect is accomplished by imposing the MR image of the spatial distribution of x-nuclei over the proton image. The

biggest challenge in the detection of ^{19}F-containing theranostic nanocarriers was, therefore, a low signal-to-noise ratio. This was due to the fact that the signal from ^{19}F compounds is usually only a little above detection limits. Thus, the main objective of ^{19}F imaging experiments was to optimise the imaging conditions to reliably determine the spatial distribution of ^{19}F-containing agents. Several strategies for increasing the SNR were implemented to ensure optimal detection of ^{19}F probes via ^{19}F MRI. Firstly, all measurements were performed using a high-field 9.4 T MRI scanner, which provides 3 to around 6 times higher signal than most clinical scanners. Regarding the coil quality, the small in-house built ribbon coil that can be tuned either to ^{1}H or ^{19}F resonance frequency, with a size optimised for imaging of small samples, was used, resulting in a fourfold increase of achievable SNR only by the coil selection. As the image quality is an interplay between the total scan time, spatial resolution, and SNR, to maximise the SNR, at least one of the two other factors has to be limited. Because the total scan time has to be kept within a reasonable range, the spatial resolution has to be lowered to a value that ensures sufficient SNR but at the same time allows resolving important features. In the case of ^{19}F imaging, a reliable assessment of the tracer distribution can be achieved even with lower resolution due to the close to zero endogenous ^{19}F MR signal. Another strategy for increasing the SNR is repeating the acquisition with the same parameters multiple times and summing the results pixel-wise. Such a procedure leads to signal amplification and noise suppression due to its statistical distribution. The net SNR enhancement is proportional to $\sqrt{NA}$. However, as the total scan time scales linearly with NA, the number of averages used in the experiments was selected as a compromise between achievable SNR and acquisition time. For both types of investigated ^{19}F nanocarriers, namely nanocapsules with Nafion™ polymer embedded in the multilayer shell, and polyelectrolyte nanocapsules with 5-fluorouracil, it was shown that undertaken steps for ^{19}F MRI optimisation led to their successful detection within 30 minutes of the total scan time. For 5-FU nanocarriers, a single-slice image with a high SNR of 32.5 was achieved within the acquisition time of about 27 min, while for Nafion™ nanocapsules, applying the same acquisition time resulted in an SNR of 3. However, here the whole volume of the sample was covered. As there are only a few similar works present in the literature, and those that exist focus on MR spectroscopy (or localized spectroscopy), rather than on MR imaging, the comparison of obtained results was difficult. Nevertheless, taking into

consideration obtained values of SNR it can be presumed that in-vivo observations of NCs distribution will also be possible.

To further conclude, it was shown that all investigated theranostic nanocarriers produce sufficient contrast for their detection via MR imaging. In the case of relaxation contrast agents, contrasting properties were evaluated by the measurements of the specific relaxivities, r_1 and r_2, and the contrast assessment in MR images. The obtained results are very promising, as the r_1 or r_2 values for almost all proposed compositions were higher than those of clinically approved CAs. For fluorine-containing probes, the contrast was assessed by the SNR analysis, and the obtained results suggest, especially for 5-FU NCs, the potential for in-vivo detection at the therapeutic dose. Therefore, the aim of the thesis was accomplished.

References

[1] WHO, "The top 10 causes of death," World Health Organization, 09 December 2020. [Online]. Available: https://www.who.int/news-room/fact-sheets/detail/the-top-10-causes-of-death.

[2] P. N. Navya, A. Kaphle, S. P. Srinivas, S. K. Bhargava, V. M. Rotello and H. K. Daima, "Current trends and challenges in cancer management and therapy using designer nanomaterials," *Nano convergence,* vol. 6, no. 1, 15 July 2019.

[3] S. Rani and U. Gupta, "HPMA-based polymeric conjugates in anticancer therapeutics," *Drug discovery today,* vol. 25, no. 6, June 2020.

[4] B. Brito, J. Gallo, T. W. Price, M. Bañobre-López and G. J. Stasiuk, "Smart magnetic resonance imaging-based theranostics for cancer," *Theranostics,* pp. 8706-8737, 07 August 2021.

[5] A. Tareq, R. Shiva, S. Nayer and D. E. Allan, "MRI-traceable theranostic nanoparticles for targeted cancer treatment," *Theranostics,* vol. 11, no. 2, pp. 579-610, 01 January 2021.

[6] J. Funkhouser, "Current Drug Discovery," pp. 17-19, 01 August 2002.

[7] A. G. Robertsona and L. M. Rendina, "Gadolinium theranostics for the diagnosis," *Chemical Society Reviews,* pp. 4231-4244, 18 February 2021.

[8] C.-T. Yang, K. K. Ghosh, P. Padmanabhan, O. Langer, J. Liu, D. N. C. Eng, C. Halldin and B. Gulyás, "PET-MR and SPECT-MR multimodality probes: Development and challenges," *Theranostics,* vol. 8, no. 22, pp. 6210-6232, 2018.

[9] F.-M. Lu and Z. Yuan, "PET/SPECT molecular imaging in clinical neuroscience: recent advances in the investigation of CNS diseases.," *Quantitative imaging in medicine and surgery,* p. 433–447, 01 June 2015.

[10] H. Lusic and M. W. Grinstaff, "X-ray-Computed Tomography Contrast Agents," *Chemical Reviews,* pp. 1641-1666, 05 December 2012.

[11] Y. Liu, K. Ai and L. Lu, "Nanoparticulate X-ray Computed Tomography Contrast Agents: From Design Validation to in Vivo Applications," *Accounts of Chemical Research,* pp. 1817-1827, 05 September 2012.

[12] A. Dauba, A. Delalande, H. A. S. Kamimura, A. Conti, B. Larrat, N. Tsapis and A. Novell, "Recent Advances on Ultrasound Contrast Agents for Blood-Brain Barrier Opening with Focused Ultrasound," *Pharmaceutics,* vol. 12, no. 11, 21 November 2020.

[13] M. Versluis, E. Stride, G. Lajoinie, B. Dollet and T. Segers, "Ultrasound Contrast Agent Modeling: A Review," *Ultrasound in Medicine & Biology,* vol. 46, no. 9, pp. 2117-2144, 01 September 2020.

[14] Y. Jeong, H. S. Hwang and K. Na, "Theranostics and contrast agents for magnetic resonance imaging," *Biomaterials Research,* vol. 22, no. 20, 27 July 2018.

[15] L. P. Ganipineni, B. Ucakar, N. Joudiou, J. Bianco, P. Danhier, M. Zhao, C. Bastiancich, B. Gallez, F. Danhier and V. Préat, "Magnetic targeting of paclitaxel-loaded poly(lactic-co-glycolic acid)-based

nanoparticles for the treatment of glioblastoma," *International journal of nanomedicine,* vol. 13, pp. 4509-4521, 08 August 2018.

[16] C.-H. Fan, Y.-H. Cheng, C.-Y. Ting, Y.-J. Ho, P.-H. Hsu, H.-L. Liu and C.-K. Yeh, "Ultrasound/Magnetic Targeting with SPIO-DOX-Microbubble Complex for Image-Guided Drug Delivery in Brain Tumors," *Theranostics,* vol. 6, no. 10, pp. 1542-1556, 2016.

[17] A. Shakeri-Zadeh, M.-B. Shiran, S. Khoee, A. M. Sharifi, H. Ghaznavi and S. Khoei, "A new magnetic nanocapsule containing 5-fluorouracil: in vivo drug release, anti-tumor, and pro-apoptotic effects on CT26 cells allograft model," *Journal of biomaterials applications,* vol. 29, no. 4, pp. 548 - 556, October 2014.

[18] S.-T. Feng, J. Li, Y. Luo, T. Yin, H. Cai, Y. Wang, Z. Dong, X. Shuai and Z.-P. Li, "pH-Sensitive Nanomicelles for Controlled and Efficient Drug Delivery to Human Colorectal Carcinoma LoVo Cells," *PLOS ONE,* vol. 9, no. 6, 25 June 2014.

[19] D. Ling, H. Li, W. Xi, Z. Wang, A. Bednarkiewicz, S. T. Dibaba, L. Shi and L. Sun, "Heterodimers made of metal–organic frameworks and upconversion nanoparticles for bioimaging and pH-responsive dual-drug delivery," *Journal of Materials Chemistry B,* vol. 8, pp. 1316-1325 , 03 January 2020.

[20] Y. Liu, . L. Feng, T. Liu, L. Zhang, Y. Yao, D. Yu, L. Wang and N. Zhang, "Multifunctional pH-sensitive polymeric nanoparticles for theranostics evaluated experimentally in cancer," *NAnoscale,* vol. 6, pp. 3231-3242, 03 January 2014.

[21] T. Boissenot, E. Fattal, A. Bordat, S. Houvenagel, J. Valette, H. Chacun, C. Gueutin and N. Tsapis, "Paclitaxel-loaded PEGylated nanocapsules of perfluorooctyl bromide as theranostic agents," *European Journal of Pharmaceutics and Biopharmaceutics,* vol. 108, pp. 136 - 144, 01 November 2016.

[22] B. Shaowei, Y. Yaping, C. Yongping, Y. Zhigang, C. Shizhen, Z. Xin and J. Zhong-Xing, "In vivo drug tracking with 19F MRI at therapeutic dose," *Chemical Communications,* pp. 3875-3878, 29 March 2018.

[23] J. Zhu, H. Zhang, K. Chen, Y. Li, Z. Yang, S. Chen, X. Zheng, X. Zhou and Z.-X. Jiang, "Peptidic Monodisperse PEG "Comb" as Multifunctional "Add-On" Module for Imaging-Traceable and Thermo-Responsive Theranostics," *Advanced Healthcare Materials,* vol. 9, no. 3, 01 February 2020.

[24] X. Liu, Y. Zhang, Y. Wang, W. Zhu, G. Li, X. Ma, Y. Zhang, S. Chen, S. Tiwari, K. Shi, S. Zhang, H. M. Fan, Y. X. Zhao and X.-J. Liang, "Comprehensive understanding of magnetic hyperthermia for improving antitumor therapeutic efficacy," *Theranostics,* vol. 10, no. 8, pp. 3793 - 3815, 2020.

[25] K. Hayashi, M. Nakamura, W. Sakamoto, T. Yogo, H. Miki, S. Ozaki, M. Abe, T. Matsumoto and K. Ishimura, "Superparamagnetic Nanoparticle Clusters for Cancer Theranostics Combining Magnetic Resonance Imaging and Hyperthermia Treatment," *Theranostics,* vol. 3, no. 6, pp. 366 -376, 2013.

[26] M. Soleymani, S. Khalighfard, S. Khodayari, H. Khodayari, M. R. Kalhori, M. R. Hadjighassem, Z. Shaterabadi and A. M. Alizadeh, "Effects of multiple injections on the efficacy and cytotoxicity of folate-targeted magnetite nanoparticles as theranostic agents for MRI detection and magnetic hyperthermia therapy of tumor cells," *Scientific Reports,* vol. 10, no. 1, p. 1695, 03 February 2020.

[27] S. Fernandes, T. Fernandez, S. Metze, P. B. Balakrishnan, B. T. Mai, J. Conteh, C. De Mei, A. Turdo, S. Di Franco, G. Stassi, M. Todaro and T. Pellegrino, "Magnetic Nanoparticle-Based Hyperthermia Mediates

Drug Delivery and Impairs the Tumorigenic Capacity of Quiescent Colorectal Cancer Stem Cells," *ACS Applied Materials & Interfaces,* vol. 13, no. 14, pp. 15959 - 15972, 14 April 2021.

[28] K. Hayashi, M. Nakamura, H. Miki, S. Ozaki, M. Abe, T. Matsumoto, W. Sakamoto, T. Yogo and K. Ishimura, "Magnetically Responsive Smart Nanoparticles for Cancer Treatment with a Combination of Magnetic Hyperthermia and Remote-Control Drug Release," *Theranostics,* vol. 4, no. 8, pp. 834 - 844, 07 June 2014.

[29] S. Liu, D. Shi, L. Chen, Y. Yan, X. Wang, Y. Song, S. Pu, Y. Liang, Y. Zhao, Y. Zhang and J. Xie, "Paclitaxel-loaded magnetic nanocrystals for tumor neovascular-targeted theranostics: an amplifying synergistic therapy combining magnetic hyperthermia with chemotherapy," *Nanoscale,* vol. 13, no. 6, pp. 3613 - 3626, 07 January 2021.

[30] M. Yusefi, K. Shameli, Z. Hedayatnasab, S.-Y. Teow, U. N. Ismail, C. A. Azlan and R. Rasit Ali, "Green synthesis of Fe3O4 nanoparticles for hyperthermia, magnetic resonance imaging and 5-fluorouracil carrier in potential colorectal cancer treatment," *Research on Chemical Intermediates,* vol. 47, no. 5, pp. 1789 - 1808, 01 May 2021.

[31] Z. Abed, J. Beik, S. Laurent, N. Eslahi, T. Khani, E. S. Davani, H. Ghaznavi and A. Shakeri-Zadeh, "Iron oxide-gold core-shell nano-theranostic for magnetically targeted photothermal therapy under magnetic resonance imaging guidance," *Journal of cancer research and clinical oncology,* vol. 145, no. 5, pp. 1213-1219, 07 May 2019.

[32] N. Eyvazzadeh, A. Shakeri-Zadeh, R. Fekrazad, E. Amini, H. Ghaznavi and S. Kamran Kamrava, "Gold-coated magnetic nanoparticle as a nanotheranostic agent for magnetic resonance imaging and photothermal therapy of cancer," *Lasers in medical science,* vol. 32, no. 7, pp. 1469-1477, September 2017.

[33] M.-F. Tsai, C. Hsu, C.-S. Yeh, Y.-J. Hsiao, C.-H. Su and L.-F. Wang, "Tuning the Distance of Rattle-Shaped IONP@Shell-in-Shell Nanoparticles for Magnetically-Targeted Photothermal Therapy in the Second Near-Infrared Window," *ACS applied materials & interfaces,* vol. 10, no. 2, pp. 1508-1519, 17 January 2018.

[34] X. Hou, X. Wang, R. Liu, H. Zhang, X. Liu and Y. Zhang, "Facile synthesis of multifunctional Fe3O4@SiO2@Au magneto-plasmonic nanoparticles for MR/CT dual imaging and photothermal therapy," *RSC Advances,* vol. 7, no. 31, pp. 18844 -18850, 29 March 2017.

[35] Q. Feng, Y. Zhang, W. Zhang, Y. Hao, W. Yongchao, H. Zhang, L. Hou and Z. Zhang, "Programmed near-infrared light-responsive drug delivery system for combined magnetic tumor-targeting magnetic resonance imaging and chemo-phototherapy," *Acta Biomaterialia,* vol. 49, pp. 402 - 413, 01 February 2017.

[36] Z.-P. Liang and P. C. Lauterbur, Principles of Magnetic Resonance Imaging: A Signal Processing Perspective, New York: The Institute of Electrical and Electronics Engineers, Inc., 1999.

[37] J. Keeler, "Energy levels and NMR spectra," in *Understanding NMR Spectroscopy*, John Wiley & Sons, 2010.

[38] L. G. Hanson, "Is Quantum Mechanics necessary for understanding Magnetic Resonance?," *Concepts in Magnetic Resonance Part A,* vol. 32A, no. 5, pp. 329-340, September 2008.

[39] F. Bloch, "Nuclear Induction," *Physical Review,* vol. 70, pp. 460-474, 01 October 1946.

[40] M. Goldman, "Formal Theory of Spin–Lattice Relaxation," *Journal of Magnetic Resonance,* vol. 149, no. 2, pp. 160-187, April 2001.

[41] M. A. Bernstein, K. F. King and X. J. Zhou, "INTRODUCTION TO DATA ACQUISITION, K-SPACE SAMPLING, AND IMAGE RECONSTRUCTION," in *Handbook of MRI Pulse Sequences*, Burlington, Academic Press, 2004, pp. 363 - 366.

[42] M. A. Bernstein, K. F. King, X. J. Zhou, M. A. Bernstein and X. J. Zhou, "SIGNAL ACQUISITION AND K-SPACE SAMPLING," in *Handbook of MRI Pulse Sequences*, Burlington, Academic Press, 2004, pp. 367 - 442.

[43] C. F. G. C. Geraldes and S. Laurent, "Classification and basic properties of contrast agents for magnetic resonance imaging," *Contrast Media and Molecular Imaging,* pp. 1-23, 2009.

[44] Y.-D. Xiao, R. Paudel, J. Liu, Z.-S. Zhang and S.-K. Zhou, "MRI contrast agents: Classification and application," *International Journal of Molecular Medicine,* pp. 1319-1326, 21 September 2016.

[45] N. Bloembergen and L. O. Morgan, "Proton Relaxation Times in Paramagnetic Solutions. Effects of Electron Spin Relaxation," *The Journal of Chemical Physics,* pp. 842-850, March 1961.

[46] I. Solomon and N. Bloembergen, "Nuclear Magnetic Interactions in the HF Molecule," *The Journal of Chemical Physics,* pp. 261-266, August 1956.

[47] I. Solomon, "Relaxation Processes in a System of Two Spins," *Physical Review,* vol. 99, no. 2, pp. 559-565, 15 July 1955.

[48] N. Bloembergen, "Spin Relaxation Processes in a Two-Proton System," *Physica Review,* pp. 1542-1547, 15 December 1956.

[49] N. Bloembergen, "Proton Relaxation Times in Paramagnetic Solutions," *The Journal of Chemical Physics,* pp. 572-573, August 1957.

[50] É. Tóth, L. Helm and A. E. Merbach, "Relaxivity of MRI Contrast Agents," *Topics in Current Chemistry,* vol. 221, pp. 61-101, 21 January 2002.

[51] A. D. McLachlan, "Line widths of electron resonance spectra in solution," *Proc. R. Soc. Lond. A,* vol. 280, no. 1381, pp. 271-288, 21 July 1964.

[52] J. Wahsner, E. M. Gale, A. Rodríguez-Rodríguez and P. Caravan, "Chemistry of MRI Contrast Agents: Current Challenges and New Frontiers," *Chemical Reviews,* pp. 957-1057, 23 January 2019.

[53] J. W. Chen, R. L. Belford and R. B. Clarkson, "Second-Sphere and Outer-Sphere Proton Relaxation of Paramagnetic Complexes: From," *The Journal of Physical Chemistry A,* pp. 2117-2130, 01 March 1998.

[54] A. Smeraldo, P. A. Netti and E. Torino, "New Strategies in the Design of Paramagnetic CAs," *Contrast media & molecular imaging,* 27 September 2020.

[55] B. Corbin and A. Pollard, "Summary of Imaging in 2020: Visualizing the Future of Healthcare with MR Imaging," *Molecular imaging and biology,* pp. 193-199, April 2019.

[56] Y. Shen, F. L. Goerner, C. Snyder, J. N. Morelli, D. Hao, D. Hu, X. Li and V. M. Runge, "T1 Relaxivities of Gadolinium-Based Magnetic Resonance Contrast Agents in Human Whole Blood at 1.5, 3, and 7 T," *Investigative Radiology,* pp. 330-338, May 2015.

[57] I. M. Noebauer-Huhmann, P. Szomolanyi, V. Juras, O. Kraff, M. E. Ladd and S. Trattnig, "Gadolinium-Based Magnetic Resonance Contrast Agents at 7 Tesla," *Investigative Radiology,* pp. 554-558, September 2010.

[58] J. Pintaske, P. Martirosian, H. Graf, G. Erb, K.-P. Lodemann, C. D. Claussen and F. Schick, "Relaxivity of Gadopentetate Dimeglumine (Magnevist), Gadobutrol (Gadovist), and Gadobenate Dimeglumine (MultiHance) in Human Blood Plasma at 0.2, 1.5, and 3 Tesla," *Investigative Radiology,* pp. 213-221, March 2006.

[59] P. Gillis and S. H. Koenig, "Transverse relaxation of solvent protons induced by magnetized spheres: application to ferritin, erythrocytes, and magnetite," *Magnetic Resonance in Medicine,* pp. 323-345, 12 March 1987.

[60] P. Gillis, . F. Moiny and R. A. Brooks, "On T(2)-shortening by strongly magnetized spheres: a partial refocusing model," *Magnetic Resonance in Medicine,* pp. 257-263, 23 January 2002.

[61] S. Tong, S. Hou, Z. Zheng, J. Zhou and G. Bao, "Coating Optimization of Superparamagnetic Iron Oxide Nanoparticles for High T2 Relaxivity," *Nano Letters,* p. 4607–4613, 10 November 2010.

[62] S. Caspani, R. Magalhães, J. P. Araújo and C. T. Sousa, "Magnetic Nanomaterials as Contrast Agents for MRI," *Materials,* pp. 1996-1944, 5 June 2020.

[63] S. Caspani, R. Magalhães, J. P. Araújo and C. T. Sousa, "Magnetic Nanomaterials as Contrast Agents for MRI," *Materials,* vol. 13, no. 11, 05 June 2020.

[64] Q. A. Pankhurst, J. Connolly, S. K. Jones and J. Dobson, "Applications of magnetic nanoparticles in biomedicine," *Journal of Physics D: Applied Physics,* pp. 167-181, 19 June 2003.

[65] M. Rohrer, H. Bauer, J. Mintorovitch, M. Requardt and H.-J. Weinmann, "Comparison of magnetic properties of MRI contrast media solutions at different magnetic field strengths," *Investigative radiology,* pp. 715-724, November 2005.

[66] A. Thakor, J. Jokerst, P. Ghanouni, J. L. Campbell, E. Mittra and S. S. Gambhir, "Clinically Approved Nanoparticle Imaging Agents," *Journal of Nuclear Medicine,* pp. 1833-1837, 01 December 2016.

[67] H. B. Na, C. Song and T. Hyeon, "Inorganic Nanoparticles for MRI Contrast Agents," *Advanced Materials,* pp. 2133-2148, 5 June 2009.

[68] P. C. N. van Zijl and N. N. Yadav, "Chemical exchange saturation transfer (CEST): What is in a name and what isn't?," *Magnetic Resonance in Medicine,* pp. 927-948, 01 April 2011.

[69] B. Wu, G. Warnock, M. Zaiss, C. Lin, M. Chen, Z. Zhou, L. Mu, D. Nanz, R. Tuura and G. Delso, "An overview of CEST MRI for non-MR physicists," *EJNMMI Physics,* vol. 3, no. 19, 26 August 2016.

[70] E. Vinogradov, A. D. Sherry and R. E. Lenkinski, "CEST: From basic principles to applications, challenges and opportunities," *Journal of Magnetic Resonance,* pp. 155-172, 01 April 2013.

[71] C. . K. Jones, M. J. Schlosser, P. C. M. van Zijl, M. G. Pomper, X. Golay and J. Zhou, "Amide proton transfer imaging of human brain tumors at 3T," *Magnetic Resonance in Medicine,* pp. 585-592, 04 August 2006.

[72] M. T. McMahon, A. A. Gilad, M. A. DeLiso, S. M. Cromer Berman, J. W. M. Bulte and P. C. M. van Zijl, "New "multicolor" polypeptide diamagnetic chemical exchange saturation transfer (DIACEST) contrast agents for MRI," *Magnetic Resonance in Medicine,* pp. 803-812, 24 September 2008.

[73] K. M. Ward, A. H. Aletras and R. S. Balaban, "A New Class of Contrast Agents for MRI Based on Proton Chemical Exchange Dependent Saturation Transfer (CEST)," *Journal of magnetic resonance,* pp. 79-87, 04 March 2000.

[74] A. D. Sherry and M. Woods, "Chemical Exchange Saturation Transfer Contrast Agents for Magnetic Resonance Imaging," *Annual Review of Biomedical Engineering,* pp. 391-411, 18 April 2008.

[75] D. Parrott, W. S. Fernando and A. F. Martins, "Smart MRI Agents for Detecting Extracellular Events In Vivo: Progress and Challenges," *Inorganics,* vol. 7, no. 2, 09 February 2019.

[76] J. Zhou, H.-Y. Heo, L. Knutsson, P. C. M. van Zijl and S. Jiang, "APT-weighted MRI: Techniques, current neuro applications, and challenging issues," *Journal of magnetic resonance imaging,* pp. 347-364, 20 January 2019.

[77] J. M. Goldenberg and M. D. Pagel, "Assessments of tumor metabolism with CEST MRI," *NMR in biomedicine,* 25 June 2018.

[78] X. Xu, N. N. Yadav, L. Knutsson, J. Hua, R. Kalyani, E. Hall, J. Laterra, J. Blakeley, R. Strowd, M. Pomper, P. Barker, K. Chan, G. Liu, M. T. McMahon, R. D. Stevens and P. C. M. van Zijl, "Dynamic Glucose-Enhanced (DGE) MRI: Translation to Human Scanning and First Results in Glioma Patients," *Tomography,* pp. 105-114, December 2015.

[79] K. Herz, T. Lindig, A. Deshmane, J. Schittenhelm, M. Skardelly, B. Bender, U. Ernemann, K. Scheffler and M. Zaiss, "T1ρ-based dynamic glucose-enhanced (DGEρ) MRI at 3 T: method development and early clinical experience in the human brain," *Magnetic Resonance in Medicine,* pp. 1832-1847, 01 November 2019.

[80] Z. Chen, Z. Han and G. Liu, "Repurposing Clinical Agents for Chemical Exchange Saturation Transfer Magnetic Resonance Imaging: Current Status and Future Perspectives," *Pharmeceuticals,* 24 December 2020.

[81] Y. Li, H. Chen, J. Xu, N. N. Yadav, K. W. Y. Chan, L. Luo, M. T. McMahon, B. Vogelstein, P. C. M. van Zijl, S. Zhou and G. Liu, "CEST theranostics: label-free MR imaging of anticancer drugs," *Oncotarget,* pp. 6369-6378, 09 February 2016.

[82] L. L. Lock, Y. Li, X. Mao, H. Chen, V. Staedtke, R. Bai, W. Ma, R. Lin, Y. Li, G. Liu and H. Cui, "One-Component Supramolecular Filament Hydrogels as Theranostic Label-Free Magnetic Resonance Imaging Agents," *ACS Nano,* pp. 797-805, 24 January 2017.

[83] Y. Yuan, J. Zhang, X. Qi, S. Li, G. Liu, S. Siddhanta, I. Barman, X. Song, M. T. McMahon and J. W. M. Bulte, "Furin-mediated intracellular self-assembly of olsalazine nanoparticles for enhanced magnetic resonance imaging and tumour therapy," *Nature materials,* pp. 1376-1383, 21 October 2019.

[84] G. N. Holland, P. A. Bottomley and W. S. Hinshaw, "19F magnetic resonance imaging," *Journal of Magnetic Resonance,* pp. 133-136, October 1977.

[85] J. Ruiz-Cabello, B. P. Barnett, P. A. Bottomley and J. W. Bulte, "Fluorine (19F) MRS and MRI in biomedicine," *NMR in Biomedicine,* pp. 114-129, 15 September 2010.

[86] X. Staal, O. Koshkina and M. Srinivas, "In vivo 19-fluorine magnetic," *Fluorine in Life Sciences: Pharmaceuticals, Medicinal Diagnostics, and Agrochemicals, Elsevier Inc.,* pp. 397-424, 2019.

[87] Z. Bober, D. Aebisher, Ł. Ożóg, J. Tabarkiewicz, P. Tutka and D. Bartusik-Aebisher, "19F MRI As a tool for imaging drug delivery to tissue and individual cells," pp. 99-109, January 2017.

[88] I. Tirotta, A. Mastropietro, C. C. Cordiglieri, L. Gazzera, F. Baggi, G. Baselli, M. G. Bruzzone, I. Zucca, G. Cavallo, G. Terraneo, F. B. Bombelli, P. Metrangolo and G. Resnatia, "A Superfluorinated Molecular Probe for Highly Sensitive in vivo 19F-MRI," *Journal of the American Chemical Society,* 18 June 2014.

[89] P. Bouvain , S. Temme and U. Flögel, "Hot spot 19F magnetic resonance imaging of inflammation," *WIREs Nanomedicine and Nanobiotechnology,* vol. 12, no. 6, 07 May 2020.

[90] D. Jirak, A. Galisova, K. Kolouchova, D. Babuka and M. Hruby, "Fluorine polymer probes for magnetic resonance imaging: quo vadis?," *Magnetic Resonance Materials in Physics, Biology and Medicine,* p. 173–185, 29 November 2018.

[91] S. Rizzo, F. Padelli, E. Rinaldi, D. Gioeni, S. Brizzola, F. Acocella, L. Spaggiari, F. Baggi, M. Bellomi, M. G. Bruzzone and F. Petrella, "7-T MRI tracking of mesenchymal stromal cells after lung injection in a rat model," *European Radiology Experimental,* vol. 4, no. 54, 08 October 2020.

[92] A. V. Makela and P. J. Foster, "Preclinical 19F MRI cell tracking at 3 Tesla," *Magnetic Resonance Materials in Physics, Biology and Medicine,* pp. 123-132, 01 February 2019.

[93] C. Fink, M. Smitch, J. M. Gaudet, A. Makela, P. J. Foster and G. A. Dekaban, "Fluorine-19 Cellular MRI Detection of In Vivo Dendritic Cell Migration and Subsequent Induction of Tumor Antigen-Specific Immunotherapeutic Response," *Molecular Imaging and Biology,* pp. 549-561, 01 June 2020.

[94] A. V. Makela and P. J. Foster, "Imaging macrophage distribution and density in mammary tumors and lung metastases using fluorine-19 MRI cell tracking," *Magnetic Resonance in Medicine,* vol. 80, no. 3, pp. 1138-1147, 12 January 2018.

[95] J. De Blois, G. Kania, P. Blyszczyk, M. Stuber, U. Eriksson and J. Schwitter, "Selective in vivo visualization of immune-cell infiltration in a mouse model of autoimmune myocarditis by fluorine-19 cardiac magnetic resonance," *Circulation. Cardiovascular imaging,* vol. 6, no. 2, 23 January 2013.

[96] C. Gonzales, H. AI Yoshihara, R. B. van Heeswijk, . P. Mieville, H. Lothar, P. Blyszczuk, G. Kania, U. Eriksson and J. Schwitter, "19F-Magnetic Resonance Imaging for Tracking BoneMarrow Macrophages in a Model of Experimental Autoimmune Myocarditis: A Pilot Study," *Biomedical Journal of Scientific & Technical Research,* vol. 29, no. 3, pp. 22419-22428, 07 August 2020.

[97] F. Bönner, W. M. Merx, K. Klingel, P. Begovatz, U. Flögel, M. Sager, S. Temme, C. Jacoby, R. M. Salehi , C. Grapentin, R. Schubert, J. Bunke, M. Roden, M. Kelm and J. Schrader, "Monocyte imaging after myocardial infarction with 19F MRI at 3 T: a pilot study in explanted porcine hearts," *European heart journal. Cardiovascular Imaging,* pp. 612-620, 01 March 2015.

[98] N. Vindegaard, C. Muñoz-Briones, H. H. El Ali, L. K. Kristensen, R. S. Rasmussen, F. F. Johansen and H. Hasseldam, "T-cells and macrophages peak weeks after experimental stroke: Spatial and temporal characteristics," *Neuropathology,* pp. 407-414, 18 May 2017.

[99] A. Khurana, F. Chapelin, H. Xu, J. R. Acevedo, A. Molinolo and Q. Nguyen, "Visualization of macrophage recruitment in head and neck carcinoma model using fluorine-19 magnetic resonance imaging," *Magnetic resonance in medicine,* pp. 1972-1980, 26 July 2017.

[100] G. Weise, T. C. Basse-Luesebrink, C. Wessig, P. M. Jakob and G. Stoll, "In vivo imaging of inflammation in the peripheral nervous system by (19)F MRI," *Experimental neurology,* pp. 4949-501, 01 April 2011.

[101] S. Weibel , T. C. Basse-Luesebrink, M. Hess, E. Hofmann, C. Seubert, J. Langbein-Laugwitz, I. Gentschev, V. J. F. Sturm, Y. Ye, T. Kampf, P. M. Jakob, and A. A. Szalay, "Imaging of Intratumoral Inflammation during Oncolytic Virotherapy of Tumors by 19F-Magnetic Resonance Imaging (MRI)," *PLoS ONE,* vol. 8, no. 2, 18 February 2013.

[102] A. Balducci, Y. Wen, Y. Zhang, B. M. Helfer, T. K. Hitchens, W. S. Meng, A. K. Wesa and J. M. Janjic, "A novel probe for the non-invasive detection of tumor-associated inflammation," *Oncoimmunology,* vol. 2, no. 2, 01 February 2013.

[103] H. Vu-Quang, M. S. Vinding, T. Nielsen , G. M. Ullisch, N. C. Nielsen and J. Kjems , "Theranostic tumor targeted nanoparticles combining drug delivery with dual near infrared and 19 F magnetic resonance imaging modalities," *Nanomedicine : nanotechnology, biology, and medicine,* pp. 1873-1884, 29 April 2016.

[104] J. D. Seitz, J. G. Vineberg, L. Wei, J. F. Khan, B. Lichtenthal, C.-F. Lin and I. Ojima, "Design, Synthesis and Application of Fluorine-Labeled Taxoids as (19)F NMR Probes for the Metabolic Stability Assessment of Tumor-Targeted Drug Delivery Systems," *Journal of fluorine chemistry,* pp. 148-161, 01 March 2015.

[105] C. Jacoby, S. Temme, F. Mayenf, N. Benoit, M. P. Krafft, R. Schubert, J. Schrader and U. Flögel, "Probing different perfluorocarbons for in vivo inflammation imaging by 19F MRI: image reconstruction, biological half-lives and sensitivity," *NMR in biomedicine,* pp. 261-271, 19 December 2013.

[106] A. H. J. Staal, K. Becker, O. Tagit, N. Koen van Riessen, O. Koshkina, A. Veltien, P. Bouvain, K. R. G. Cortenbach, T. Scheenen, U. Flögel, S. Temme and M. Srinivas, "In vivo clearance of 19F MRI imaging nanocarriers is strongly influenced by nanoparticle ultrastructure," *Biomaterials,* 01 December 2020.

[107] M. Szczęch, A. Karabasz, N. Łopuszyńska, M. Bzowska, W. P. Węglarz, P. Warszyński and K. Szczepanowicz , "Gadolinium labeled polyelectrolyte nanocarriers for theranostic application," *Colloids and Surfaces B: Biointerfaces,* vol. 183, pp. 26508-26520, 1 November 2019.

[108] M. Szczęch and K. Szczepanowicz, "Polymeric Core-Shell Nanoparticles Prepared by Spontaneous Emulsification Solvent Evaporation and Functionalized by the Layer-by-Layer Method," *Nanomaterials,* vol. 10, no. 3, 10 March 2020.

[109] G. B. Sukhorukov, E. Donath, H. Lichtenfeld, E. Knippel, M. Knippel, A. Budde and H. Möhwald, "Layer-by-layer self assembly of polyelectrolytes on colloidal particles," *Colloids and Surfaces A: Physicochemical and Engineering Aspects,* pp. 253-266, 15 June 1998.

[110] J. J. Richardson, M. Björnmalm and F. Caruso, "Technology-driven layer-by-layer assembly of nanofilms," *Science,* vol. 246, no. 6233, pp. 411-422, 24 April 2015.

[111] Y. Nakamura, A. Mochida, P. L. Choyke and H. Kobayashi, "Nanodrug Delivery: Is the Enhanced Permeability and Retention Effect Sufficient for Curing Cancer?," *Bioconjugate Chemistry,* pp. 2225-2238, 19 October 2016.

[112] M. Szczęch, D. Orsi, N. Łopuszyńska, L. Cristofolini, K. Jasiński, W. P. Węglarz, F. Albertini, S. Kereïche and K. Szczepanowicz, "Magnetically responsive polycaprolactone nanocarriers for application in the biomedical field: magnetic hyperthermia, magnetic resonance imaging, and magnetic drug delivery," *RSC Advances,* vol. 10, no. 71, pp. 43607-43618, 08 December 2020.

[113] M. Szczęch, N. Łopuszyńska, W. Tomal, K. Jasiński , W. P. Węglarz, P. Warszyński and K. Szczepanowicz, "Nafion-Based Nanocarriers for Fluorine Magnetic Resonance Imaging," *Langmuir,* p. 9534–9539, 24 July 2020.

[114] M. Szczęch, A. Hinz, N. Łopuszyńska, M. Bzowska, W. Węglarz and K. Szczepanowicz, "Polyaminoacid Based Core@shell Nanocarriers of 5-Fluorouracil: Synthesis, Properties and Theranostics Application," *International Journal of Molecular Sciences,* vol. 22, no. 23, 11 25 2021.

[115] A. Maximenko, J. Depciuch, N. Łopuszyńska, M. Stec, Ż. Światkowska-Warkocka, V. Bayev, P. M. Zieliński, J. Baran, J. Fedotova, W. P. Węglarz and M. Parlinska-Wojtan, "Fe3O4@SiO2@Au nanoparticles for MRI-guided chemo/NIR photothermal therapy of cancer cells," *RSC Advances,* p. 26508–26520, 15 July 2020.

[116] P. Garteiser, O. Bane, S. Doblas, I. Friedli, S. Hectors, G. Pagé and B. E. Van Beers, "Experimental Protocols for MRI Mapping of Renal T1," in *Preclinical MRI of the Kidney. Methods in Molecular Biology vol 2216*, Humana, New York, NY, 2021.

[117] GmbH Bruker BioSpin MR, "ParaVision 5.1 Users Manual," pp. A-6.15 139 -140, 2010.

[118] GmbH Bruker BioSpin MRI, "ParaVision 5.1 Users Manual," pp. A-6.17 148 - 149, 2010.

[119] GmbH Bruker BioSpin MRI, "ParaVision 5.1 Users Manual," pp. A-6.13 122 - 128, 2010.

[120] J. Frahm, A. Haase and D. Matthaei, "Rapid NMR imaging of dynamic processes using the FLASII technique," *Magnetic Resonance in Medicine,* vol. 3, no. 2, pp. 321 - 327, 01 April 1986.

[121] N. Łopuszyńska, K. Szczepanowicz, K. Jasiński, P. Warszyński and W. P. Węglarz, "Effective Detection of Nafion®-Based Theranostic Nanocapsules Through 19F Ultra-Short Echo Time MRI," *Nanomaterials,* vol. 10, no. 11, 26 10 2020.

[122] K. A. Mauritz and R. B. Moore, "State of Understanding of Nafion," *Chemical Reviews,* pp. 4535 - 4586, 01 10 2004.

[123] F. Springer, G. Steidle, P. Martirosian, C. D. Claussen and F. Schick, "Effects of in-pulse transverse relaxation in 3D ultrashort echo time sequences: Analytical derivation, comparison to numerical simulation and experimental application at 3 T," *Journal of Magnetic Resonance,* pp. 88-96, 23 June 2010.

[124] W. Zhang, L. Liu, H. Chen, K. Hu, I. Delahunty, S. Gao and J. Xie, "Surface impact on nanoparticle-based magnetic resonance imaging contrast agents," *Theranostics,* vol. 8, no. 9, pp. 2521-2548, 2018.

[125] Z. Zhou, R. Tian, Z. Wang, Z. Yang, Y. Liu, G. Liu, R. Wang, J. Gao, J. Song, L. Nie and X. Chen, "Artificial local magnetic field inhomogeneity enhances T2 relaxivity," *Nature Communications,* vol. 8, no. 1, 18 May 2017.

[126] L. Wu, M. Wu, X. Lin, X. Zhang, X. Liu and J. Liu, "Magnetite nanocluster and paclitaxel-loaded charge-switchable nanohybrids for MR imaging and chemotherapy," *Journal of Materials Chemistry B,* vol. 5, no. 4, pp. 849-857, 15 December 2017.

[127] R. J. Hickey, A. S. Haynes, J. M. Kikkawa and S.-J. Park, "Controlling the Self-Assembly Structure of Magnetic Nanoparticles and Amphiphilic Block-Copolymers: From Micelles to Vesicles," *Journal of the American Chemical Society,* pp. 1517-1525, 09 Ferbruary 2011.

[128] Z. Yu, C. Peng, Y. Luo, J. Zhu, C. Chen, M. Shen and X. Shi, "Poly(γ-glutamic acid)-stabilized iron oxide nanoparticles: synthesis, characterization and applications for MR imaging of tumors," *RSC Advances,* pp. 76700-76707, 04 September 2015.

[129] Z. Zhang, F.-L. Zhou, G.-L. Davies and G. R. Williams, "Theranostics for MRI-guided therapy: Recent developments," *View,* 03 August 2021.

[130] A. Nazemi, F. Martínez, T. J. Scholl and E. R. Gillies, "Biodegradable dendritic polymersomes as modular, high-relaxivity MRI contrast agents," *RSC Advances,* pp. 7971-7973, 06 August 2012.

[131] W.-C. Huang, Y.-H. Hsu, W.-Y. Hsieh and H.-C. Chiu, "Development of a diagnostic polymersome system for potential imaging delivery," *Colloids and Surfaces B: Biointerfaces,* pp. 67-76, 01 April 2015.

[132] H. Cai, X. Dai, X. Wang, P. Tan, L. Gu, Q. Luo, X. Zheng, Z. Li, H. Zhu, H. Zhang, Z. Gu, Q. Gong and K. Luo, "A Nanostrategy for Efficient Imaging-Guided Antitumor Therapy through a Stimuli-Responsive Branched Polymeric Prodrug," *Advanced Science,* 01 March 2020.

[133] M. H, G. K and F. J, "The EPR Effect and Polymeric Drugs: A Paradigm Shift for Cancer Chemotherapy in the 21st Century," *Adv Polym Sci,* pp. 103-121, 30 November 2005.

[134] W. Zhang, L. Liu, H. Chen, K. Hu, I. Delahunty, S. Gao and J. Xie, "Surface impact on nanoparticle-based magnetic resonance imaging contrast agents," *Theranostics,* pp. 2521-2548, 04 May 2018.

[135] A. Kostopoulou and A. Lappas, "Colloidal magnetic nanocrystal clusters: variable length-scale interaction mechanisms, synergetic functionalities and technological advantages," *Nanotechnology Reviews,* vol. 6, no. 4, pp. 595-624, 10 September 2015.

[136] S.-H. Noh, W. Na, J.-T. Jang, J.-H. Lee, E. J. Lee, S. H. Moon, Y. Lim, J.-S. Shin and . J. Cheon, "Nanoscale magnetism control via surface and exchange anisotropy for optimized ferrimagnetic hysteresis," *Nano letters,* 23 June 2012.

[137] Z. Zhao, Z. Zhou, J. Bao, Z. Wang, J. Hu, X. Chi, . K. Ni, R. Wang, X. Chen, Z. Chen and J. Gao, "Octapod iron oxide nanoparticles as high-performance T2 contrast agents for magnetic resonance imaging," *Nature Communications,* vol. 4, no. 1, 01 August 2013.

[138] S. Larumbe, C. Gómez-Polo, J. I. Pérez-Landazábal and J. M. Pastor, "Effect of a SiO2 coating on the magnetic properties of Fe3O4 nanoparticles," *Journal of physics. Condensed matter,* 16 June 2012.

[139] M. Abbas, S. R. Torati and C. Kim, "A novel approach for the synthesis of ultrathin silica-coated iron oxide nanocubes decorated with silver nanodots (Fe3O4/SiO2/Ag) and their superior catalytic reduction of 4-nitroaniline," *Nanoscale,* 15 June 2015.

[140] M. N. Islam, M. Abbas, B. Sinha and J.-R. Joeng, "Silica encapsulation of sonochemically synthesized iron oxide nanoparticles," *Electronic Materials Letters,* pp. 817-820, 01 November 2013.

[141] N. Kostevšek, "A Review on the Optimal Design of Magnetic Nanoparticle-Based T2 MRI Contrast Agents," *Magnetochemistry,* vol. 6, no. 1, 28 February 2020.

[142] E. Peng, F. Wang and J. M. Xue, "Nanostructured magnetic nanocomposites as MRI contrast agents," *Journal of Materials Chemistry B,* pp. 2241-2276, 03 February 2015.

[143] E. Pöselt, H. Kloust, U. Tromsdorf, M. Janschel, C. Hahn, C. Maßlo and H. Weller, "Relaxivity Optimization of a PEGylated Iron-Oxide-Based Negative Magnetic Resonance Contrast Agent for T2-Weighted Spin–Echo Imaging," *ACS Nano,* pp. 1619-1624, 28 February 2012.

[144] D. Jirak, A. Galisova, K. Kolouchova, D. Babuka and M. Hruby, "Fluorine polymer probes for magnetic resonance imaging: quo vadis?," *Magnetic Resonance Materials in Physics, Biology and Medicine,* 29 November 2018.

[145] K. Szczepanowicz, M. Bzowska, T. Kruk, A. Karabasz, J. Bereta and P. Warszyński, "Pegylated polyelectrolyte nanoparticles containing paclitaxel as a promising candidate for drug carriers for passive targeting," *Colloids and Surfaces B: Biointerfaces,* pp. 463-471, 1 July 2016.

[146] J. T. Nofiele and H.-L. M. Cheng, "Ultrashort Echo Time for Improved Positive-Contrast Manganese-Enhanced MRI of Cancer," *PLOS ONE,* vol. 8, no. 3, 04 March 2013.

[147] F. Springer, G. Steidle, P. Martirosian, C. D. Claussen and F. Schick, "Effects of in-pulse transverse relaxation in 3D ultrashort echo time sequences: analytical derivation, comparison to numerical simulation and experimental application at 3T," *Journal of magnetic resonance,* vol. 206, no. 1, pp. 88-96, September 2010.

[148] . J. . T. Bushberg, J. A. Seibert, E. M. Leidholdt and J. M. Boone, The essential physics of medical imaging (3rd ed.), Philadelphia, PA: Lippincott Williams and Wilkins, 2011.

[149] D. W. McRobbie, E. A. Moore, M. J. Graves and M. R. Prince, MRI from Picture to Proton, Cambridge University Press, 2017.

[150] A. Galante, R. Sinibaldi, A. Conti, C. De Luca, N. Catallo, S. Piero , V. Pizzella,, G. L. Romani, A. Sotgiu and S. Della Penna, "Fast Room Temperature Very Low Field-Magnetic Resonance Imaging System Compatible with MagnetoEncephaloGraphy Environment," *PLOS ONE,* 2 December 2015.

[151] J. Graessner, "Bandwidth in MRI?," *MAGNETOM Flash,* no. 2, pp. 122-127, 2013.

[152] J. R. Kruga, R. Schadewijk, F. J. Vergeldt, A. G. Webb, H. J. M. de Grootd, A. Alia, H. Van As and A. H. Velders, "Assessing spatial resolution, acquisition time and signal-to-noise ratio for commercial

microimaging systems at 14.1, 17.6 and 22.3 T," *Journal of Magnetic Resonance,* vol. Journal of Magnetic Resonance, p. 106770, 2020.

[153] W. M. Spees, N. Buhl, P. Sun, J. J. Ackerman, N. J. Jeffrey and J. R. Garbow, "Quantification and Compensation of Eddy-Current-Induced Magnetic Field Gradients," *Journal of magnetic resonance,* p. 116–123, September 2011.

[154] C. B. Ahn and Z. H. Cho, "Analysis of the Eddy-Current Induced Artifacts and the temporal compensation in nuclear magnetic resonance imaging," *IEEE TRANSACTIONS ON MEDICAL IMAGING,* pp. 47-52, March 1991.

[155] T. Smith, K. Affram, E. L. Nottingham, B. Han, F. Amissah, S. Krishnan, J. Trevino and E. Agyare, "Application of smart solid lipid nanoparticles to enhance the efficacy of 5-fluorouracil in the treatment of colorectal cancer," *Scientific Reports,* 12 October 2020.

[156] P. F. Hsiao, R. Anbazhagan, C. Hsiao-Ying, A. Vadivelmurugan and H.-C. Tsai, "Thermoresponsive polyamic acid-conjugated gold nanocarrier for enhanced light-triggered 5-fluorouracil release," *RSC Advances,* vol. 7, pp. 8357 - 8365, 25 January 2017.

[157] Y. A. Haggag, M. A. Osman, S. A. El-Gizawy, A. E. Goda, M. M. Shamloula, A. M. Faheem and P. A. McCarron, "Polymeric nano-encapsulation of 5-fluorouracil enhances anti-cancer activity and ameliorates side effects in solid Ehrlich Carcinoma-bearing mice," *Biomedicine & Pharmacotherapy,* vol. 105, pp. 215-224, September 2018.

[158] A. Mohan , S. Narayanan, S. Sethuraman and U. M. Krishnan, "Novel Resveratrol and 5-Fluorouracil Coencapsulated in PEGylated Nanoliposomes Improve Chemotherapeutic Efficacy of Combination against Head and Neck Squamous Cell Carcinoma," *BioMed Research International,* 09 July 2014.

[159] L. Du, Y. Jin, J. Yang, S. Wang and X. Wang, "A functionalized poly(amidoamine) nanocarrier-loading 5-fluorouracil: pH-responsive drug release and enhanced anticancer effect," *Anticancer Drugs,* vol. 24, no. 12, pp. 172- 180, February 2013.

[160] D. Moorkoth, K. M. Nampoothiri, S. Nagarajan, A. Ravindran Girija, S. Balasubramaniyan and D. S. Kumar, "Star-Shaped Polylactide Dipyridamole Conjugated to 5-Fluorouracil and 4-Piperidinopiperidine Nanocarriers for Bioimaging and Dual Drug Delivery in Cancer Cells," *ACS Applied Polymer Materials,* vol. 3, no. 2, pp. 737 - 756, 12 February 2021.

[161] J. Xu, G. Zhang, X. Luo, D. Wang, W. Zhou, Y. Zhang, W. Zhang, J. Chen, Q. Meng, E. Chen, H. Chen and Z. Song, "Co-delivery of 5-fluorouracil and miRNA-34a mimics by host-guest self-assembly nanocarriers for efficacious targeted therapy in colorectal cancer patient-derived tumor xenografts," *Theranostics,* vol. 11, no. 5, pp. 2475 - 2489, 2021.

[162] M. Szota, K. Reczyńska-Kolman, E. Pamuła, O. Michel, J. Kulbacka and B. Jachimska, "Poly(amidoamine) Dendrimers as Nanocarriers for 5-Fluorouracil: Effectiveness of Complex Formation and Cytotoxicity Studies," *International Journal of Molecular Sciences,* vol. 22, no. 20, 2021.

[163] X. Ren, W. Wang, L. Ke, E. Ning, L. Du and J. Bradshaw, "A 5-fluorouracil-loaded pH-responsive dendrimer nanocarrier for tumor targeting," *International journal of pharmaceutics,* vol. 420, no. 2, pp. 378 - 384, 28 November 2011.

[164] G. Neri, G. Mion, A. Pizzi, W. Celentano, L. Chaabane, M. R. Chierotti, R. Gobetto, M. Li, P. Messa, F. De Campo, F. Cellesi, P. Metrangolo and F. Baldelli Bombelli, "Fluorinated PLGA Nanoparticles for

Enhanced Drug Encapsulation and 19F NMR Detection," vol. 26, no. 44, pp. 10057 - 10063, 06 August 2020.

[165] Y. Kato and D. Artemov, "Monitoring of release of cargo from nanocarriers by MRI/MR spectroscopy (MRS): significance of T2/T2* effect of iron particles," *Magnetic resonance in medicine,* vol. 61, no. 5, pp. 1059 - 1065, May 2009.

[166] Y. Shepelytskyi, M. S. Fox, K. Davenport, T. Li, M. S. Albert and E. Davenport, "In-Vivo Retention of 5-Fluorouracil Using (19)F Magnetic Resonance Chemical Shift Imaging in Colorectal Cancer in a Murine Model," *Scientific reports,* vol. 9, no. 1, 13 Sepetember 2019.

[167] Y. Otake, K. Hirata, Y. Soutome and Y. Bito, "In-vivo 19 F Imaging of 5-Fluorouracil and its Metabolites in Rat by Two-Element Phased-Array Coil," *proc. International Society for Magnetic Resonance in Medicine 19 (2011),* 2010.

[168] Y. Doi, T. Shimmura, H. Kuribayashi, Y. Tanaka and Y. Kanazawa, "Quantitative (19)F imaging of nmol-level F-nucleotides/-sides from 5-FU with T(2) mapping in mice at 9.4T," *Magnetic resonance in medicine,* vol. 62, no. 5, pp. 1129 - 1139, November 2009.

[169] Z. Dai and . H. Möhwald, "Highly Stable and Biocompatible Nafion-Based Capsules with Controlled Permeability for Low-Molecular-Weight Species," *Chemistry - A European Journal,* vol. 8, no. 20, p. 4751–4755, 14 October 2002.

[170] K. Yoshida, K. Sato, T. Ono, T. Dairaku and Y. Kashiwagi, "Preparation of Nafion/Polycation Layer-by-Layer Films for Adsorption and Release of Insulin," *Polymers,* vol. 10, no. 8, 2018.

[171] V. A. Pham Ba, D.-g. Cho and S. Hong, "Nafion-Radical Hybrid Films on Carbon Nanotube Transistors for Monitoring Antipsychotic Drug Effects on Stimulated Dopamine Release," *ACS Applied Materials & Interfaces,* vol. 11, no. 10, pp. 9716 - 9723, 03 March 2019.

[172] M. A. Özbek, A. Yaşar, S. Çete, E. Er and N. Erk, "A novel biosensor based on graphene/platinum nanoparticles/Nafion composites for determination of glucose," *Journal of Solid State Electrochemistry,* p. 1601–1610, 17 March 2021.

[173] T. Tasnuva , J. B. Bulitta, . C. B. Landersdorfer, . V. Cashin and . A. Yu, "Stability and controlled antibiotic release from thin films embedded with antibiotic loaded mesoporous silica nanoparticles," *RSC Advances,* vol. 5, no. 130, pp. 107839 - 107846, 02 December 2015.

[174] Q. Yi and G. . B. Sukhorukov, "Externally Triggered Dual Function of Complex Microcapsules," *ACS Nano,* vol. 7, no. 10, pp. 8693 - 8705, 22 October 2013.

Appendix A

Mössbauer spectroscopy results for Fe_3O_4@SiO_2 NPs

Above the Verwey transition temperature, which is 125 K, magnetite has a cubic Fd-3m symmetry with an inverse spinel cubic structure. O^{2-} ions form an FCC lattice and iron cations occupy interstitial sites. Half of the Fe^{3+} cations occupy tetrahedral sites (A-site), while the other half, and Fe^{2+} cations, occupy octahedral sites (B-site). This means that at tetrahedral sites, Fe atoms are in a +3 state, while in B positions the mean valence is +2.5 [1-3]. Room temperature (290 K) ^{57}Fe Mössbauer spectra are shown in Figure 66, while hyperfine parameters are summarized in Table 18. Low temperature (16K) results are presented in Figure 67 and Table 19.

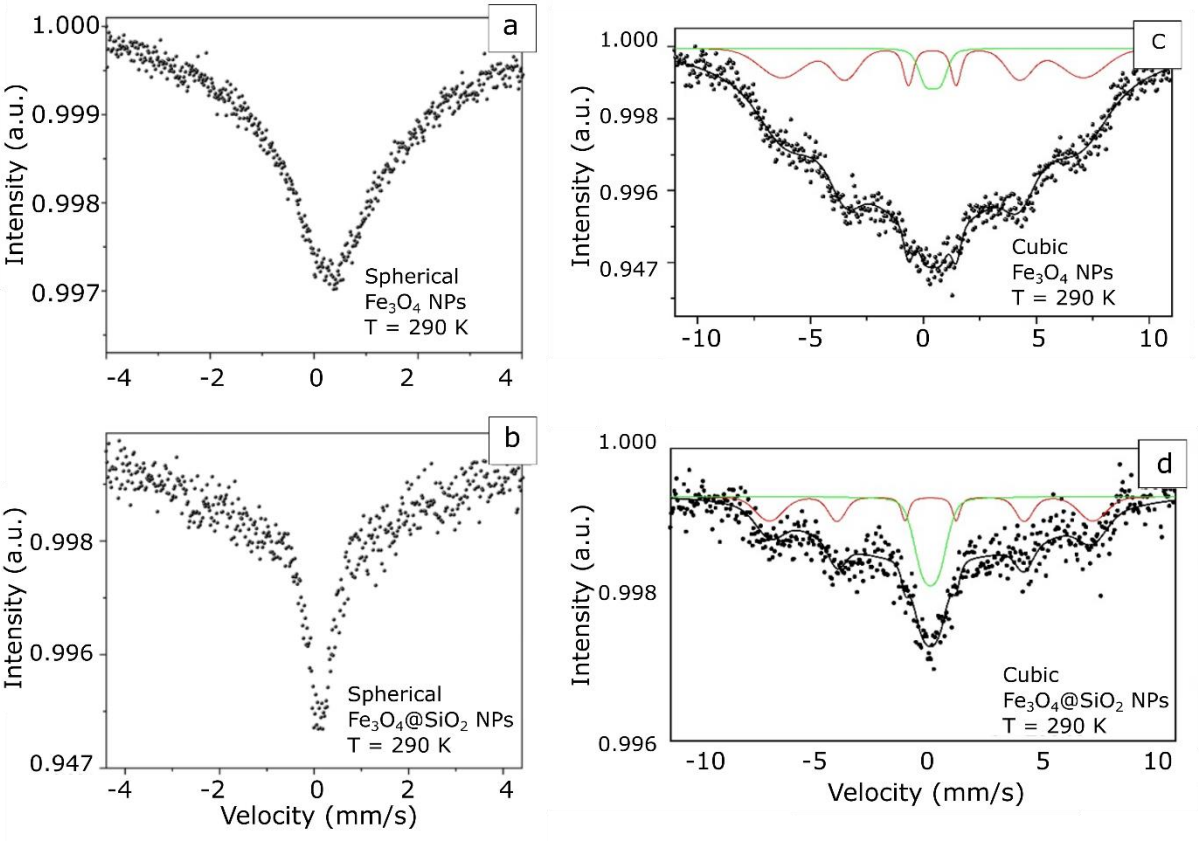

Figure 66 Room temperture (290K) Fe_3O_4 Mössbauer spectra for (a,b) spherical NPs and (c, d) cubic NPs; Top row – Fe_3O_4 nanoparticles; bottom row – nanoparticles with SiO_2 shell

Table 18 Room temperature (290 K) Mössbauer spectroscopy results for Fe_3O_4 and Fe_3O_4@SiO_2 NPs

Sample	Sub-spectrum	*IS*, [mm/s]	H_{hf}, [T]	H_{hf} - Sigma, [T]	*E*, [mm/s]	Area ratio, %
sphere-Fe_3O_4 NPs	$Fe^{3+}/Fe^{2.5+}$	0.32	-	-	-	26
sphere-Fe_3O_4@SiO_2 (10 nm) NPs	$Fe^{3+}/Fe^{2.5+}$	0.32	-	-	-	26
cubic-Fe_3O_4 NPs	$Fe^{3+}/Fe^{2.5+}$	0.42	-	-	-	3
		0.41	41.5	5.7	0.01	12
cubic-Fe_3O_4@ SiO_2 (10 nm) NPs	$Fe^{3+}/Fe^{2.5+}$	0.32	-	-	-	13
		0.35	43.8	3.4	0.01	15

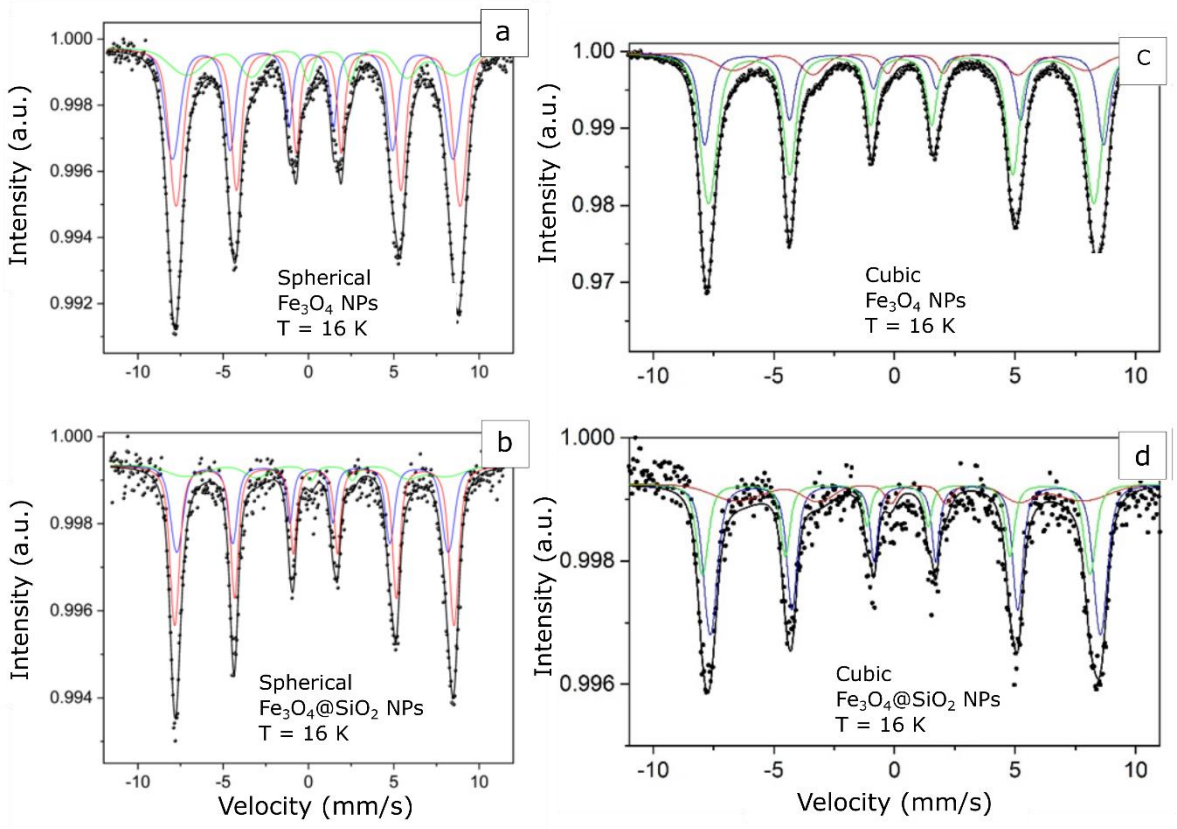

Figure 67 Low temperature (16K) Fe_3O_4 Mössbauer spectra for (a,b) spherical NPs and (c, d) cubic NPs; Top row – Fe_3O_4 nanoparticles; bottom row – nanoparticles with SiO_2 shell

Table 19 Low temperature (16 K) Mössbauer spectroscopy results for Fe_3O_4 and $Fe_3O_4@SiO_2$ NPs

Sample	Sub-spectrum	*IS*, [mm/s]	H_{hf}, [T]	H_{hf} -Sigma, [T]	*E*, [mm/s]	Area ratio, %
sphere-Fe_3O_4 NPs	Fe3+ at A site	0.21	51.1	0.14	0.04	36
	Fe3+ at B site	0.58	51.7	0.12	-0.02	47
	Fe2+ at B site	0.96	48.8	5.5	-0.24	17
sphere-$Fe_3O_4@SiO_2$ (10 nm) NPs	Fe3+ at A site	0.20	49.4	0.11	0.04	35
	Fe3+ at B site	0.38	50.8	0.07	-0.04	53
	Fe2+ at B site	0.90	47.2	6.1	-0.47	12
cubic-Fe_3O_4NPs	Fe3+ at A site	0.28	49.6	1.3	0.00	28
	Fe3+ at B site	0.42	51.4	0.7	-0.02	58
	Fe2+ at B site	0.75	45.5	3.8	-0.11	14
cubic-$Fe_3O_4@SiO_2$ (10 nm) NPs	Fe3+ at A site	0.15	50.0	0.9	-0.03	39
	Fe3+ at B site	0.48	50.2	0.9	0.01	43
	Fe2+ at B site	0.81	45.0	5.7	-0.20	18

The Mössbauer spectra of spherical Fe_3O_4 core samples and $Fe_3O_4@SiO_2$ core-shell NPs are characterized with singlet IS = 0.32 mm/s without resolved quadrupole splitting corresponding to Fe^{3+} ions. For cubic core Fe_3O_4 NPs, the Mössbauer spectra are approximated with a singlet IS = 0.42 mm/s without resolved quadrupole splitting and a sextet IS = 0.41 mm/s corresponding to Fe^{3+} ions. Similarly, for core-shell cubic $Fe_3O_4@SiO_2$ NPs, singlet IS = 0.32 mm/s without resolved quadrupole splitting and sextet IS = 0.35 mm/s corresponding to Fe^{3+} ions were observed. For both shapes of NPs, the observed broadened baseline in the spectra of NPs is most probably caused by the presence of an unresolved magnetic sextet corresponding to $Fe^{2.5+}$ ions, which indicates a superparamagnetic state.

Low temperature (16 K) spectra of Fe_3O_4 and $Fe_3O_4@SiO_2$ for both cubic and spherical geometries are deconvoluted into three sextets corresponding to Fe^{3+} ions at *A* site, Fe^{3+} ions at *B* site, and Fe^{2+} ions at *B* site. For spherical nanoparticles, the ratio of the contribution of a sextet of Fe^{3+} ions at *A* site to the contribution of sextets of Fe ions at *B* site is 0.56 for Fe_3O_4 and 0.54 for $Fe_3O_4@SiO_2$ NPs, which is very close to the value of stoichiometric magnetite (0.50). However, the relative contribution of subspectrum attributed to Fe^{2+} ions at *B* site is less than expected (only 17 % for Fe_3O_4 and 12 % $Fe_3O_4SiO_2$ against ~ 30 % expected). For cubic nanoparticles, the ratio of the contribution of a sextet of Fe^{3+} ions at *A* site to the

contribution of sextets of Fe ions at *B* site is 0.39 and 0.64 for Fe_3O_4 and $Fe_3O_4@SiO_2$ NPs respectively. Also, the contribution of subspectrum of Fe^{2+} ions at the *B* site is again less than theoretical, 14 % for Fe_3O_4 and 18 % for $Fe_3O_4SiO_2$ NPs. A similar ratio of contribution of ions in A and B sites for spherical geometry Fe_3O_4 NPs and encapsulated in SiO_2 shell NPs suggests that they possess a very similar crystal structure, while results obtained for cubic nanoparticles may indicate the influence of the encapsulation on the crystal structure of NPs. Moreover, the lower contribution of Fe^{2+} ions in the Mössbauer spectrum for both geometries of NPs can be attributed to the partial oxidation of Fe_3O_4 NPs, leading to the formation of some amount of maghemite or wüstite at the surface of NPs [3].

[1] Chokkareddy, Rajasekhar Reddy & Kumar, Natesh & Kabane, Bakusele & Redhi, Gan. (2017). Bio-Sensing Performance of Magnetite Nanocomposite for Biomedical Applications. 10.1002/9781119370383.ch7

[2] Tiquia-Arashiro S., Rodrigues D. (2016) Nanoparticles Synthesized by Microorganisms. In: Extremophiles: Applications in Nanotechnology. Springer, Cham.https://doi.org/10.1007/978-3-319-45215-9_1

[3] A. Maximenko , J. Depciuch , N. Łopuszyńska , M. Stec , Ż. Światkowska-Warkocka , V. Bayev P. M. Zieliński, J. Baran , J. Fedotova and W. P. Węglarz , RSC Adv., 2020, 10 , 26508 —26520